N O T I C E

THIS DOCUMENT HAS BEEN REPRODUCED FROM MICROFICHE. ALTHOUGH IT IS RECOGNIZED THAT CERTAIN PORTIONS ARE ILLEGIBLE, IT IS BEING RELEASED IN THE INTEREST OF MAKING AVAILABLE AS MUCH INFORMATION AS POSSIBLE

Final Report, Contract NAS 5-27463
NASA Goddard Space Flight Center
Greenbelt, MD 20771

NASA-CR-176379

E86-10007

LANDSAT-D INVESTIGATIONS IN SNOW HYDROLOGY

OCT 1985
RECEIVED
NASA STI FACILITY
ACCESS DEPT.

Principal Investigator
Jeff Dozier

Contributing Authors

Robert E. Davis **Danny Marks**
Ralph O. Dubayah **Ralph F. Milliff**
James E. Frew **Denise D. Rousseau**
Shusun Li **Zheng-ming Wan**

Original photography may be purchased
EROS Data Center
Sioux Falls, SD 57198

Computer Systems Laboratory
University of California
Santa Barbara, CA 93106

1985

(E86-10007 NASA-CR-176379) LANDSAT-D INVESTIGATIONS IN SNOW HYDROLOGY Final Report (California Univ.) 111 p HC A06/MF A01 CSCL 08H
N86-14709
Unclas
G3/43 00007

OCT
RECEIVED
NASA STI FACILITY

Table of Contents

Introduction 1

1. Snow Reflectance from Landsat-4 Thematic Mapper 2

2. Registering Thematic Mapper Imagery to Digital Elevation Models 3

3. Reflectance Measurements from Landsat Thematic Mapper over Rugged Terrain 4

4. Automated Basin Delineation from Digital Elevation Data 5

5. Field and Laboratory Measurements of Snow Liquid Water by Dilution 6

6. Orthographic Terrain Views Using Data Derived from Digital Elevation Models 7

7. Two-Stream Method for Radiative Transfer in Inhomogeneous Atmospheres over Irregular Surfaces 8

8. A Component Decomposition Model for Evaluating Atmospheric Effects in Remote Sensing 9

8.1. Introduction 9

8.2. Decomposition of Remotely Sensed Radiance 11

8.3. Azimuthally Dependent Plane-Parallel Atmospheric Radiative Transfer 14

9. Model Performance 21

9.1. Atmospheric Point Spread Function 22

9.2. Example – Atmospheric Effects in Landsat Thematic Mapper Images 29

9.3. Notation 31

9.4. Tables 34

9.5. Figures 39

10. Texture Analysis of the Spatial Contiguity of Snow Cover 46

10.1. Introduction 46

10.2. Texture Analysis 48

10.3. Data Processing 53

10.4. Snow Classification 56

10.5. Methods 59

10.6. Results 62

10.7. Discussion and Conclusion 72

10.8. Appendix 77

10.9. Symbols 80

10.10. Tables 82

10.11. Figures 88

11. References 101

Introduction

The work undertaken during and this contract and its results are described in the remainder of the report. Fortunately many of the results from this investigation are available in the journal or conference proceedings literature — published, accepted for publication, or submitted for publication. For these we simply give the reference and the abstract. The papers themselves have been separately delivered to NASA/GSFC. Those results that have not yet been submitted separately for publication are described in considerable detail.

The accomplishments during this contract are summarized in the following list. They correspond to the objectives of the revised proposal.

[1] Analysis of the snow reflectance characteristics of the Landsat Thematic Mapper, including spectral suitability, dynamic range, and spectral resolution.

[2] Development of a variety of atmospheric models for use with Landsat Thematic Mapper data. These include a simple but fast two-stream approximation for inhomogeneous atmospheres over irregular surfaces, and a doubling model for calculation of the angular distribution of spectral radiance at any level in an plane-parallel atmosphere.

[3] Incorporation of digital elevation data into the atmospheric models and into the analysis of the satellite data.

[4] Textural analysis of the spatial distribution of snow cover.

1. Snow Reflectance from Landsat-4 Thematic Mapper

This paper has been published. The reference citation is:

Dozier, J., "Snow reflectance from Landsat-4 Thematic Mapper," *IEEE Transactions on Geoscience and Remote Sensing*, vol. GE-22, pp. 323-328, 1984.

Abstract. In California 75 percent of the agricultural water supply comes from the melting Sierra Nevada snowpack. Basin-wide spectral albedo measurements from the Landsat-4 Thematic Mapper (TM) could be used to better forecase the timing of the spring runoff, because these data can be combined with solar radiation calculations to estimate the net radiation balance. The TM is better-suited for this purpose than the Multispectral Scanner because of its larger dynamic range. Saturation still occurs in bands 1–4, but is severe only in TM1 (0.45–0.52μm). Snow reflectance in TM2 (0.43–0.61μm) is typical of the visible wavelength region, where reflectance is almost insensitive to crystal size but sensitive to contamination. TM4 (0.78–0.90μm) allows estimation of effective optical grain size and thereby spectral extension throughout the near-infrared. TM5 (1.57–1.78μm) can discriminate clouds from snow.

2. Registering Thematic Mapper Imagery to Digital Elevation Models

This paper has been published. The reference citation is:

Frew, J., "Registering thematic mapper imagery to digital elevation models," in *Proceedings, Tenth International Symposium on Machine Processing of Remotely Sensed Data, with Special Emphasis on Thematic Mapper Data and Geographic Information Systems*, ed. M. M. Klepfer and D. B. Morrison, pp. 432-435, Purdue University, West Lafayette, IN, 1984.

Abstract. Several problems arise when attempting to register Landsat Thematic Mapper (TM) data to U.S. Geological Survey digital elevation models (DEMs). Chief among these are:

- TM data are currently available only in a rotated variant of the Space Oblique Mercator (SOM) map projection. Geometric transforms are thus required to access TM data in the geodetic coordinates used by the DEMs. Due to positional errors in the TM data, these transforms require some sort of external control.
- The spatial resolution of TM data exceeds that of the most commonly available DEM data. Oversampling DEM data to TM resolution introduces systematic noise. Common terrain processing algorithms (*e.g.* slope computation) compound this problem by acting as high-pass filters.

3. Reflectance Measurements from Landsat Thematic Mapper over Rugged Terrain

This paper has been published. The reference citation is:

Dozier, J., "Reflectance measurements from Landsat Thematic Mapper over rugged terrain," in *Proceedings, Tenth International Symposium on Machine Processing of Remotely Sensed Data, with Special Emphasis on Thematic Mapper Data and Geographic Information Systems*, ed. M. M. Klepfer and D. B. Morrison, pp. 230-234, Purdue University, West Lafayette, IN, 1984.

Abstract. Spectral albedo measurements from the Landsat-4/5 Thematic Mappers require that spacecraft upwelling radiances be corrected for atmospheric absorption and scattering and for local surface illumination. A two-stream model is developed, with a lower boundary condition that varies with incidence angle. TM data must be registered to digital terrain data. Reflectance from points in shadows can be used to estimate optical depth. Our primary application is determination of the spectral albedo of snow. The TM is better-suited for this purpose than the MSS because of its larger dynamic range.

4. Automated Basin Delineation from Digital Elevation Data

This paper has been published. The reference citation is:

Marks, D., J. Dozier, and J. Frew, "Automated basin delineation from digital elevation data," *Geo-Processing*, vol. 2, pp. 299-311, 1984.

Abstract. While digital elevation grids are now in wide use, accurate delineation of drainage basins from these data is difficult to efficiently automate. We present a recursive "order N" solution to this problem. No point in the basin is checked more than once, and no points outside the basin are considered. Two applications for terrain analysis and one for remote sensing are given to illustrate the method, using a basin with high relief in the Sierra Nevada. This technique for automated basin delineation will enhance the utility of digital terrain analysis for hydrologic modeling and remote sensing.

5. Field and Laboratory Measurements of Snow Liquid Water by Dilution

This paper has been accepted for publication. The reference citation is:

Davis, R. E., J. Dozier, E. R. LaChapelle, and R. Perla, "Field and laboratory measurements of snow liquid water by dilution," *Water Resources Research*, 1985. In press

Abstract. Field trials of the dilution technique for measuring snow liquid water content show that the refined procedure is rapid and simple. Measurements of the liquid water mass fraction with an absolute error of $\sim$1.5% can be obtained by one operator at a rate of 10–15 samples per hour, but if the water content is low, 0–2%, the relative error can be high. Electrolytic conductivity is the preferred method for measuring concentrations, using a stock solution of 0.01 N HCl. The recommended amount of stock solution to add is 0.5–0.8 $\times$ the mass of the snow sample. Extraction of the resulting mixture of stock solution and snow liquid water is best done with a screened pipette, instead of by decanting.

6. Orthographic Terrain Views Using Data Derived from Digital Elevation Models

This paper has been submitted for publication. The reference citations are:

Dubayah, R. O., "Orthographic terrain views using data derived from digital elevation models," M. A. Thesis, Department of Geography, University of California, Santa Barbara, CA, 1985.

Dubayah, R. O. and J. Dozier, "Orthographic terrain views using data derived from digital elevation models," *Photogrammetric Engineering and Remote Sensing*. (Submitted 1985)

Abstract. A fast algorithm is present for producing three-dimensional orthographic terrain views using digital elevation data and co-registered imagery. These views are created using projective geometry and are designed for display on high resolution raster graphics devices. The algorithm's effectiveness is achieved by [1] the implementation of two efficient grey-level interpolation routines which offer the user a choice between speed and smoothness, and [2] a unique visible surface determination procedure based on horizon angles derived from the elevation data set.

7. Two-Stream Method for Radiative Transfer in Inhomogeneous Atmospheres over Irregular Surfaces

This paper has been submitted for publication. The reference citation is:

Dozier, J. and R. F. Milliff, "Two-stream method for radiative transfer in inhomogeneous atmospheres over irregular surfaces," *Journal of Geophysical Research*. (Submitted 1985)

Abstract. Two-stream approximations for solution to the radiative transfer equation in plane-parallel media can be extended to inhomogeneous atmospheres over irregular surfaces. For a homogeneous layer the two-stream equations are solved for an irregular boundary condition, which includes topographic effects and variation of reflectance with illumination angle. Direct and diffuse reflectances of this layer are then used as the boundary condition for the next upward layer, continuing recursively to the top of the atmosphere. Accuracy of the method compares favorably to more precise solutions, with standard errors of $\sim$1.5%.

8. A Component Decomposition Model for Evaluating Atmospheric Effects in Remote Sensing

8.1. Introduction

Images acquired by radiometric sensors on satellites are somewhat degraded compared to those from lower altitude platforms because of atmospheric effects. For better derivation of surface properties and classification of ground features, it is desirable to make constructive atmospheric corrections and retrieve the ground reflectance. It is also desirable to better understand the relationship between the properties of the atmosphere and surface and the upwelling radiance at the sensor's level. An atmospheric model with wide wavelength coverage is also useful for selection of optimal bands or band combinations in future remote sensing instruments. Here we describe an ultraviolet-through-infrared atmospheric component evaluation model for a plane-parallel atmosphere-earth system with arbitrarily nonuniform albedo, either Lambertian or anisotropic. Such a model can be used for testing simpler atmospheric correction models and selecting new wavelength bands for future sensors.

Many researchers [Ueno et al., 1978; Otterman and Fraser, 1979; Dave, 1980; Kaufman and Fraser, 1984] have noted that the radiance L received by a remote sensor is composed of three components: (1) directly transmitted ground signature, (2) diffusely transmitted ground radiation through the atmosphere, and (3) the atmospheric radiation that would occur even over a perfectly absorbing and non-emitting ground. Different researchers use different terminologies for these three components. Hereafter, we call them L_s (attenuated signal), L_d (diffusely transmitted ground radiation), and L_0 (pure atmospheric radiance). The physical meanings of these three components are depicted in Figure 8.1.

$$L = L_s + L_d + L_0 \tag{8.1}$$

Among these three components, L_s contains useful information that we want to retrieve from the remotely sensed data, while the other two degrade the satellite measurement and need to be removed.

L_0 is usually regarded as the result of scattering of sunlight. This is true for visible and shorter wavelengths, but in the more general case we can consider this as caused by both scattering and emission. For accurate calculation of L_0, multiple scattering should be included [Ueno et al., 1978].

The L_d term is difficult to calculate for a nonuniform surface, because radiation reflected from surface areas that are not within the instantaneous field of view (IFOV) of the sensor can arrive at the sensor by atmospheric scattering. Ueno et al. [1978] use the mean albedo of the neighborhood of the target pixel to correct for individual values. Pearce [1977] takes a backward-tracking Monte Carlo approach to solve this problem with given ground albedo patterns. He also introduces the concept of a point spread function and points out its importance in retrieving ground albedo by deconvolution. Otterman and Fraser [1979] look into the significance of adjacency effects by a single scattering approximation. Dave [1980] uses a more sophisticated version of first order scattering, the "primary scattering source function" model, to investigate the atmospheric effect caused by surface inhomogeneity. Kiang [1982] assesses the importance of atmospheric spreading effects on Landsat Multispectral Scanner and Thematic Mapper measurements using a procedure similar to Pearce's. Mekler and Kaufman [1982] develop a two-dimensional radiative transfer model in which a one-dimensionally varying surface can be handled. Kaufman and Fraser [1984] use Pearce's results and investigate the effect of L_d on classification accuracy.

While all these investigations confirm the existence of neighboring area effects caused by L_d, most of the approaches are forward models only, in that they calculate the upwelling radiance at the top of the atmosphere, given an atmospheric profile and surface albedo distribution, but they cannot retrieve the surface albedo distribution, given the atmospheric profile and top-of-atmospheric radiance. Kiang [1982] correctly looked into the physical meaning of the atmospheric spread function, but he did not further investigate its possible usage in retrieving ground reflectance. The method of Ueno et al. [1978] is an inverse method, but without support by the atmospheric point spread function, it is somewhat empirical [Dave, 1980]. Moreover, their atmospheric model was composed of only two layers and might be too simple.

Pearce's [1977] model is a forward one but can be used for the inverse problem in some special cases. The wavelength range for his model is in the solar spectrum only; atmospheric emission is not considered. The only surface type handled is Lambertian, and the point spread function is derived only for a nadir-pointing monochromatic sensor. Diner and Martonchik [1984] incorporate a spatial Fourier transform method and the standard one-dimensional radiative transfer technique for solving the three-dimensional transfer equation for a vertically inhomogeneous atmosphere sitting on an inhomogeneous non-Lambertian plane surface. So far, this method is a forward algorithm.

The development of a model for a wider wavelength range, handling both Lambertian and anisotropic surfaces and producing a point spread function for arbitrary sensor angles is the task we consider here. Given infomation about the atmospheric profile, surface reflectance can be retrieved from top-of-atmospheric radiance. The model therefore achieves a partial step toward solution of the surface remote sensing inversion problem — retrieval of surface reflection properties from upwelling radiance measurements alone.

8.2. Decomposition of Remotely Sensed Radiance

To understand the physical meaning of the components of the upward radiance, let us look at the decomposition in a layer-structured plane-parallel atmosphere. According to the interaction principle [Grant and Hunt, 1969] radiation is additive, and the upward radiance at the top of a layer, bounded by upper level τ_i and lower level τ_j, where $j = i+1$, is the sum of three components: reflection of top incident radiation, transmission of bottom incident radiation to the top, and the upward internal source emerging at the top. In vector notation,

$$\mathbf{L}^{\uparrow}(\tau_i) = \mathbf{R}(\tau_j,\tau_i)\,\mathbf{L}^{\downarrow}(\tau_i) + \mathbf{T}(\tau_i,\tau_j)\,\mathbf{L}^{\uparrow}(\tau_j) + \Sigma^{\uparrow}(\tau_i,\tau_j) \tag{8.2}$$

The **L**'s denote the vectors of downward and upward radiances in different directions at different levels τ_i and τ_j. **R** and **T** are reflectance and transmittance matrices, and $\Sigma^{\uparrow}$ is the upward internal source vector emerging at level τ_i.

This equation is a statement of radiation conservation. **R**, **T**, and $\Sigma^{\uparrow}$ are uniquely determined by the composition and status of the layer only; they are independent of the radiation impinging on the layer from outside. The **L** terms on the right hand side represent radiation coming from above or below the layer and can be caused by emission and reflection. They may include any interactions between the layer concerned and the adjacent layers. The decomposition of the transmittance term in (8.2) is a consequence of separation of direct from diffuse transmittance.

The first and third terms on the right hand side in (8.2) result in the L_0 term. For further separation, we consider general expressions for L_e and L_d first. Then we derive equations for the simpler cases. For an anisotropic inhomogeneous surface, the upward direct and diffuse components at the sensor, which points in direction $\vec{\Omega}$ are:

$$L_e = L^{\uparrow}(\tau,\vec{r},\vec{\Omega})\, e^{-\tau/\mu} \tag{8.3}$$

$$L_d = \iint_{A\,\Omega} T_d(0,\vec{r},\vec{\Omega};\tau,\vec{r}\,',\vec{\Omega}')\,L^{\uparrow}(\tau,\vec{r}\,',\vec{\Omega}')\,\mu'\, d\Omega'\, dA' \tag{8.4}$$

$\vec{\Omega}$ is composed of nadir angle $\cos^{-1}\mu$ and azimuth ϕ. $\vec{\Omega}$ and $\vec{\Omega}'$ are directional vectors, and $d\Omega$ is the differential of solid angle in direction $\vec{\Omega}$. Therefore $\int \quad d\Omega = \int\int d\mu\, d\phi$. The horizontal position vectors $\vec{r}$ and $\vec{r}'$ are expressed by x, y and x', y' for the horizontal positions of emerging and incident radiation pencils, and $dA' = dx'\, dy'$ is differential area. The "upward point-to-point bidirectional diffuse transmittance function" is

$$T_d(0,\vec{r},\vec{\Omega};\tau,\vec{r}',\vec{\Omega}') = \frac{dL^{\uparrow}(0,\vec{r},\vec{\Omega})}{d\,[\mu'\, E_d^{\uparrow}(\tau,\vec{r}')]} \tag{8.5}$$

This defines the contribution to the top-of-atmospheric radiance increment at the horizontal position $\vec{r}$ in direction $\vec{\Omega}$ made by an upwelling irradiance increment leaving from unit surface area in direction $\vec{\Omega}'$ at the horizontal position $\vec{r}'$. For a plane-parallel atmosphere and surface it is shift invariant: it depends on the difference $(\vec{r}' - \vec{r})$ and not on their individual values.

The expression for L_e (8.3) remains the same for simpler Lambertian or homogeneous surfaces, so only L_d is discussed below. For simpler cases, we first define the following quantities. The "upward point-to-point hemispherical-directional diffuse transmittance function" from subpoint $\vec{r}'$ to sensor is

$$T_d(0,\vec{\Omega};\tau,\vec{r}') = \int_{\Omega} T_d(0,\vec{\Omega};\tau,\vec{r}',\vec{\Omega}')\, \mu'\, d\Omega' \tag{8.6}$$

The "total upward plane-to-point hemispherical-directional diffuse transmittance coefficient" is

$$T_d(0,\vec{\Omega};\tau) = \int_{A'} T_d(0,\vec{\Omega};\tau,\vec{r}')\, dA' \tag{8.7}$$

For a Lambertian surface upwelling radiance at the surface is independent of viewing direction, i.e. $L^{\uparrow}(\tau,\vec{r}',\vec{\Omega}') = L^{\uparrow}(\tau,\vec{r}')$, and (8.4) simplifies to

$$L_d \equiv L_d(0,\vec{\Omega};\tau,\vec{r}) = \int_{A'} T_d(0,\vec{\Omega};\tau,\vec{r}' - \vec{r})\, L^{\uparrow}(\tau,\vec{r}')\, dA' \tag{8.8}$$

An averaged upwelling radiance for an atmosphere of total optical thickness τ at the bottom position $\vec{r}$ for a Lambertian surface is

$$\overline{L^{\uparrow}(\tau,\vec{r})} = \frac{\int_{A'} T_d(0,\vec{\Omega};\tau,\vec{r}' - \vec{r})\, L^{\uparrow}(\tau,\vec{r}')\, dA'}{T_d(0,\vec{\Omega};\tau)} \tag{8.9}$$

For a homogeneous Lambertian surface under uniform illumination $L^{\uparrow}(\tau,\vec{r}\,',\vec{\Omega}\,') = L^{\uparrow}(\tau)$. Therefore

$$L_d = L^{\uparrow}(\tau)\, T_d(0,\vec{\Omega};\tau) \tag{8.10}$$

Now it is interesting to consider an opposite configuration. If a narrow beam with irradiance E_0 is incident on a unit area at the top of the atmosphere, in the same direction as the sensor viewing axis, then $\mu_0 = \mu$ and the resulting diffuse radiance at the bottom is

$$L_d^{\downarrow}(\tau,\vec{r}\,',\vec{\Omega}\,';0,\vec{r},\vec{\Omega}) = \mu_0\, E_0\, T_d(\tau,\vec{r}\,',\vec{\Omega}\,';0,\vec{r},\vec{\Omega}) \tag{8.11}$$

and the diffuse irradiance at that location is

$$E_d^{\downarrow}(\tau,\vec{r}\,';0,\vec{r},\vec{\Omega}) = \int_{\Omega} L_d^{\downarrow}(\tau,\vec{r}\,',\vec{\Omega}\,';0,\vec{r},\Omega)\, \mu'\, d\Omega'$$

$$= \mu_0\, E_0 \int_{\Omega} T_d(\tau,\vec{r}\,',\vec{\Omega}\,';0,\vec{r},\vec{\Omega})\, \mu'\, d\Omega' \tag{8.12}$$

From the reciprocity principle [van de Hulst, 1980, pp. 16-18] $T_d(0,\vec{\Omega};\tau,\vec{r}\,') = T_d(\tau,\vec{r}\,';0,\vec{\Omega})$. Therefore

$$E_d^{\downarrow}(\tau,\vec{r}\,';0,\vec{r},\vec{\Omega}) = \mu_0\, E_0\, T_d(0,\vec{\Omega};\tau,\vec{r}\,'-\vec{r}) \tag{8.13}$$

The reciprocity relations among L, E, and T are presented in Figure 8.2.

Consider the convolution expression of L_d in equation (8.4). If the coordinates are chosen such that the zeros of $\vec{r}\,'$ are at the viewing axis of the sensor each time the radiance of the concerned pixel is recorded, then a new transmission function can be defined:

$$T(0,\vec{\Omega};\tau,\vec{r}\,',\vec{\Omega}\,') = \delta(\vec{r}\,')\,\delta(\vec{\Omega}-\vec{\Omega}\,')\,\frac{e^{-\tau/\mu}}{\mu} + T_d(0,\vec{\Omega};\tau,\vec{r}\,',\vec{\Omega}\,') \tag{8.14}$$

where δ is the delta function. Similarly, for a Lambertian surface, an integrated transmission function is

$$T(0,\vec{\Omega};\tau,\vec{r}\,') = \int_{\Omega} T(0,\vec{\Omega};\tau,\vec{r}\,',\vec{\Omega}\,')\, \mu'\, d\Omega' \tag{8.15}$$

Substituting T for T_d, we have

$$L - L_0 = \int_{A'} T(0,\vec{\Omega};\tau,\vec{r}\,')\, L^{\uparrow}(\tau,\vec{r}\,')\, dA' \tag{8.16}$$

According to reciprocity again, $T(0,\vec{\Omega};\tau,\vec{r}')$ equals the point spread function $T(\tau,\vec{r}';0,\vec{\Omega})$. Knowing L and L_0 and the point spread function we can solve for $L^{\uparrow}(\tau,\vec{r}')$ by a two dimensional deconvolution procedure [Andrews and Hunt, 1977]. This is the basis of applying a back-tracking atmospheric point spread function in restoration of remotely sensed images.

For a homogeneous, anisotropic surface, when the pattern of $L^{\uparrow}(\tau,\vec{r}',\vec{\Omega}')$ is independent of horizontal location $\vec{r}'$, as is shown in Figure 8.3, we have the following expression for it:

$$L^{\uparrow}(\tau,\vec{r}',\vec{\Omega}') = L_*^{\downarrow}(\tau,\vec{r}')\,\eta(\vec{\Omega}') \tag{8.17}$$

where η is an anisotropic reflectance factor. We define

$$t_{d,*}(0,\vec{\Omega};\tau,\vec{r}') = \int_{\Omega} T_d(0,\vec{\Omega};\tau,\vec{r}',\vec{\Omega}')\,\eta(\vec{\Omega}')\,\mu'\,d\Omega' \tag{8.18}$$

and

$$L_*^{\downarrow}(\tau,\vec{r}') = \frac{1}{\pi}\int_{\Omega} L^{\uparrow}(\tau,\vec{r}',\vec{\Omega}')\,\mu'\,d\Omega' \tag{8.19}$$

We can substitute $t_{d,*}$ for T_d in equation (8.14), and $L_*^{\downarrow}(\tau,\vec{r}')$ for $L^{\uparrow}(\tau,\vec{r}')$ in equation (8.16). Then solve $L_*^{\downarrow}(\tau,\vec{r}')$ in (8.16) by deconvolution.

For a simpler and somewhat empirical solution, go back to L_d and L_g. By estimating L_d locally, the individual upward ground radiances can be solved by

$$L^{\uparrow}(\tau,\vec{r},\vec{\Omega}) = (L - L_0 - L_d)\,e^{\tau/\mu} \tag{8.20}$$

L_0 and τ can be accurately calculated from a one-dimensional radiative transfer model, the details of which are described in a following section. The value of L_d can be estimated in the following way, by defining $\beta_d = L_d/L_g$ and $\beta = (L - L_0)/L_g$ for a homogeneous Lambertian surface:

$$L_d \approx \frac{\beta_d\,(\bar{L} - L_0)}{\beta} \tag{8.21}$$

8.3. Azimuthally Dependent Plane-Parallel Atmospheric Radiative Transfer Multiple Scattering

Azimuthally dependent radiance in an absorbing, emitting, and scattering layer is governed by the radiative transfer equation [Chandrasekhar, 1960]:

$$\mu \frac{dL(\tau,\vec{\Omega})}{d\tau} + L(\tau,\vec{\Omega}) = J(\tau,\vec{\Omega}) \tag{8.22}$$

Here, the sign convention is that the downward direction is positive. τ is optical depth, and $L(\tau,\vec{\Omega})$ is the radiance at level τ along direction $\vec{\Omega}$, which is composed of zenith angle $\cos^{-1}\mu$ and azimuth ϕ. The source function J is

$$J(\tau,\vec{\Omega}) = \frac{\tilde{\omega}}{4\pi} \int_{4\pi} P(\tau,\vec{\Omega};\vec{\Omega}')L(\tau,\vec{\Omega})\, d\Omega' + Q(\tau,\vec{\Omega}) \tag{8.23}$$

The phase function $P(\tau,\vec{\Omega};\vec{\Omega}')$ gives the distribution pattern of single scattering at τ caused by a pencil of radiation incident along direction $\vec{\Omega}'$ and scattered in direction $\vec{\Omega}$. The first term on the right hand side of (8.23) is then the total contribution made by radiation coming from all directions to the radiance at a particular direction $\vec{\Omega}$. The phase function is calculated by rapid Mie algorithms [Wiscombe, 1980].

The Q term in (8.23) represents an internal source. By separating direct from diffuse radiation, it is convenient to consider the radiation scattered from the direct beam and the specularly reflected direct beam as caused by some internal "pseudo-source" [Wiscombe, 1976a]. Then the total internal source is

$$Q(\tau,\vec{\Omega}) = Q_t(\tau,\vec{\Omega}) + Q_s(\tau,\vec{\Omega}) + Q_{sp}(\tau,\vec{\Omega}) \tag{8.24}$$

where Q_t is the thermal source and Q_s and Q_{sp} are the direct and specular "pseudo-sources." $\mathrm{B}[T(\tau)]$ is the Planck function.

$$Q_t(\tau,\vec{\Omega}) = (1-\tilde{\omega})\mathrm{B}[T(\tau)] \tag{8.25}$$

$$Q_s(\tau,\vec{\Omega}) = \frac{\tilde{\omega} E_0}{4\pi} P(\tau,\vec{\Omega};\vec{\Omega}_0)\, e^{-\tau/\mu_0} \tag{8.26}$$

$$Q_{sp}(\tau,\vec{\Omega}) = \frac{\tilde{\omega}}{4\pi} \rho_{sp}(\mu_0)\, P(\tau,\vec{\Omega};\vec{\Omega}_{sp})\, e^{-(2\tau_{sp}-\tau)/\mu_0} \tag{8.27}$$

μ_0 is the cosine of the solar zenith angle, E_0 is the solar irradiance incident on the top of the atmosphere (normal to the beam), ρ_{sp} is the directional specular reflectivity at the surface beneath the atmosphere, and τ_{sp} is the total optical thickness from top to the specular surface.

To resolve phase functions with strongly forward peaks using lower order polynomial approximation, a delta-M transformation is performed for the phase function moments, optical depth, and single scattering albedo [Wiscombe, 1977].

Interaction Principle

One way to attack this integro-differential equation (8.22) uses the previously mentioned "interaction principle" [Grant and Hunt, 1969]. In vector form, its expression for both upward and downward outward radiances from any arbitrary layer bounded by upper boundary τ_i and lower boundary τ_j, appears as

$$\mathbf{L}^{\downarrow}(\tau_j) = \mathbf{R}(\tau_i,\tau_j)\,\mathbf{L}^{\uparrow}(\tau_j) + \mathbf{T}(\tau_j,\tau_i)\,\mathbf{L}^{\downarrow}(\tau_i) + \mathbf{\Sigma}^{\downarrow}(\tau_i,\tau_j) \tag{8.28}$$

$$\mathbf{L}^{\uparrow}(\tau_i) = \mathbf{R}(\tau_j,\tau_i)\,\mathbf{L}^{\downarrow}(\tau_i) + \mathbf{T}(\tau_i,\tau_j)\,\mathbf{L}^{\uparrow}(\tau_j) + \mathbf{\Sigma}^{\uparrow}(\tau_i,\tau_j) \tag{8.29}$$

Radiances $\mathbf{L}^{\downarrow\uparrow}$ are vectors of $m \times n$ elements on a discrete angular space composed of m zenith and n azimuth angles at a given optical depth:

$$\mathbf{L}^{\downarrow\uparrow}(\tau) = \begin{bmatrix} L(\tau,\pm\mu_1,\phi_1) \\ L(\tau,\pm\mu_1,\phi_2) \\ \cdots\cdots \\ L(\tau,\pm\mu_m,\phi_n) \end{bmatrix} \tag{8.30}$$

$1 \geq \mu_1 > \cdots > \mu_m > 0$ are a set of quadrature points on (0,1) and $0 \leq \phi_1 < \cdots < \phi_n < 2\pi$ are equally spaced points in the interval 0–2π. The **R**'s and **T**'s are reflection and transmission matrices, and $\mathbf{\Sigma}^{\downarrow\uparrow}$ are internal source vectors. For a homogeneous thin layer, these quantities can be derived by some initialization scheme [Wiscombe, 1976b].

Adding/Doubling Method

By applying the interaction principle to two adjacent layers, the reflection and transmission matrices and the source vectors for the combined layer can be derived if the corresponding quantities are known for each of these two layers [Grant and Hunt, 1969].

Consider two adjacent layers with identical scattering properties bounded by planes at optical depths τ_1, τ_2, and τ_3. By the interaction principle, we have expressions for $\mathbf{L}^{\downarrow}(\tau_2)$, $\mathbf{L}^{\uparrow}(\tau_1)$, $\mathbf{L}^{\downarrow}(\tau_3)$, and $\mathbf{L}^{\uparrow}(\tau_2)$. Since τ_1, τ_2, τ_3 are entirely arbitrary, we consider a single layer bounded by τ_1 and τ_3, and we have new expressions for $\mathbf{L}^{\downarrow}(\tau_3)$ and $\mathbf{L}^{\uparrow}(\tau_1)$. Both old and new forms for $\mathbf{L}^{\downarrow}(\tau_3)$ and $\mathbf{L}^{\uparrow}(\tau_1)$ must be equivalent. Eliminating $\mathbf{L}^{\downarrow}(\tau_2)$ from the first set of expressions yields the reflection and transmission matrices and the internal source vectors for the combined layer in terms of quantities for the separate layers.

$$\mathbf{R}(\tau_3,\tau_1) = \mathbf{R}(\tau_2,\tau_1) + \mathbf{T}(\tau_1,\tau_2)\,[\mathbf{I} - \mathbf{R}(\tau_3,\tau_2)\,\mathbf{R}(\tau_1,\tau_2)]^{-1}\,\mathbf{R}(\tau_3,\tau_2)\,\mathbf{T}(\tau_2,\tau_1) \tag{8.31}$$

$$\mathbf{R}(\tau_1,\tau_3) = \mathbf{R}(\tau_2,\tau_3) + \mathbf{T}(\tau_3,\tau_2)\,[\mathbf{I} - \mathbf{R}(\tau_1,\tau_2)\,\mathbf{R}(\tau_3,\tau_2)]^{-1}\,\mathbf{R}(\tau_1,\tau_2)\,\mathbf{T}(\tau_2,\tau_3) \tag{8.32}$$

$$\mathbf{T}(\tau_3,\tau_1) = \mathbf{T}(\tau_3,\tau_2)\,[\mathbf{I} - \mathbf{R}(\tau_1,\tau_2)\,\mathbf{R}(\tau_3,\tau_2)]^{-1}\,\mathbf{T}(\tau_2,\tau_1) \tag{8.33}$$

$$\mathbf{T}(\tau_1,\tau_3) = \mathbf{T}(\tau_1,\tau_2)\,[\mathbf{I} - \mathbf{R}(\tau_3,\tau_2)\,\mathbf{R}(\tau_1,\tau_2)]^{-1}\,\mathbf{T}(\tau_2,\tau_3) \tag{8.34}$$

$$\begin{aligned}\mathbf{\Sigma}^{\downarrow}(\tau_1,\tau_3) = {} & \mathbf{T}(\tau_3,\tau_2)\,[\mathbf{I} - \mathbf{R}(\tau_1,\tau_2)\,\mathbf{R}(\tau_3,\tau_2)]^{-1}\,\mathbf{R}(\tau_1,\tau_2)\,\mathbf{\Sigma}^{\uparrow}(\tau_2,\tau_3) + \\ & \mathbf{T}(\tau_3,\tau_2)\,[\mathbf{I} - \mathbf{R}(\tau_1,\tau_2)\,\mathbf{R}(\tau_3,\tau_2)]^{-1}\,\mathbf{\Sigma}^{\downarrow}(\tau_1,\tau_2) + \mathbf{\Sigma}^{\downarrow}(\tau_2,\tau_3)\end{aligned} \tag{8.35}$$

$$\begin{aligned}\mathbf{\Sigma}^{\uparrow}(\tau_1,\tau_3) = {} & \mathbf{T}(\tau_1,\tau_2)\,[\mathbf{I} - \mathbf{R}(\tau_3,\tau_2)\,\mathbf{R}(\tau_1,\tau_2)]^{-1}\,\mathbf{R}(\tau_3,\tau_2)\,\mathbf{\Sigma}^{\downarrow}(\tau_1,\tau_2) + \\ & \mathbf{T}(\tau_1,\tau_2)\,[\mathbf{I} - \mathbf{R}(\tau_3,\tau_2)\,\mathbf{R}(\tau_1,\tau_2)]^{-1}\,\mathbf{\Sigma}^{\uparrow}(\tau_2,\tau_3) + \mathbf{\Sigma}^{\uparrow}(\tau_1,\tau_2)\end{aligned} \tag{8.36}$$

These are formulae for the "adding" method. If the two layers have identical optical thickness, the simpler "doubling" method results. If the initial layer is chosen such that $\Delta\tau = (\tau_{i+1} - \tau_i)/2^N$, where N is an integer and $(\tau_{i+1} - \tau_i)$ is the optical depth of the layer in the multi-layer system, then the reflection and transmission matrices and source vectors for the homogeneous thicker layer can be built up quickly by "doubling" N times. Note that internal sources are not constant with optical depth and need to be treated separately [Wiscombe, 1976a].

Calculation of the Internal Radiance

Knowing the reflection and transmission matrices and source vectors for each layer in the multi-layer system, we can build the internal radiance field in the atmosphere by the adding method. Using the formulae of the interaction principle, we have a set of simultaneous equations for levels $0 \le i \le k$, where k is the total number of layers in the system:

$$\mathbf{L}^{\downarrow}(\tau_{i+1}) = \mathbf{T}(\tau_{i+1},\tau_i)\,\mathbf{L}^{\downarrow}(\tau_i) + \mathbf{R}(\tau_i,\tau_{i+1})\,\mathbf{L}^{\uparrow}(\tau_{i+1}) + \mathbf{\Sigma}^{\downarrow}(\tau_i,\tau_{i+1}) \tag{8.37}$$

$$\mathbf{L}^{\uparrow}(\tau_i) = \mathbf{R}(\tau_{i+1},\tau_i)\,\mathbf{L}^{\downarrow}(\tau_i) + \mathbf{T}(\tau_i,\tau_{i+1})\,\mathbf{L}^{\uparrow}(\tau_{i+1}) + \mathbf{\Sigma}^{\uparrow}(\tau_i,\tau_{i+1}) \tag{8.38}$$

The top and bottom boundary conditions that need to be satisfied are that $\mathbf{L}^{\downarrow}(\tau_0)$ must be specified and

$$\mathbf{L}^{\uparrow}(\tau_k) = \mathbf{R}_G\,\mathbf{L}^{\downarrow}(\tau_k) + \vec{\epsilon}\,\mathrm{B}[T_G] + \frac{\mu_0 E_0}{\pi}\,e^{-\tau_k/\mu_0}\,\mathbf{f}_r(\mu_0) \tag{8.39}$$

$\mathbf{R}_G$ is the surface diffuse reflection matrix, $\vec{\epsilon}$ is the emissivity vector, $\mathbf{f}_r(\mu_0)$ is the BRDF (bidirectional reflectance-distribution function) vector for the incident beam, and T_G is the temperature of the surface.

A method to solve this set of equations is given by Grant and Hunt [1969]. Its essence is that the radiation is additive, so that we can first consider the case in which there is no radiation from the bottom of the current layer to get a partial radiance, and then take into account the remaining contribution caused by upward radiance from the bottom of each layer.

The method includes two passes. In the forward pass, the calculation starts at the top layer, then goes down. For each layer, only the partial radiances are calculated, which include the contribution made by the internal sources of the current layer plus that resulting from the downwelling radiation. Also, the cumulative reflection matrix and transmission-reflection matrix looking from the bottom are calculated for later use. This process is carried out until the ground surface is reached. At this point, a downward radiance over a nonreflecting, nonemitting surface $\mathbf{L}_b^{\downarrow}(\tau_k)$ has been obtained. For other surfaces the interaction between atmosphere and ground is

$$\mathbf{L}^{\downarrow}(\tau_k) = [\mathbf{I} - \mathbf{R}_A\,\mathbf{R}_G]^{-1}\left\{\mathbf{L}_b^{\downarrow}(\tau_k) + \mathbf{R}_A\left[\frac{\mu_0 E_0}{\pi}\; e^{-\tau_k/\mu_0}\,\mathbf{f}_r(\mu_0) + \vec{\epsilon}B(T_G)\right]\right\} \tag{8.40}$$

where $\mathbf{R}_A$ is the reflection of atmosphere looking from the bottom. The downward radiance can then be calculated from the bottom boundary condition (8.39).

This is followed by the backward pass carried out upwards, in which the contribution from the bottom of each layer is added to the previously computed partial radiances.

The upward radiance at the top of the atmosphere is

$$\begin{aligned}\mathbf{L}^{\uparrow}(\tau_0) = {} & \{\mathbf{R}(\tau_k,\tau_0) + \mathbf{T}(\tau_0,\tau_k)\,\mathbf{R}_G\,[\mathbf{I} - \mathbf{R}(\tau_0,\tau_k)\,\mathbf{R}_G]^{-1}\,\mathbf{T}(\tau_k,\tau_0)\}\,\mathbf{L}^{\downarrow}(\tau_0) + \\ & \Sigma^{\uparrow}(\tau_0,\tau_k) + \mathbf{T}(\tau_0,\tau_k)\,\mathbf{R}_G[\mathbf{I} - \mathbf{R}(\tau_0,\tau_k)\,\mathbf{R}_G]^{-1} \times \\ & \{\Sigma^{\downarrow}(\tau_0,\tau_k) + \mathbf{R}(\tau_0,\tau_k)\,[\vec{\epsilon}\,B(T_G) + \frac{\mu_0 E_0}{\pi}\; e^{-\tau_k/\mu_0}\,\mathbf{f}_r(\mu_0)]\}\end{aligned} \tag{8.41}$$

Fourier Transformation

In the azimuthally dependent case all vectors are organized in lexicographic ordering [Andrews and Hunt, 1977]. The related square matrices are matrices with circulant blocks [Davis, 1979]. For simplicity, we call them local circulant matrices. The results of operations of addition, scalar multiplication and matrix multiplication of local circulant matrices are still local circulant. Moreover if the inverse of a local circulant matrix exists, it is also a local circulant matrix. For operations involving such matrices and vectors, the Fourier transform can be used to save computation time. Since the matrices are only local circulant instead of complete or block circulant, the Fourier transform is performed locally to take care of the azimuthal dependence,

and the resulting coefficients of each order of Fourier transform can also be organized as matrices. The size of the resulting matrices and the length of the corresponding vectors are equal to the number of discretizations in the azimuth domain.

For Fourier transforms on discrete data, the general formulae to compute the coefficients for sine and cosine transforms are [Scheid, 1968]:

$$F_{st}(k+1) = h \sum_{j=0}^{n-1} f(j+1)\sin(2\pi jk/n) \tag{8.42}$$

$$F_{ct}(k+1) = h \sum_{j=0}^{n-1} f(j+1)\cos(2\pi jk/n) \tag{8.43}$$

where $k = 0,1,2,\cdots,\frac{1}{2}n$. For even functions, such as the phase function in the present work, all the sine coefficients are 0. The formula for the inverse Fourier transform is:

$$f(j+1) = d\ \{F_{ct}(1) + F_{ct}(\frac{n}{2}+1)(-1)^j + \tag{8.44}$$

$$2\sum_{k=1}^{\frac{n}{2}-1} [F_{ct}(k+1)\cos(2\pi jk/n) + F_{st}(k+1)\sin(2\pi jk/n)]\}$$

The product of the coefficients h and d in the above formulae should meet the relation $hd = 1/n$. If we choose $h = 1$, and $d = 1/n$, then for a unit matrix, the F_{ct}'s are all 1 for the diagonal subblocks and 0 elsewhere, i.e. the Fourier transform of an identity matrix is also an identity matrix. For computation, the Fast Fourier Transform method is used.

With $h = 1$, the Fourier transformation of a locally even circulant matrix is isomorphic. In other words, the forms of the original formulae remain unchanged, with the order of the matrix reduced. Under such transformation, the isomorphism covers the matrix operations of addition, scalar multiplication, multiplication, and inversion. This technique is equivalent to those used by Hansen and Travis [1974] and Dave and Gazdag [1970]. The computation time is reduced dramatically with the error introduced by the transformation of less than 10^{-7}. Note that the formula for the azimuthally averaged case is only the 0th order expression of the Fourier transform of the azimuthally dependent case.

8.4. Incorporation of LOWTRAN Calculations

As described thus far, the model is for the monochromatic case only. To make the model work for the atmosphere, we need to know the atmospheric optical properties. Among them the most important are optical thickness, τ, single scattering albedo, $\tilde{\omega}$, and the scattering phase functions.

The first two are related to the direct transmittance of the atmosphere. Given an atmospheric profile (temperature, pressure, water vapor density, ozone density, and the aerosol density and distribution) the LOWTRAN codes [Kneizys et al., 1983] and Mie scattering calculations give the atmospheric transmittance profile for wavelengths from 0.25–28.5 μm for every 20 cm^{-1} wavenumber interval. Unfortunately, the required τ and $\tilde{\omega}$ can not always be derived simply from the results of LOWTRAN, because a simple derivation makes the relation between the vertical optical thickness and slant optical length violate the cosine law that is essential for a one-dimensional radiative transfer model. The reason for this is that LOWTRAN does not really give monochromatic transmittance but instead averaged quantities over 20 cm^{-1} wavenumber intervals. This averaging causes violation of the Lambert-Bouguer-Beer law because of the complexity of molecular band absorption in longer wavelengths, even in a narrow wavenumber interval like 20 cm^{-1}. Since the total transmittance of a layer is the product of the average transmittances owing to molecular band absorption, molecular scattering, aerosol extinction, and molecular continuum absorption, the problem resulting from molecular band absorption causes trouble in calculation of the total transmittance and single scattering albedo for each layer.

A solution to this problem is the "exponential-sum fitting" method [Wiscombe and Evans, 1977] for radiative transmission functions calculated from LOWTRAN. For each of the three major absorbers (water vapor, ozone, and uniformly mixed gasses, which include CO_2, N_2O, CH_4, CO, O_2, and N_2) the exponential-fitting is performed to get equivalent absorption coefficients k_i, and weights a_i in this model, such that transmittance T_{mo} for a given absorber u is

$$T_{mo}(u) \approx \sum_{i=1}^{M} a_i \, e^{-k_i u} \tag{8.45}$$

When more then one major absorber exists, the combined effect, assuming random overlap of absorption lines from different absorbers, is

$$T_{mo}(\mathbf{U}) \approx \prod_{j=1}^{N} \sum_{i=1}^{M_j} a_{ji} \, e^{-k_{ji} u_j} \tag{8.46}$$

Here j represents one of N absorbers. U is a vector composed of $u_1, \cdots, u_N$. For the jth absorber, there are M_j expansion terms. Therefore, by expansion the total number of terms is $K = M_1 \cdots M_N$, with each having its own weight and power coefficient. The new weights and coefficients are

$$a_m' = \prod_{j=1}^{N} a_{jl_j} \tag{8.47}$$

$$k_m' = \sum_{j=1}^{N} k_{jl_j} \tag{8.48}$$

for $l_j = 1, \cdots, M_j$, and $m = 1, \cdots, K$. For each of these terms in the expansion, the monochromatic radiative transfer model can be used exactly.

9. Model Performance

Comparison with Özişik and Shouman [1980]

To verify our numerical code for a homogeneous lower boundary, we compare our results with those obtained by different methods. Özişik and Shouman [1980] presented exact solutions, calculated by the F_N method, of hemispherical reflectance and transmittance values for isotropic incident radiation on a two-layer model with isotropic scattering properties. Stamnes and Conklin [1984] compared their discrete ordinate method with the same calculations. Now we use the same calculations to verify our method over a variety of single scattering albedoes and optical thickness combinations. We use 4, 8, and 16 discretizations in the zenith domain and analytically integrate over azimuth for these comparisons. In Tables 1 and 2 we show the exact solutions and the 4-, 8-, and 16-stream results produced by different methods for reflectance and transmittance. Tables 3 and 4 offer the comparison of reflectances and transmittances for the same model with an underlying semi-transparent specular reflecting surface. It is shown that the 8- and 16-stream results from our model agree with exact solutions up to 3 or 4 decimal places. For intensities accuracy will be reduced by about one significant figure. Our results match those of Stamnes and Conklin [1984] to 4 decimal places in all cases but two; these minor exceptions are noted in Table 2.

Comparison with LOWTRAN6

In Table 5, we compare our results with LOWTRAN6 for the spectral interval 3–4 μm. The resulting upward radiances from LOWTRAN6 correspond to our results obtained when the constructive contribution of atmospheric scattering is intentionally omitted.

Computation Speed

To evaluate efficiency of our code, we use a 100-layer atmospheric model with total optical depth of 2 for computing radiance with 16 streams. Our model, coded in the C language, requires 80 sec CPU time on a Digital VAX 11/780 computer operating under the UNIX operating system. It is difficult to compare this value with other reported times, because the run time depends on the computational environment. But we can at least say that this speed is comparable with those of Stamnes and Conklin's [1984] discrete ordinate method, which takes 2 min 26 sec for the same atmosphere on the same model computer. Their model's computation time is independent of the total optical depth, but in remote sensing applications we are usually interested only in atmospheres with modest optical depths. Our code has the flexibility that the run time can be spent only on changed layers as long as we save intermediate results.

9.1. Atmospheric Point Spread Function

For a detailed investigation of diffusely transmitted ground radiation, the validity of a model using averaged ground albedo is open to challenge. Therefore, the atmospheric point spread function is studied. The PSF is the distribution pattern of the transmitted radiation of a pin-narrow beam through a degrading system. It is equivalent to the transmission in a three-dimensional model.

In the present model, the atmospheric point spread function is calculated by sparse sampling at some specific radii and polar angles. Then the results of the sampling are smoothed by a least-squares fitting procedure, and a rectangular PSF is produced from the parameters describing the curve chosen.

Point Spread Function Sampling Procedure

The procedure starts by shooting photons from the receiver in a specified direction. The PSF is then sparsely sampled on the ground in a polar coordinate system. For each sample element, two distinct sampling procedures are performed. For a Lambertian surface only the total number of photons that hit the element is recorded. For an anisotropic surface, the angular distribution of transmitted photons is recorded for each discrete direction. The angular discretization is exactly the same as for the radiative transfer model described in the previous section.

Single Scattering Approximation of Point Spread Function

For a thin atmosphere, multiple scattering is negligible, therefore a first order scattering approximation is appropriate. The approximation is similar to Dave's [1980] primary scattering

source function model except for the following three points: (1) Dave's approach is forward-tracking while this model is backward-tracking [Pearce, 1977]. (2) Dave's is ground albedo pattern dependent. (3) Dave does the complete integration over the entire ground surface in contrast to our sparse sampling approach.

From a beam of N photons originating at the sensor, the number lost from the beam traveling between τ/μ and $(\tau+\Delta\tau)/\mu$ is

$$\Delta N_e(\tau,\tau+\Delta\tau) = N\left[e^{-\tau/\mu} - e^{-(\tau+\Delta\tau)/\mu}\right] \tag{9.49}$$

Among these, the number lost by scattering is

$$\Delta N_s(\tau,\tau+\Delta\tau) = \Delta N_e(\tau,\tau+\Delta\tau)\,\overline{\tilde{\omega}(\tau,\tau+\Delta\tau)} \tag{9.50}$$

The contribution of these photons to the ground sample element is

$$\Delta N(\tau_g,\vec{r},\vec{\Omega}') = \Delta N_s(\tau,\tau+\Delta\tau)\,\frac{\Delta\Omega}{4\pi}\times$$

$$P\left(\tau+\frac{\Delta\tau}{2},\vec{\Omega},\vec{\Omega}'\right)\exp\left[-\frac{\tau_g-\tau-\Delta\tau/2}{\mu'}\right] \tag{9.51}$$

where the exponential factor is due to the attenuation between the scattering location and the sampling element. $\Delta\Omega$ is the solid angle increment covering the sampling element with respect to the point $\tau+\Delta\tau/2$. When $\vec{\Omega}\approx\vec{\Omega}'$ and $\Delta\Omega$ is almost 4π, special care needs to be taken to avoid exaggeration of the contribution because of the strong forward peak of the phase function.

For a Lambertian surface, the contributions made by different intervals for a particular sampling element are added to get the total contribution of the beam at the location. For an anisotropic surface, the contribution from different intervals are grouped according to the angular discretization of the hemisphere. In this way, the point spread function for a single scattering approximation is calculated.

Monte Carlo Method for Multiple Scattering

The essence of the Monte Carlo method is that the scattering and absorption of photon bundle can be statistically simulated by a sequence of random collisions before finally the bundle is exhausted by absorption or escape. After collision, some portion of the photon bundle is absorbed, and the remaining portion may change the direction of motion by scattering. Each scattering or absorption is a random collision event, but the general trend is governed by probability functions of the processes.

In this approach, the atmospheric optical parameters are the same as in the one-dimensional model. However, only the transmission problem is treated by Monte Carlo techniques, because the pure atmospheric radiance distribution has already been solved for a plane-parallel atmosphere. The problem is to find the contributions of the surface upwelling radiance to the signature of a certain pixel; included are the directly transmitted radiance from the pixel and the diffuse transmission of the ground upwelling radiance. By the reciprocity principle, the pattern of the contributions made by the ground radiation can be mimicked by a reverse process, in which a beam of photons impinges at a given point at the top of the atmosphere and finally some of them hit the bottom and make a spread pattern on it, which is the point spread function. According to the interaction principle, the transmission of a layer depends only on its properties and has nothing to do with the incident radiation. The radiation interaction between layers can only change the amount of incident radiation, but can not change layer transmission functions. Therefore to calculate the transmission or point spread function, we need only consider the case in which a photon hits the ground once.

In this model, the general procedures outlined by House and Avery [1969] are followed with some improvements made by Pearce [1977] included: the concept of photon bundle and photon fraction, and the separation between a real scattering and a sampling of the contribution made by a scatterer. The photon bundle concept looks at a photon as a bundle of photons and allows the investigator to deal with a fraction of the bundle instead of an unseparable whole photon each time. In this way, an absorbing atmosphere can be easily dealt with. The real scattering simulates the random walk process of a single photon in a scattering and absorbing layer. For each scattering event within the atmospheric layer the contribution to the point spread function is calculated. In other words, the sampling is not made when the photon hits the ground, instead it is made when a scattering occurs, because the diffuse radiance can be more accurately calculated from the integration of the source contributions along the given path than by direct sampling. Such a sampling method requires many fewer incident photons.

To mimic the random walk process, we need the distance traveled by the photon between two random collision events, the direction of each path, the portion of the photon bundle remaining after each collision, and the position of the photon in three-dimensional space. The following sections give the mathematical expressions of these events and quantities. Similar descriptions can be found in some representative papers [Cashwell and Everett, 1959; House and Avery, 1969; Pearce, 1977].

Free path length. The distance traveled by photon bundle between collisions is called the free path length. Measured in the same manner as the optical depth, it is dimensionless and is called optical distance. The probability density function of noncollision for an optical distance l is

$$p(l) = e^{-l} \tag{9.52}$$

Then the probability that no collision occurs in the range of optical distance from 0 to l is

$$r_1 = \int_0^l p(l')\, dl' = 1 - e^{-l} \tag{9.53}$$

where r_1 is a uniformly distributed random number between 0 and 1. This equation sets up a unique relation between a random number and an optical distance l:

$$l = -\ln(1-r_1) = |\ln(1-r_1)| \tag{9.54}$$

Direction of scattering. For each scattering event, two independent angular variables can be obtained from the random process, the scattering angle Θ and the azimuth angle Φ that is measured in the plane perpendicular to the original direction θ_1,ϕ_1.

The scattering angle Θ is determined in the following way. First define

$$P(\Theta) = \int_0^\Theta p(\Theta')\sin\Theta'\, d\Theta' \tag{9.55}$$

where Θ' is a dummy variable and $p(\Theta')$ is the phase function for scattering angle Θ' for the current scattering sublayer. Because the integration of $p(\Theta')$ over the range from 0 to π is 2, we need to multiply $P(\Theta')$ by 0.5 to normalize it. Then we can relate such a normalized quantity to a random number r_2 to determine the scattering angle Θ:

$$P(\Theta) = 2\, r_2 \tag{9.56}$$

The angle Φ is within the range from 0 to 2π; therefore

$$\Phi = 2\pi r_3 \tag{9.57}$$

where r_3 is another random number. Knowing the original direction θ_1,ϕ_1, and the scattering angle and azimuth Θ and Φ, the direction for the next path θ_2,ϕ_2 can be determined from analytic geometry [Marchuk et al., 1980]:

$$\cos\theta_2 = \cos\theta_1 \cos\Theta - \sin\theta_1 \sin\Theta \cos\Phi \tag{9.58}$$

$$\tan\phi_2 = \frac{\cos\theta_1 \sin\phi_1 \sin\Theta \cos\Phi + \cos\phi_1 \sin\Theta \sin\Phi + \sin\theta_1 \sin\phi_1 \cos\Theta}{\cos\theta_1 \cos\phi_1 \sin\Theta \cos\Phi - \sin\phi_1 \sin\Theta \sin\Phi + \sin\theta_1 \cos\phi_1 \cos\Theta} \tag{9.59}$$

The portion of a photon bundle remaining. After a collision, a portion of the photon bundle is absorbed and the remaining portion changes direction by scattering. If the scattered portion does not travel horizontally, some of it may escape from the medium. Therefore, if the original portion before the scattering is f_1 and the scattering takes place at τ within the medium of the total optical depth τ^*, then the remaining portion that is subject to the next scattering is

$$\begin{aligned} f_2 &= \tilde{\omega} f_1 (1 - e^{-\tau/|\cos\theta_2|}) && \text{for } \theta_2 > \frac{\pi}{2} \\ f_2 &= \omega f_1 (1 - e^{-(\tau^* - \tau)/(\cos\theta_2)}) && \text{for } 0 \le \theta_2 < \frac{\pi}{2} \\ f_2 &= \tilde{\omega} f_1 && \text{for } \theta_2 = \frac{\pi}{2} \end{aligned} \tag{9.60}$$

The remaining portion f_2 will still travel within the medium. The travel distance related to random number r_1 can be determined from a transformed version of (9.54):

$$l = \left| \ln \left[1 - r_1 \left(\frac{f_2}{\tilde{\omega} f_1} \right) \right] \right| \tag{9.61}$$

Such a process is repeated until the remaining portion is too small to be of any significance.

Distance of penetration of photon in the slab. In terms of optical depth, the penetration is determined by

$$\Delta\tau = l \cos\theta_2 \tag{9.62}$$

$$\tau_2 = \tau_1 + \Delta\tau \tag{9.63}$$

where l is the optical distance, τ_1 and τ_2 are the optical depths for the two successive collisions, and $\Delta\tau$ is the increment of optical depth between the two collisions. The height at which the collision occurs can be calculated from the relation between the optical depth and the height according to atmospheric profile. Suppose the heights for two successive collisions are h_1 and h_2, the distance traveled between collisions is

$$d = (h_2 - h_1) / \cos\theta_2 \tag{9.64}$$

Horizontal displacement. The horizontal displacement can then be calculated:

$$\Delta x = d \sin\theta_2 \cos\phi_2 \tag{9.65}$$

$$\Delta y = d \sin\theta_2 \sin\phi_2 \tag{9.66}$$

where Δx and Δy are the increments in Cartesian coordinates. The horizontal location x_2, y_2 can be derived given the location before traveling:

$$x_2 = \Delta x + x_1 \tag{9.67}$$

$$y_2 = \Delta y + y_1 \tag{9.68}$$

Sampling the PSF. The sampling procedures are the same as that for the first order scattering except that the scattering can be of any order and can take place not only along the path of the the direct beam but also any place outside that particular path. For the anisotropic case, the direction of contribution can be over the entire upper hemisphere.

Point Spread Function Smoothing, Curve Fitting and Interpolation

The point spread function produced from the Monte Carlo method is not perfectly smooth because of the statistical nature of the Monte Carlo procedure. Therefore, some curve fitting should be performed to apply the results in radiance retrieval.

One form that might be used is the normal distribution curve and its two-dimensional extension, for their wide use in the statistics and easy calculation of integrals over infinite range. However, we find that the normal curve gives low values on the outskirt of the PSF. A better choice is to look for the best fitting curve over a wide range of curves. A formula suitable for this purpose is:

$$f(x) = \frac{1}{(A + B\,|x|^D)^C} \tag{9.69}$$

where A, B, C, and D are the parameters to be determined in the fitting. This formula is chosen is for several reasons: (1) When the parameters A, B, C, and D are positive, the value of $f(x)$ decreases with increasing absolute value of x. In other words, the curve takes a bell or near-bell shape. (2) When D is 2, $A/B = 2C-1$. If A/B is an integer, it includes the t-distribution curves, often used in statistics The t-distribution curves, in turn, include normal distribution curves when the degrees of freedom approach infinity. Therefore, if a normal distribution curve or a t-distribution curve best fits the polar profile of PSF, then using this formula we can find it. (3) The integral of the volume under the bell surface for the x range 0–∞ (which represents the total point-plane directional-hemispherical transmittance function) is convergent when $C > 1$.

For an obliquely viewing sensor position, the PSF is not symmetric with respect to the vertical axis and is polar angle dependent. Therefore, it is not appropriate to use a single curve to fit

the PSF in all the polar angles. Instead, for each polar angle, a specific curve is fitted. Then the volume of each piece of the PSF-bell for each polar angle, as well as the total volume of the non-symmetric bell curve can be found.

Application of Point Spread Function in Image Processing

After removing L_0, we have the following relation:

$$g(x,y) = L(x,y) - L_0 = \sum_{x_1}\sum_{y_1} L_g(x-x_1, y-y_1)\, h(x_1,y_1) + e_n(x,y) \tag{9.70}$$

This states that the ground contribution is a convolution of atmospheric PSF and the ground upward radiances plus a noise term $e_n(x,y)$ If the PSF $h(x_1,y_1)$ is known, $L_g(x,y)$ can be retrieved by deconvolution [Andrews and Hunt, 1977].

The above expression is for an individual pixel. For an image, using the lexicographic form we can express a two-dimensional array as a vector by stacking columns for g, L and e_n. Also, we can construct a matrix **H** from the PSF h such that the size of **H** is comparable to that of **g**, **L** and $\mathbf{e_n}$ vectors. Then for the above relation over the entire image, we have

$$\mathbf{g} = \mathbf{H}\,\mathbf{L_g} + \mathbf{e_n} \tag{9.71}$$

This is a system of linear equations. When the noises $e_n(x,y)$ are 0, the ground upward radiance is given by an inverse filter:

$$\mathbf{L_g} = [\mathbf{H}]^{-1}\,\mathbf{g} \tag{9.72}$$

Fourier transform techniques are often used in this inverse filtering [Andrews and Hunt, 1977]. In the current investigation, we use another technique, the "constrained least squares" algorithm [Hunt, 1973], to handle nonzero noise with the aid of the Fourier transform. When the inner product of $\mathbf{e_n}$, i.e. $\mathbf{e_n}^T\,\mathbf{e_n}$, is estimated based on the mean and the standard deviation of the signal-to-noise-ratio of the sensor, this technique results in an estimation of ground upward radiance $\hat{\mathbf{L}}_\mathbf{g}$ that gives the smoothest solution for given $\mathbf{e_n}^T\,\mathbf{e_n}$. In other words, minimize $\hat{\mathbf{L}}_\mathbf{g}^T\,\mathbf{C}^T\,\mathbf{C}\,\hat{\mathbf{L}}_\mathbf{g}$ subject to $[\mathbf{g} - \mathbf{H}\,\hat{\mathbf{L}}_\mathbf{g}]^T\,[\mathbf{g} - \mathbf{H}\hat{\mathbf{L}}_\mathbf{g}] = \mathbf{e_n}^T\,\mathbf{e_n}$. The matrix **C** is produced from a two-dimensional Laplacian operator and is of the same size as matrix **H**. By Lagrangian method, the solution is

$$\hat{\mathbf{L}}_\mathbf{g} = [\mathbf{H}^T\,\mathbf{H} + \gamma\,\mathbf{C}^T\,\mathbf{C}]^{-1}\,\mathbf{H}^T\,\mathbf{g} \tag{9.73}$$

γ is the Lagrangian factor that need not be solved explicitly.

9.2. Example – Atmospheric Effects in Landsat Thematic Mapper Images

In this section we analyze the values of the three radiance components for six Thematic Mapper (TM) bands in visible and near-infrared regions, and we display the point spread function used for atmospheric correction of TM band-1 images. Finally, an image of expected ground upwelling radiances is retrieved from the remotely sensed TM band-1 image using that point spread function.

Three Radiance Components for a Standard Atmospheric Profile

We chose the U.S. Standard Atmosphere [1976] with a 13-layer structure as the input atmosphere for our model because it represents an average condition for the mid-latitudes. The major properties and parameters of this atmosphere are shown in Table 6. The sun is assumed at the average sun-earth distance with the solar zenith angle at 53.7 °. The sensor is at the nadir position.

Under such conditions, the three components L_e, L_d, and L_0 are calculated for different albedoes (1.0, 0.8, 0.5, 0.2, 0.0). For a given atmosphere L_0 depends on the incident solar condition only, whereas L_d and L_e depend on the albedo. However, for a homogeneous Lambertian surface the ratios $\beta_e = L_e / L_g$ and $\beta_d = L_d / L_g$ remain constant no matter what the albedo is. In the visible wavelength range we find that for each wavenumber interval of 300 cm^{-1} the relation that $T_d(0,\vec{\Omega};\tau) = T_d(\tau,\vec{\Omega};0)$ holds quite well, because the absence of molecular absorption make those individual wavenumber intervals close to monochromatic cases. But in the near-infrared, the wide wavelength bands do not allow the monochromatic reciprocity relation to be applied, since the complexity of strong CO_2 and O_2 absorption makes it completely unsuitable to approximate such bands by monochromatic wavelengths. The difference is caused by the change of spectral distribution of the radiation within the wavelength interval concerned, after passing through the atmosphere once. For the purpose of atmospheric correction, the term $T_d(0,\vec{\Omega};\tau)$ instead of $T_d(\tau;\Omega)$ is used, since that term mimics the upwelling transmission better.

In Table 6, the terms L_0, α, β_e, and β_d for the 6 TM bands in the reflective solar spectrum are listed. These values are wavelength averaged, with the involved radiance values weighted by sensor response function Υ_λ and wavelength interval.

$$\bar{L} = \frac{\int_\lambda \overline{L_\lambda}\, \Upsilon_\lambda \, d\lambda}{\int_\lambda \Upsilon_\lambda \, d\lambda} \tag{9.74}$$

From Table 6, it is obvious that for shorter wavelengths, the terms L_0 and β_d have larger values than those in the longer wavelengths. Since β_d represents the total contribution of the diffusely transmitted ground radiation to the sensor-received radiance for a uniform Lambertian surface, it is an indicator of the magnitude of the adjacency effect. In TM bands 5 and 7, β_d and the ratio $\alpha = \beta_d / \beta_e$ are small, and the adjacency effect may be neglected even for nonuniform, anisotropic surfaces.

Point Spread Functions

The shapes of point spread functions of six bands of Thematic Mapper are shown in Figure 9.4. The integrals of the point spread function for shorter TM bands (1-4) are close to their $\beta_e + \beta_d$ sums (let $\beta = \beta_e + \beta_d$ and note that $\beta = (L - L_0)/L_g$). This shows: (1) the results of Monte Carlo procedure are comparable to those from adding/doubling; (2) the reciprocity principle holds for each narrow spectral interval. However, for some wavelengths within TM bands 5 and 7, the integrals of point spread function even for narrow intervals differ considerably from the β value when both values are comparatively small. The reason for this is that for such intervals, the monochromatic assumptions are no longer valid because of the complexity of molecular absorption. Our point spread function for each narrow interval is simulated by downward tracking, starting with a smoothed solar spectrum, but the β values are calculated based on spectrally averaged upward transmissivities for each interval. The upward reflected photons have experienced longer atmospheric paths; therefore a higher portion have high penetration in the atmosphere than do the original downward spreading photons. Under such circumstances, a desirable point spread function cannot be obtained without renormalization. Fortunately, the effect of scattering at those two TM bands is negligible. A simpler atmospheric correction using L_0 and α will produce a good approximation for the radiance at ground level.

Image Restoration

Figure 9.5 shows the original images and the equivalent images restored by the "constrained least squares" technique. The resulting images in TM bands 1 and 2 are much sharper than the originals. Figure 9.6 also shows a set of restored images using a simpler technique in which the averaged neighborhood radiance values are used in association with the β_d value. A comparison shows that for TM band 2 the two restoration techniques give little difference.

9.3. Notation

$B[T]$	Planck function at temperature T (W $m^{-2}\mu m^{-1}sr^{-1}$)
E_0	solar constant (W $m^{-2}\mu m^{-1}$)
$E_d^{\downarrow}(\tau,\vec{r})$	downward diffuse irradiance at optical depth τ, location $\vec{r}$ (W $m^{-2}\mu m^{-1}$)
$E_d^{\uparrow}(\tau,\vec{r})$	upward diffuse irradiance at optical depth τ, location $\vec{r}$ (W $m^{-2}\mu m^{-1}$)
$E_e(\tau)$	downward direct irradiance at optical depth τ (W $m^{-2}\mu m^{-1}$)
$\mathbf{e_n}$	lexicographic noise vector
$e_n(x,y)$	noise term at pixel located at x,y
$f_r(\mu_0;\mu,\phi)$	BRDF (bidirectional reflectance-distribution function) for incidence angle $\cos^{-1}\mu_0$, reflection angle $\cos^{-1}\mu$, and reflection azimuth ϕ, measured from azimuth of illumination (sr^{-1})
$\mathbf{f}_r(\mu_0)$	BRDF vector for incidence angle $\cos^{-1}\mu_0$ (sr^{-1})
F_{ct}	Fourier cosine coefficient
F_{st}	Fourier sine coefficient
$\mathbf{g}$	lexicographic vector of radiances measured by sensor
$g(x,y)$	radiances measured by sensor
$\mathbf{H}$	lexicographic vector of point spread functions
$h(x,y)$	element of point spread function at location x,y
$\mathbf{L}^{\downarrow}(\tau_i)$	vector of downward radiances at level i (W $m^{-2}\mu m^{-1}sr^{-1}$)
$\mathbf{L}^{\uparrow}(\tau_i)$	vector of upward radiances at level i (W $m^{-2}\mu m^{-1}sr^{-1}$)
$\mathbf{L}_b^{\downarrow}(\tau_K)$	vector of downward radiances over a black and nonemitting surface (W $m^{-2}\mu m^{-1}sr^{-1}$)
$\hat{\mathbf{L}}_g$	vector of expected or estimated ground radiances (W $m^{-2}\mu m^{-1}sr^{-1}$)
$L(\tau,\vec{\Omega})$	radiance at level τ along direction $\vec{\Omega}$ (W $m^{-2}\mu m^{-1}sr^{-1}$)
L_0	pure atmospheric radiance (W $m^{-2}\mu m^{-1}sr^{-1}$)
L_d	diffusely transmitted ground radiation at sensor's level (W $m^{-2}\mu m^{-1}sr^{-1}$)
L_g	ground upwelling radiance (W $m^{-2}\mu m^{-1}sr^{-1}$)
L_s	attenuated signal at sensor's level (W $m^{-2}\mu m^{-1}sr^{-1}$)

$\overline{L^{\uparrow}(\tau)}$	averaged upward radiance from nonuniform Lambertian surface at ground level (W $m^{-2}\mu m^{-1}sr^{-1}$)
$\mathbf{P}$	matrix of phase functions
$P(\tau,\vec{\Omega},\vec{\Omega}')$	phase function at optical depth τ, from direction $\vec{\Omega}$ to $\vec{\Omega}'$
$\mathbf{R}$	reflectance matrix
$\mathbf{R}_G$	surface diffuse reflection matrix
$\mathbf{R}_A$	reflection of atmosphere looking from the bottom
$\vec{r}$	horizontal position vector
T_G	temperature of the surface (°K)
$\mathbf{T}$	transmittance matrix
$T(0,\vec{\Omega};\tau,\vec{r}')$	hemispherical-directional upward transmittance from a point $\vec{r}$ at bottom to sensor
$T(\tau,\vec{r}';0,\vec{\Omega})$	directional-hemispherical downward transmittance from sensor to a ground point at location $\vec{r}$
$T_d(0,\vec{\Omega};\tau,\vec{\Omega}')$	upward plane-to-point bidirectional diffuse transmittance function
$T_d(0,\vec{\Omega};\tau,\vec{r})$	upward point-to-point hemispherical-directional diffuse transmittance function
$T_d(0,\vec{\Omega};\tau,\vec{r},\vec{\Omega}')$	shift invariant upward point-to-point bidirectional diffuse transmittance function
$T_d(0,\vec{r},\vec{\Omega};\tau,\vec{r}',\vec{\Omega}')$	upward point-to-point bidirectional diffuse transmittance function
$T_d(\tau,\vec{r}',\vec{\Omega}';0,\vec{r},\vec{\Omega})$	downward point-to-point bidirectional diffuse transmittance function
$T_d(\tau,\vec{r}';0,\vec{\Omega})$	downward point-to-point directional-hemispherical diffuse transmittance function
$T_d(\tau,\vec{\Omega})$	downward beam diffuse transmission at ground level
$T_d(0,\vec{\Omega};\tau)$	total upward plane-to-point hemispherical-directional diffuse transmission coefficient
$T_{mo}(u)$	molecular transmittance for given absorber u
$T_{mo}(\mathbf{U})$	molecular transmittance for a set of absorbers $\mathbf{U}$

$\mathbf{U}$	a set of molecular absorbers composed of $(u_1, \cdots, u_N)$
α	ratio L_d/L_e
β	ratio $(L-L_0)/L_e$
β_d	ratio L_d/L_e
β_e	ratio L_e/L_e
$\vec{\varepsilon}$	emissivity vector
δ	delta function.
$\eta(\mu_0;\mu,\phi)$	anisotropic reflectance factor, defined as $\dfrac{\pi f_r(\mu_0;\mu,\phi)}{\int_0^{2\pi}\int_0^1 \mu' \; f_r(\mu_0;\mu',\phi')\, d\mu' \; d\phi'}$
γ	Lagrangian factor
λ	wavelength (μm)
μ	cosine of zenith angle θ
$\vec{\Omega}$	directional vector in three-dimensional space
$d\Omega$	differential of solid angle in direction $\vec{\Omega}$ (sr)
$\tilde{\omega}$	single scattering albedo
Φ	scattering azimuth angle measured in new coordinates
ϕ	azimuth angle, normally measured from direction of illumination
ρ_{sp}	directional specular reflectivity
$\Sigma^{\downarrow}$	downward internal source vector (W $m^{-2}\mu m^{-1}sr-1$)
$\Sigma^{\uparrow}$	upward internal source vector (W $m^{-2}\mu m^{-1}sr^{-1}$)
τ_i	optical depth at level i, measured from top
Θ	scattering angle between incident and scattering directions
θ	zenith angle
θ_v	observation zenith angle
Υ	sensor response function

9.4. Tables

Table 9 1 Comparison of Reflectance Results for a Two-Layer Model with Exact Calculations from Ozişik and Shouman [1980]

$\tilde{\omega}_1$	$\tilde{\omega}_2$	τ_1	τ_2	4-stream	8-stream	16-stream	exact
0.8	0.95	0 25	0 25	0 2292	0 2251	0 2252	0 2252
0.8	0.7	0.25	0 25	0 1987	0 1938	0 1939	0 1939
0.6	0.5	0 25	0 25	0 1316	0 1278	0 1278	0 1278
0.5	0 3	0 25	0 25	0 0963	0 0930	0 0930	0 0930
0.8	0.95	0.5	0 5	0 3066	0 3057	0 3056	0.3056
0.8	0 7	0.5	0 5	0 2687	0 2662	0 2662	0 2662
0.6	0.5	0 5	0 5	0 1682	0 1662	0 1661	0 1661
0.5	0.3	0 5	0.5	0 1241	0 1219	0 1219	0 1219
0.8	0.95	1	1	0 3518	0 3509	0 3509	0 3509
0.8	0.7	1	1	0 3184	0 3172	0 3172	0 3172
0.6	0.5	1	1	0.1891	0 1877	0 1877	0 1877
0.5	0.3	1	1	0.141[illegible]	0.1398	0 1398	0 1398
0.8	0.95	1	2	0.3797	0.3786	0 3786	0 3786
0.8	0 7	1	2	0.3247	0.3234	0.3234	0.3234
0.6	0.5	1	2	0.1907	0.1892	0 1892	0.1892
0.5	0.3	1	2	0.1417	0.1403	0 1402	0 1402
0.8	0.95	2	1	0 3451	0.3438	0 3438	0.3438
0.8	0.7	2	1	0 3373	0.3362	0.3362	0.3362
0.6	0.5	2	1	0.1951	0.1937	0.1937	0.1937
0 5	0.3	2	1	0.1471	0.1458	0 1457	0.1457

Table 9.2 Comparison of Transmittance Results for a Two-Layer Model with Exact Calculations from Ozişik and Shouman [1980]

$\tilde{\omega}_1$	$\tilde{\omega}_2$	τ_1	τ_2	4-stream	8-stream	16-stream	exact
0.8	0.95	0.25	0.25	0.6451	0.6504	0.6503	0.6503
0.8	0.7	0.25	0.25	0.6001	0.6053	0.6051	0.6051
0.6	0.5	0.25	0.25	0.5424	0.5476	0.5474	0.5474
0.5	0.3	0.25	0.25	0.5077	0.5131	0.5128	0.5128
0.8	0.95	0.5	0.5	0.4581	0.4597	0.4597	0.4597
0.8	0.7	0.5	0.5	0.3922	0.3926	0.3927	0.3927
0.6	0.5	0.5	0.5	0.3218	0.3205	0.3206	0.3206
0.5	0.3	0.5	0.5	0.2858	0.2834	0.2835	0.2835
0.8	0.95	1	1	0.2481	0.2476	0.2476[a]	0.2476
0.8	0.7	1	1	0.1758	0.1745	0.1745	0.1745
0.6	0.5	1	1	0.1184	0.1164	0.1164	0.1164
0.5	0.3	1	1	0.0953	0.0930	0.0930	0.0930
0.8	0.95	1	2	0.1603	0.1600	0.1600[b]	0.1600
0.8	0.7	1	2	0.0749	0.0745	0.0745	0.0745
0.6	0.5	1	2	0.0422	0.0420	0.0419	0.0419
0.5	0.3	1	2	0.0302	0.0301	0.0301	0.0301
0.8	0.95	2	1	0.1209	0.1205	0.1205	0.1205
0.8	0.7	2	1	0.0850	0.0846	0.0846	0.0846
0.6	0.5	2	1	0.0457	0.0454	0.0454	0.0454
0.5	0.3	2	1	0.0340	0.0338	0.0338	0.0338

[a] 0.2477 in Stamnes and Conklin [1984]

[b] 0.1601 in Stamnes and Conklin [1984]

Table 9.3 Comparison of Reflectance Results for a Two-Layer Model above Specularly Reflecting Surface with Exact Calculations from Ozişik and Shouman [1980] (ρ_{sp} = specular reflectance at bottom)

$\tilde{\omega}_1$	$\tilde{\omega}_2$	ρ_{sp}	4-stream	8-stream	16-stream	exact
	0.2		0.0467	0.0461	0.0461	0.0461
0.2	0.5	0.0	0.0513	0.0506	0.0506	0.0506
	0.8		0.0590	0.0582	0.0582	0.0582
	0.95		0.0653	0.0644	0.0644	0.0644
	0.2		0.0502	0.0498	0.0498	0.0498
0.2	0.5	0.5	0.0562	0.0557	0.0557	0.0557
	0.8		0.0674	0.0666	0.0666	0.0666
	0.95		0.0781	0.0769	0.0769	0.0769
	0.2		0.0531	0.0529	0.0529	0.0529
0.2	0.5	0.9	0.0605	0.0601	0.0601	0.0601
	0.8		0.0762	0.0752	0.0752	0.0752
	0.95		0.0937	0.0920	0.0921	0.0921

Table 9 4 Comparison of Transmittance Results for a Two-Layer Atmosphere above Specularly Reflecting Surface with Exact Calculations from Ozişik and Shouman [1980] (ρ_{sp} = specular reflectance at bottom)

$\tilde{\omega}_1$	$\tilde{\omega}_2$	ρ_{sp}	4-stream	8-stream	16-stream	exact
	0.2		0 0750	0 0728	0 0727	0 0727
0.2	0 5	0 0	0.0899	0 0877	0 0876	0 0876
	0.8		0 1171	0 1146	0.1146	0 1146
	0.95		0.1408	0 1380	0 1380	0 1380
	0.2		0 0383	0 0371	0 0371	0 0371
0 2	0.5	0 5	0 0480	0.0467	0 0467	0 0467
	0 8		0 0678	0 0663	0 0663	0 0663
	0.95		0 0879	0 0858	0 0858	0 0858
	0.2		0 0078	0 0076	0 0076	0 0076
0 2	0.5	0 9	0 1016	0 0099	0 0099	0 0099
	0.8		0 1561	0 1521	0.1522	0 1522
	0.95		0 2209	0 2150	0 2151	0 2151

Table 9 5 Comparison of Upward Radiance at Top of U S Standard Atmosphere at Night with Same Calculations from LOWTRAN6 Wavelength 3-4μm, T_G = 300 K, Surface Albedo = 0 05

model	$L^{\uparrow}(11\ 4\ ^{\circ})$	$L^{\uparrow}(26\ 1\ ^{\circ})$	$L^{\uparrow}(40\ 3\ ^{\circ})$	$L^{\uparrow}(53\ 7\ ^{\circ})$	$L^{\uparrow}(65\ 9\ ^{\circ})$
ours	0 3499	0 3478	0 3434	0 3355	0 3214
ours, no scattering	0.3415	0 3387	0 3331	0 3232	0 3055
LOWTRAN6	0 3411	-	-	-	-

Table 9 6 Parameters Describing Atmospheric Effect on Radiances of Landsat Thematic Mapper bands, for U.S Standard Atmosphere with 53 7 ° Incident Solar Angle

TM band	wavelengths (μm)	L_0 $Wm^{-2}\mu m^{-1}sr^{-1}$	α (β_d/β_s)	β_s (L_d/L_t)	β_d (L_s/L_t)
TM1	0 45-0 52	34 483	0 31744	0 66129	0 20992
TM2	0 53-0 61	16 989	0 23198	0 72016	0 16706
TM3	0 62-0 69	9 5651	0 17438	0 78447	0 13680
TM4	0 78-0 90	3 4237	0 11675	0 84371	0 098501
TM5	1 57-1 78	0 11340	0 031436	0 91439	0 028745
TM7	2 10-2 35	0 025956	0 023439	0 93095	0 021820

9.5. Figures

Figure 9.1. Three components of sensor-measured radiance. L_0 contains both pure atmospheric scattering radiation and atmospheric thermal emission. L_s carries target information. L_d is mainly composed of the contribution made by the surrounding pixels.

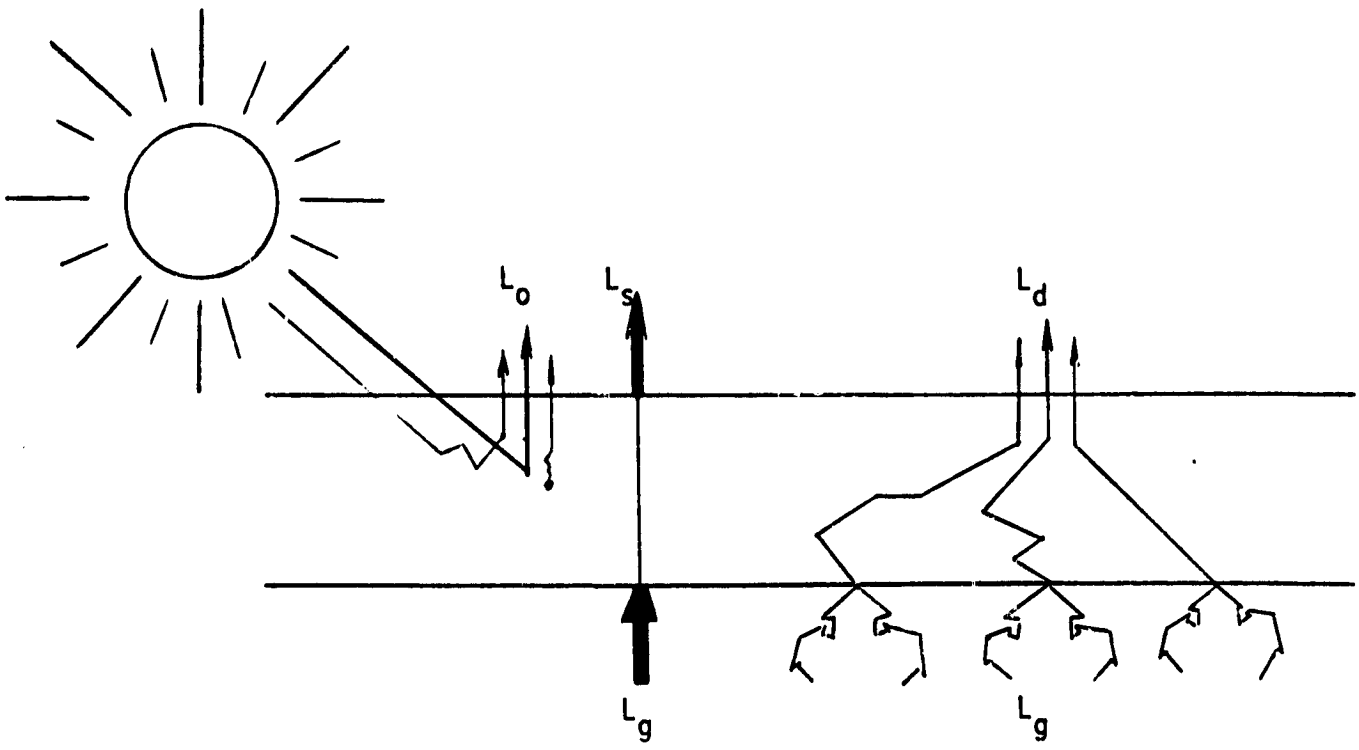

Figure 9.2. Relation between T's and L's. (a) Definition of $T_d(0,\vec{r},\vec{\Omega};\tau,\vec{r}\,',\vec{\Omega}\,')$. (b) Definition of $T_d(\tau,\vec{r}\,',\vec{\Omega}\,';0,\vec{r},\vec{\Omega})$. (c) By integrating $T(0,\vec{r},\vec{\Omega};\tau,\vec{r}\,',\vec{\Omega}\,')$ over entire hemisphere and entire ground plane, $T(0,\vec{\Omega};\tau)$ is obtained. (d) Definition of $T(\tau;\vec{\Omega})$. (a) and (b) are a reciprocal pair, and (c) and (d) are another reciprocal pair.

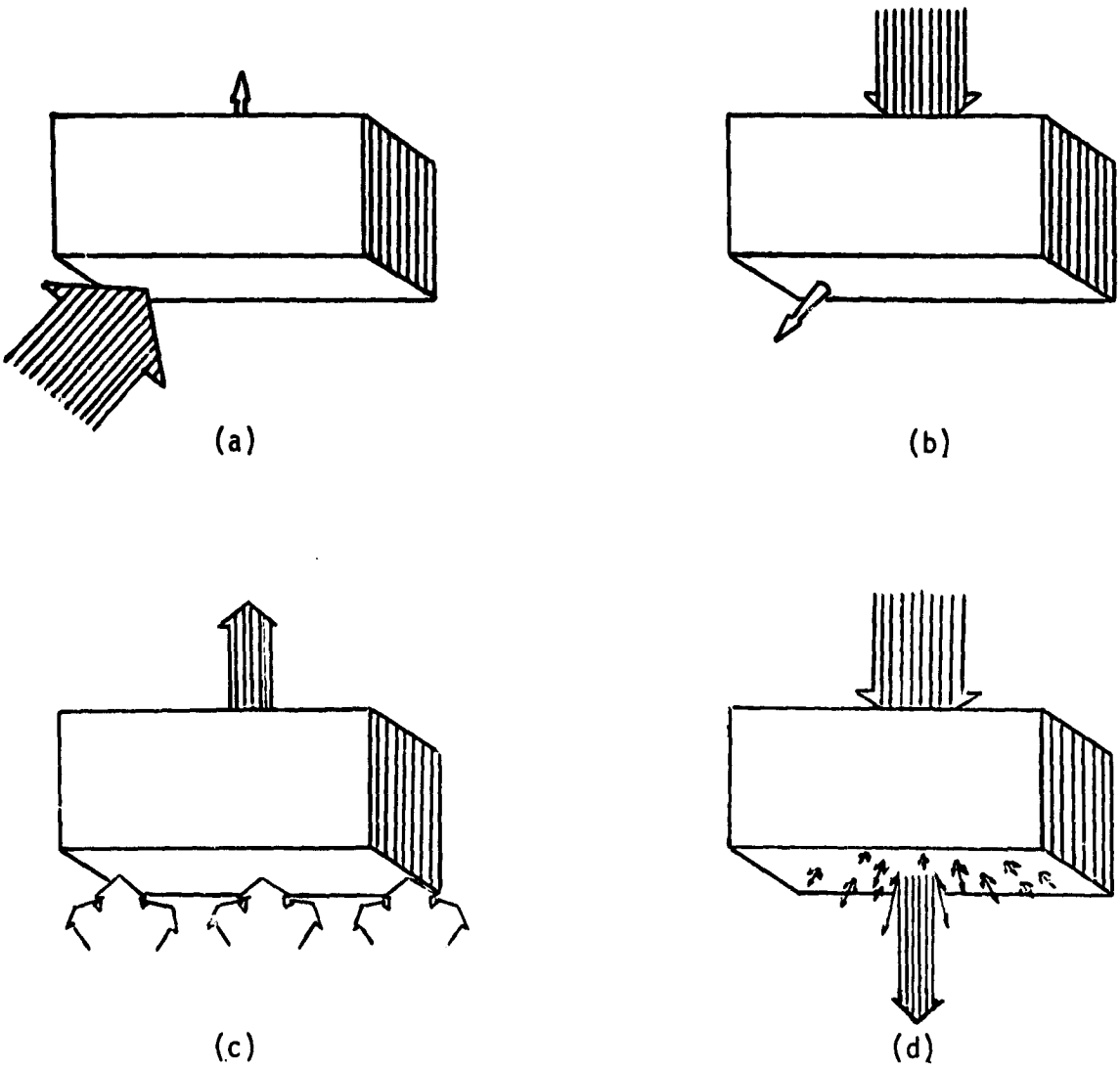

Figure 9.3. An assumed anisotropic reflectance pattern in which the anisotropic reflectance factor depends on reflection zenith and azimuth only, and is independent of location. The gravel-shaped feature at each point represents a forward-peaked anisotropic refelctance pattern. The size of the feature indicates the magnitude of the surface albedo at that point. The similarity among the features shows the location independence of the anisotropic reflectance pattern.

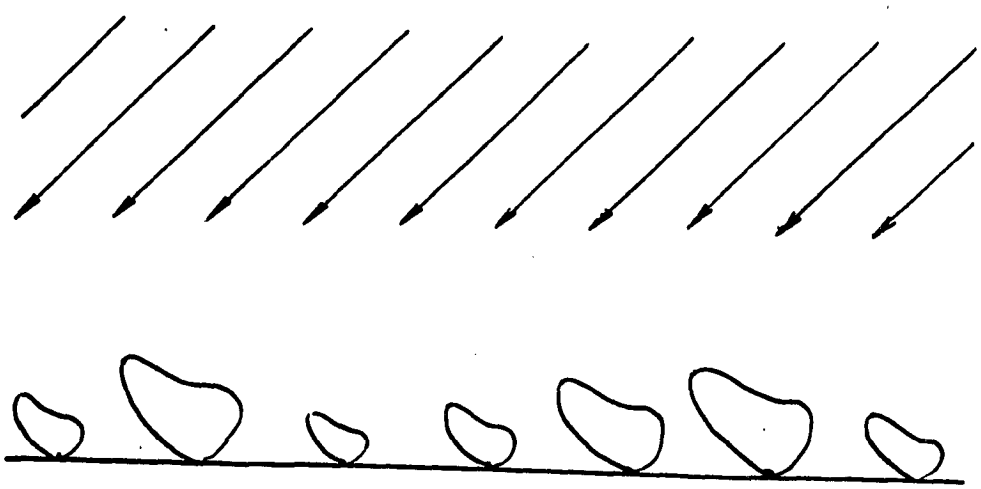

Figure 9.4. Cross section of point spread function for Thematic Mapper (TM1–TM4, TM5 and TM7). The pixel size is 28m by 28m. The horizontal axis is the number of pixels from the central pixel. The vertical axis is logarithmically transformed. (a-d) Visible and near-infrared bands (TM1–TM4). (e-f) "Shortwave infrared" bands (TM5 and TM7).

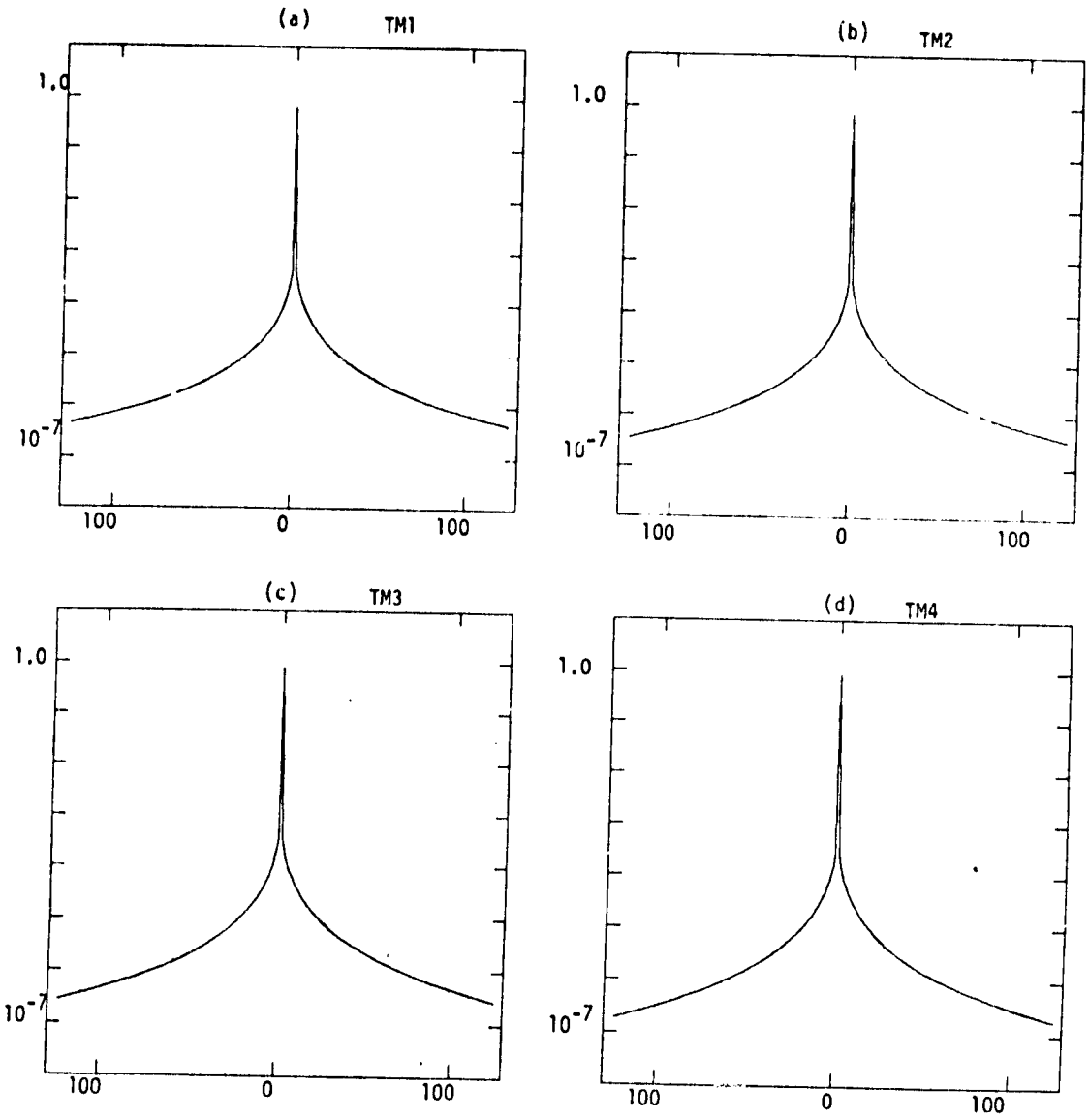

Figure 9.4. (continued)

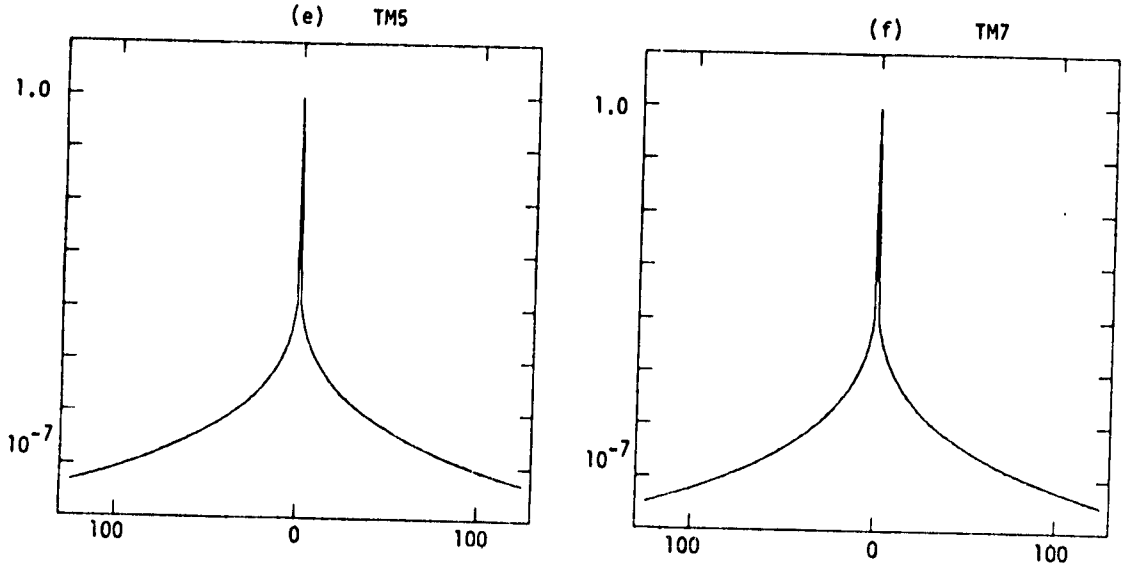

Figure 9.5. Images before and after restoration by deconvolution using point spread function. In the right column are the restored images and in the left column are the original ones. The upper row is for the TM1 images, whereas the lower row is for TM2 images. The point spread functions are produced for the U.S. Standard Atmosphere.

ORIGINAL PAGE IS
OF POOR QUALITY

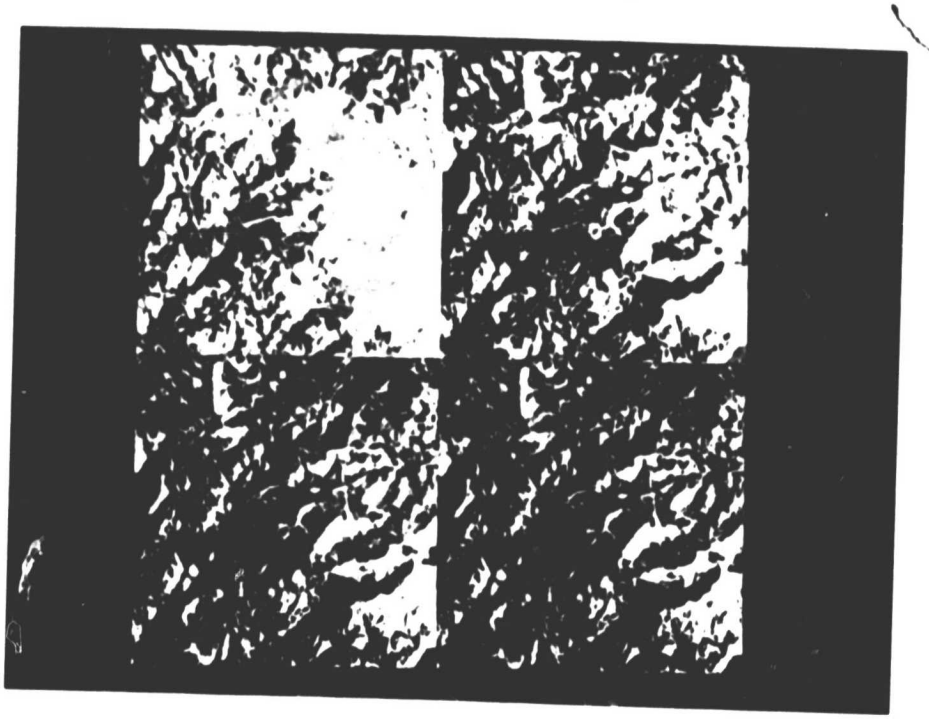

ORIGINAL PAGE IS
OF POOR QUALITY

Figure 9.6. Images restored using simpler algorithm *vs.* those by deconvolution procedure. Now the images produced by simpler algorithm using locally averaged radiance values appear in the right column.

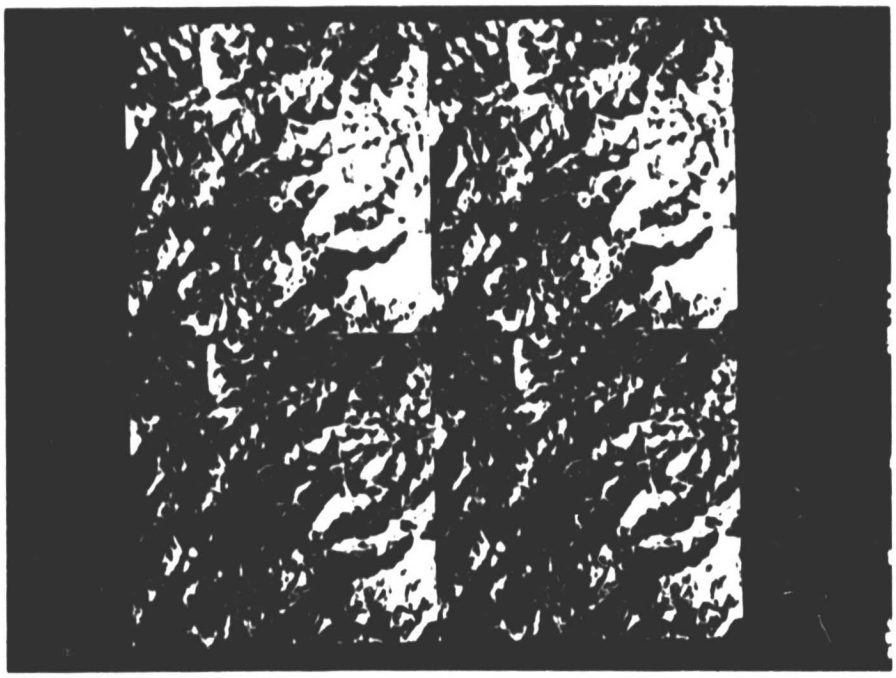

10. Texture Analysis of the Spatial Contiguity of Snow Cover

10.1. Introduction

Snow hydrologists have come to rely on satellite imagery for accurate estimates of snow cover over widespread and inaccessible areas. Prior to the advent of satellite data, snowmelt runoff models were based on point measurements, usually of snow water equivalent at index sites [Rango and Itten, 1976]. Subsequently, many studies have concluded that satellite measurements of snow-covered area (SCA) have a significant statistical relationship to seasonal streamflow [Rango et al., 1979; Rango and Martinec, 1979; Shafer and Leaf, 1979]. This relationship has been used for long-term volumetric flow forecasts [Thompson, 1975; Rango et al., 1977] and for determining the timing of daily runoff [Martinec, 1975].

The relationship between SCA and runoff depends on the time frame in which runoff is viewed. For daily predictions during the ablation period, SCA is directly related to runoff. The Martinec runoff model that has proven useful for many mountain basins [Rango and Martinec, 1981] expresses the relationship

$$Q_t = c\,(E \times SCA \times (1-k) + kQ_{t-1}) \tag{10.1}$$

Here Q_t is runoff at time t, c is a runoff coefficient, E is energy, usually in degree-days, SCA is snow-covered area, and k is the recession coefficient.

In the longer term, it is known that the rate of snowline retreat is inversely related to snow water equivalent and to runoff [Rango and Itten, 1976]. Furthermore, the relationship between SCA and depth is quite variable: snow covering the same areal extent can vary 200 percent in depth [Martinec, 1980]. In fact, Martinec found that SCA is better related to the ratio of the current water equivalent to maximum seasonal water equivalent. This agrees with Thompson's [1975] earlier finding that SCA is more strongly related to the percent of total seasonal runoff than to runoff itself. Thus the behavior of the SCA parameter in runoff models beyond those for short-term forecasts becomes complex; it is best represented in a form differentiated with respect to total accumulation [Martinec, 1980]. Alternatively, for long-term forecasting, the more direct relationship between snow depth and total water volume may be preferable. From the analysis of a large random field sample, Adams and Roulet [1982] found a broad similarity in patterns of depth and water equivalent both in terms of quantity and distribution. They suggest that depth may be a good indicator of water equivalent and therefore of runoff.

Snow depth cannot be directly determined from a single satellite image but the pattern of snow distribution at various overall depths is readily apparent. In fact, expert snow observers have used the appearance of surface features to estimate depth during aerial overflights [Rango and Itten, 1976]. The notion that snow depth can be inferred from snow cover patterns implies that accumulation patterns are stable over time due to the control of underlying physical variables of terrain and exposure. During the accumulation period snow cover patterns are event related and result from irregular deposition influenced by elevation, wind and local topography. On the other hand, overall patterns that form during the snowmelt period are quite predictable since melt rates are strongly controlled by altitude and exposure. Palmer [1981] found over a three year period in the Rio Grande watershed of Colorado that snowline recession patterns were repeated; Lichtenegger and Seidel [1981] reviewed images of the Dischma valley in the Swiss Alps over an eight year period and concluded that a typical snow cover pattern forms each year during melt season. Moravec and Danielson [1979] and Martinec [1980] have also reported that yearly repeating contour patterns of snow-covered regions occur during the ablation period.

The analysis of snow cover patterns has generally been conducted as part of research into mesoscale (100–1000m) areal differentiation of snow cover such as those based on identifiable landscape units [Adams and Roulet, 1982] or hydrologic response units [Thomsen, 1980]. The purpose of these investigations is to develop regional generalizations about snow conditions from sites stratified by similar combinations of environmental variables. By inversion, it can be reasoned that the snow patterns themselves are meaningful expressions of the sum effect of the controlling variables. As Palmer [1981] points out, the position of the snowline acts as a natural integrator of the long-term effects of snow accumulation, slope, aspect, temperature, radiation, and wind. In a one-dimensional approach to the problem of quantifying snow patterns, Palmer developed regression relationships between percent snow cover and snowline elevation along a series of index baselines for the purpose of predicting SCA for an entire basin especially at times when it is partially obscured by clouds. This method requires that the network of baselines in a basin include all areas of significant snow cover but ignore detached patches of snow. It would seem more appropriate to use a two-dimensional characterization of the spatial contiguity of snow cover to predict snow-covered area.

Objectives

In this study it is proposed that two-dimensional descriptions of snow cover obtained by means of texture analysis, a set of statistical pattern recognition techniques, serve as predictor

variables in a linear relationship for predicting snow-covered area. This is undertaken as a preliminary step to assess the feasibility of predicting in the same manner another hydrologic parameter, snow depth, which may have a more direct and consistent relationship to the total volume of water stored in a melting snowpack. Operationally, the estimation of snow coverage itself on the basis of two-dimensional statistics may be useful along transition zones of the pack and during melt season when snow cover is highly dissected and difficult to inventory by manual or digital means. At this time, when short-term forecasting occurs the SCA variable is a direct, useful predictor of daily runoff. Snow depth data at the scale and extent necessary to conduct pattern analysis were not available for this study, however it may be possible in future studies to photogrammetrically determine snow depth at a scale appropriate to the analysis [Cooper, 1965; Rawls and Jackson, 1979].

As an initial stage in the investigation, the effect of sensor resolution on detectable "texture" is studied to determine whether the large improvement in spatial resolution provided by the Landsat Thematic Mapper (TM) sensor over existing Multispectral Scanners (MSS) translates into equally improved spatial information when analyzed using standard texture analysis methods.

Study Design

Digital images from the Landsat-4 satellite were available at 30 meter resolution (TM) and at 80 meter (MSS) resolution. Four matched sets of TM and MSS subimages (Figures 10.1 and 10.2) were selected and registered. For one set (image A), texture statistics were calculated over the entire image in order to closely investigate the behavior of the statistics at both resolutions. In the next step, two sets of texture features were calculated from windowed samples over each of the four image pairs. The relative distance between sample texture features was assessed by three different metrics. In the last stage, binary classifications of snow were made at both resolutions for image pair A. From these SCA was calculated by window and regressed against the two sets of sample texture features calculated above. Model efficiencies were calculated both internally using a jackknife regression technique and through time by cross-prediction between images of the same site having undergone significant snow recession.

10.2. Texture Analysis

Satellite images are two-dimensional projections of the three-dimensional landscape below. Frequently, such images are used to supply point data about scalar quantities like brightness, temperature and elevation or used in combination with other images to provide vector

information such as color [Ahuja and Schachter, 1981]. In doing so, the higher order relationships inherent in the image are effectively ignored. However, in one area of image processing, texture analysis, the study of spatial relationships is well developed. In general, the aim of texture analysis is to apply pattern recognition techniques to an image in order to segment and discriminate between scene regions or to aid in classification of cover types; the task is to quantify an invariant, non-labile characteristic of a scene object. Characterization of changing spatial patterns has not been well explored. The objectives of the present study are to use texture analysis in the traditional sense to quantify resolution-dependent differences in texture and to explore a new possibility of using extracted texture features as meaningful parameters in a functional relationship for the prediction of a physical variable.

Texture Analysis Methods

Texture analysis, the image processing term for pattern analysis, originates from empirical efforts to recognize and duplicate the elusive perceptual concept of texture. Visual analogies have held sway so long in this field that only recently have formal image models emerged on the level of abstraction found in other spatial disciplines [e.g. Pielou, 1977]. Within the sizable battery of empirically developed methods [reviewed by Haralick, 1979], no single approach has proven to be universal, in large part because the visual hierarchies involved in perceiving spatial structure work in a complex manner not easily duplicated by simple methods [Julesz, 1975]. As Haralick [1979] has noted, the organization of tonal primitives or local regions can be viewed as structural, probabilistic, or functional depending on relative resolution. Whether stochastic pixel-based models or deterministic region-based models are the most suitable texture descriptors depends on the coarseness, homogeneity and periodicity of the texture.

Statistical approaches range from simple first-order measures like grey tone differences and run lengths [Galloway, 1975] to more complex joint and conditional second-order co-occurrences [Haralick et al., 1973]. One-dimensional autoregressive models [McCormick and Jayaramamurthy, 1974; de Souza, 1982] are only partially successful at describing spatial patterns while two-dimensional autoregression [Tou, 1980] becomes a complex task.

Image patterns can be analyzed in terms of spatial frequency but Fourier analysis has had limited application to texture analysis. The Fourier transform must be computed over large windows and comparison of power spectra between different sized regions is difficult [Chen, 1979]. More importantly, local information is scattered in the frequency domain so that similar peaks may be caused by a nearly periodic texture or a single strong edge [Nevatia, 1983]. Recently

Chen [1982] and Jernigan and D'Astous [1984] have successfully developed local and size invariant texture features based on the Fourier transform that overcome some limitations of the method. findings from perceptual experiments [Pratt et al., 1978; Julesz and Caelli, 1979] have cast doubt on the efficacy of Fourier analysis for texture discrimination. Patterns having identical power spectra and thus identical autocorrelation functions, can be discriminated effortlessly by eye.

Translated into the spatial domain, Fourier analysis is simulated by a series of convolutions [Faugeras, 1978; Laws, 1980]. Convolution masks which enhance high frequency information act as edge detectors that approximate mathematical gradient operators [Ballard and Brown, 1982]. Once obtained, the edge structure of an image can be reported simply in spatial averages or used to form high level primal sketches [Marr, 1982]. Related to edge analysis are methods that quantify local maxima and minima by row [Mitchell et al., 1977] or which construct more complex relational trees of one-dimensional intensity profiles expressed as nested or concatenated peaks [Ehrich and Foith, 1978].

When the elements of a texture become much larger than the resolution cell of an image, pixel-based stochastic models break down and are supplanted by structural methods which identify primitives, measure their attributes and determine their spatial relationships [Wang et al., 1981; Matsuyama et al., 1982; Tomita et al., 1982]. In highly regular patterns, primitives can be described syntactically using tree grammars [Lu and Fu, 1979].

There have been few studies undertaken to rigorously compare texture analysis methods. Frequently cited works by Weszka et al. [1976] and Conners and Harlow [1980] have led to the widespread use of Haralick's second-order statistical features: the moments of the grey-level co-occurrence matrix (GLCM). Indeed, co-occurrence statistics have been very useful for image segmentation [Chen and Pavlidis, 1979; Conners et al., 1984] and for image classification [Hallada et al., 1982; Vickers and Modestino, 1982; Holmes et al., 1984]. Julesz's [1975] finding that human texture discrimination operates finding that human texture discrimination operates at the level of second order relationships has lent such support for the GLCM approach that less costly first order methods reported to perform equally well for classification purposes [Weszka et al., 1976; Mitchell and Carlton, 1978; Pietikäinen et al., 1983] are not implemented as often. Because the GLCM serves as the standard of comparison for testing the performance of texture analysis methods, it was chosen for use in this study along with a newly reported local method: Laws' [1980] texture energy measures.

Grey-level Co-occurrence Matrix

The grey level co-occurrence matrix (GLCM) is an array of joint frequencies whose dimension is equal to the number of grey levels in the image. Each entry in the matrix is the frequency with which brightness i co-occurs with brightness j when separated by distance d in the direction θ. Frequencies, often normalized to probabilities, are reported in both directions for a joint pixel pair making the matrix symmetric. As a first step towards data reduction, the number of grey levels is decreased to 64 or less, and the four directional matrices can be averaged into one. To compress the data further, several statistics are calculated that express either the distribution of matrix values around the main diagonal or the degree of correlation between matrix rows and columns. Seven statistics proposed by Haralick et al. [1973] are given in the Appendix; these include energy, correlation, homogeneity, entropy, inertia and information correlations 1 and 2. Energy and homogeneity are measures that emphasize low contrast transitions; entropy and inertia increase with texture coarseness. Correlation statistics measure the degree of association between marginal and total values expressed either as frequencies or entropies.

An elegant solution to the problem of choosing an optimal combination of distance and orientation to best describe the structure in a texture was proposed by Zucker and Terzopoulos [1980]. They developed a chi-square statistic based on maximum likelihood estimates of the marginal matrix probabilities to test the independence of rows and columns. The unnormalized co-occurrence matrix is thus viewed as a contingency table in which intensity pairs are samples obtained from a two-dimensional random process. Notationally:

$$\chi^2 = N \left(\left(\sum_{i=1}^{m} \sum_{j=1}^{n} \frac{x_{ij}^{\,2}}{r_i\, c_j} \right) - 1 \right) \tag{10.2}$$

N is the total number of samples. Degrees of freedom $\nu = (m-1)(n-1)$, x_{ij} is the co-occurrence matrix entry, $r_i = \sum_{j=1}^{n} x_{ij}$, and $c_j = \sum_{i=1}^{m} x_{ij}$.

In the present study of snow texture, an automated system was developed to calculate the following for each subsample of an image: four unnormalized directional matrices, the chi-square value for each, the normalized matrix for the maximum chi-square angle, and the seven co-occurrence statistics. Only the final statistics from the most structured matrix were concatenated into an output file. This process was repeated for each of four distances (1,3,5,10 pixels) and four quantizations (8,16,32,64 grey-levels) for image pair A.

Texture Energy Measures

Despite the shortcomings of Fourier analysis outlined above, texture analysis methods that characterize spatial frequency are very useful if implemented locally in the spatial domain. This is accomplished by a sequence of boxfilter applications which are faster and simpler than a single convolution using the fast Fourier transform [McDonnell, 1981]. In his dissertation, Laws [1980] derived a series of one-dimensional operations of center-weighted local averaging, symmetric first differencing (edge detection) and second differencing (spot detection) [Pietikäinen et al., 1983]. When convolved together these vectors form nine 3 x 3 masks (see Appendix) some of which are recognizable as standard gradient operators like the pair of vertical and horizontal Sobel operators (fil_1, fil_3), and the Laplacian second difference operator (fil_8). Note that all but fil_0, the low pass smoothing filter, are zero-sum filters.

Texture features are obtained from each of the nine separately convolved images by calculating local statistics such as the sum, the mean or the standard deviation over small windows. McDonnell [1981] along with Laws have found that the variance or standard deviation of filtered windows are very powerful measures of image texture. In a zero mean field produced by convolution with a zero-sum mask, variance is the average of the squared values which makes it a measure of total energy within a window. Laws claims that the average absolute value is a fast approximation to the standard deviation; he refers to both the average and the standard deviation as measures of texture energy. Pietikäinen et al. [1983] tested two other texture energy features, the sum of the absolute values and the maximum value within a window, and found that the local maxima performed just as well as the sum. In this present study three features were compared: the sum, average and the standard deviation of values within windows sized 16 x 16 on the MSS image and 32 x 32 on the TM image. Following Laws' convention, these features are referred to as SUM, AVG and SD. As was done for GLCM analysis, an automated system was developed to cycle through all nine filters, convolve the image, compute the local statistics by window and concatenate them into an output matrix. Window size was based on Laws' finding that classification accuracies were nearly perfect using 32 x 32 window but dropped rapidly below 15 x 15. According to Hallada et al. [1982], this sample size is also adequate for co-occurrence analysis. They found that class separability increased logarithmically and then leveled off as window size increased from 3 x 3 to 13 x 13.

Texture energy measures are distinguished from Fourier methods by their local nature. Phase relationships within each window are measured without reference to a global origin [Laws,

1980], whereas Fourier frequency components contain global information from across an entire image at the neglect of local information [Jernigan and D'Astous, 1984]. In addition, gradient filters can be tailored to various textures by increasing the differencing distance to overcome noise but keeping it small enough so that local gradient remains a good representation of local changes [Ballard and Brown, 1982].

Parallel work by Faugeras and Pratt [1980] lends support to the Laws energy approach. Because the autocorrelation function has proven insufficient for texture discrimination (see above) these authors sought ways of characterizing the decorrelated texture field which would yield useful texture measures. Decorrelation can be accomplished by a whitening operator based on adjacent row and column correlations; if correlations are perfect this operator becomes the Laplacian operator. Alternatively, gradient operators like the Sobel filter can replace the whitening operator. Note that these are three of the nine Laws convolution masks.

Using a distance metric criterion, Faugeras and Pratt [1980] found that the first four moments of the first-order histogram of the decorrelated field provided good separability between similar natural textures. The first two histogram moments of the decorrelated images are exactly equivalent to the average and standard deviation of texture energy planes convolved with the same gradient operator. In accord with perceptual findings, inclusion of shape measurements taken from the autocorrelation function improved separability but alone were weak discriminators. The Sobel operator, a directional filter that does not zero out the mean or create unit variance, gave the best separability while the non-directional Laplacian was the worst. This implies that Law's choice of average and standard deviation features is well founded since all but the smoothing and Laplacian filters are non-symmetrical.

Pietikäinen et al. [1983] have confirmed that local statistics of convolved images yield better classification results than co-occurrence statistics. In the following analysis of snow cover patterns the two methods are compared for relative powers of separability and utility in characterizing spatial distribution for the purpose of predicting area.

10.3. Data Processing

Registration and Sampling

The imagery used in this study was taken by Landsat-4 Thematic Mapper (TM) and Multispectral Scanner (MSS) sensors. TM imagery was available for two dates, December 10, 1982 and January 18, 1983, in which images overlapped along adjacent paths; identical MSS imagery

was available only for the December date. The images are centered on the Kern and Kings river basins in the southern Sierra Nevada which are adjacent watersheds on the order of 4,500 square kilometers (see Rango et al. [1979] for a complete geographic description). Four subimages of varying textural complexity sized 256 pixels in dimension were selected from the December TM image. Corresponding MSS subimages, 128 pixels in size, were located and registered to the TM sites. Registration was a simple matter of enlarging the MSS subimage two-fold and translating the image to line up with the TM subimage. Resampling was unnecessary because geometric rectification performed by the NASA Goddard LAS system left MSS resolution almost exactly half the TM resolution. This level of registration accuracy was adequate for comparison of textural differences between resolutions. For the second stage of regression analysis a single site in the Kern basin was selected from both December and January TM images that showed evidence of substantial snow recession between scenes. These subimages were also co-registered using simple translation without initial resampling.

The texture study sites are about 65km^2, comparable in size to several small experimental watersheds [e.g. Rango and Martinec, 1979]. For an initial comparison of the behavior of texture features at the two resolutions, co-occurrence matrices were calculated over the entire scene. For the purpose of separability measurements and regression analysis image pairs were subsampled using 32$\times$32 sized windows for the TM image and 16$\times$16 sized windows for the MSS image. This non-overlapping sampling strategy yielded 64 samples per subimage each covering about one square kilometer. At this scale, the analysis remains within the realm of mesoscale studies and is equivalent in scale to NOAA AVHRR imagery at nadir.

Background Effects

Much of the experimental work done in texture analysis has been carried out on homogeneous texture fields which are assumed to be consistently specified by either parametric or deterministic models derived solely from the relationships of the texture primitives. Texture analysis of natural terrain must take into account external variables such as topography and vegetation that act as forcing functions on the pattern of surface cover. Shadows, topography and plant cover become part of a scene specific textural characterization of the overlying snow cover.

Topographic effect and shadowing can be reduced if digital elevation data are available, making it possible to map radiance values into a a synthetic brightness image using lambertian or non-lambertian models of surface reflectance [Justice et al., 1981]. Digital elevation data are available for the southern Sierra Nevada only at 90 meter resolution and according to Seidel et al.

[1983] elevation data on a scale greater than the Landsat sampling distance are inadequate for producing a satisfactory synthetic brightness image. Band ratioing, a method for canceling out multiplicative effects of topography was rejected because of its tendency to enhance differential noise between bands giving rise to spurious or confounding signals of high frequency texture. Without the possibility of digital terrain correction, images were selected in which shadowed areas were a small proportion of the image. This unfortunately limited the method of analysis to larger, open areas of mountain basins which may not be truly representative sites. Since all comparisons in this study were scene specific, it was assumed that the texture signal caused by underlying factors would hold constant between resolutions and between dates. More importantly, the chosen texture analysis methods, co-occurrence and energy statistics, are sensitive measures of contrast and of edge structure and should thus reflect the distribution of very bright, high-contrast snow patches rather than dark, low contrast background features. To emphasize contrast and edge detail all texture features were derived from visible bands TM 2 and MSS 4 in which snow is very bright.

Pre-Processing

Texture measures, like co-occurrence statistics that are based on grey-level transitions, are sensitive to shifts in overall scene brightness or contrast. To standardize images so that monotonic changes in illumination are not used to discriminate textures, the first order grey-level distributions of all the textures were normalized to uniform distributions. At the same time, images used for GLCM analysis were reduced in quantization to make the co-occurrence matrices reasonably sized. Histogram equalization was carried out using a procedure outlined by Pratt [1978]. This process can be considered a monotonic point transformation in which the input cumulative probabilities are equal to the output cumulative probabilities for a given input index. The histogram equalization function is expressed:

$$g = [g_{max} - g_{min}]\, P_f\,(f\,) + g_{min} \tag{10.3}$$

Here g is the output grey value, g_{min} is the minimum output grey value, g_{max} is the maximum output grey value, and $P_f\,(f\,)$ the cumulative distribution function of the input variable f .

Note that the output number of grey levels is controlled by the $g_{max} - g_{min}$ range, so that images are simultaneously equalized and reduced in quantization by a single transformation.

10.4. Snow Classification

Spectral Characteristics

Snow has a very distinct spectral signature. It is extremely bright in the visible bands, frequently saturating sensors calibrated for vegetation reflectances and at the same time is quite dark in the shortwave infrared bands like TM bands 5 and 7 [Dozier, 1984]. Few scene elements are confused with snow cover except for white clouds that often are indistinguishable in the visible and near infrared spectral range. With the advent of TM shortwave IR data (1.57–1.78μm and 2.10–2.35μm) discrimination between the two classes has become possible because clouds are significantly brighter than underlying snow in these bands [Dozier, 1984]. This suggests that given visible and shortwave IR data, satisfactory snow classification could be achieved with only two spectral bands.

A successful two band snow classification using MSS visible and near infrared data is already in use; Haefner [1979] found that snow cover could be classified into three found that snow cover could be classified into three categories, snow-free, transitional and snow-covered, using only MSS bands 5 and 7. Although it was necessary to further subdivide classes during training site selection, the visible and near infrared bands were sufficient for discriminating the three snow categories except in the presence of concrete, white rocks or snow under dense coniferous forest. (Mixed classes of snow under forest canopy can be discriminated with the addition of MSS band 4). For complex classifications which distinguish various stages of snow metamorphism all four MSS bands have been used to identify up to ten classes of snow and seven classes of ice [Thomas et al., 1979].

Classification Approach

Considering the superior resolution and spectral discrimination of the TM sensor, it was presumed that a two band approach using TM bands 2 and 5 would be an improvement over MSS two band methods and sufficient for a binary classification of snow-covered and snow-free areas. In the visible range TM band 2 was selected because of its larger dynamic range and therefore lower tendency to saturate over snow compared to TM band 1 and yet remain relatively insensitive to metamorphic changes in grain size compared to TM bands 3 and 4 [Dozier, 1984]. TM band 5 had several reasons to recommend its use; besides cloud discrimination properties, this band is generally a high information channel. Price [1984] found that the TM band 5 information rate expressed in bits/pixel is higher than shorter wavelengths and is also relatively uncorrelated with visible and near infrared bands.

~~PRECEDING PAGE BLANK NOT FILMED~~

Because snow is spectrally distinct, very bright and relatively homogeneous it is amenable to thresholding approaches to classification. In fact, Rango and Itten [1976] found that snow classification results differed little between histogram parallelepiped and maximum likelihood classifiers. For this study, rather than use a parallelepiped scheme, methods were investigated to find a single data plane for thresholding which combined critical spectral properties of visible and shortwave infrared wavelengths and also reduced variance.

Table 10.1 gives summary statistics for a single snow cover training site from TM image A (n=315) using two approaches, ratioing and principal component analysis. Ratioing the two adjacent bands, TM 2 and TM 3, reduced variability and range when compared to TM band 2 alone. Presumably, variation due to topography was reduced by canceling out multiplicative effects. This reduction is greatest for adjacent bands in which surface reflectance ranges are similar [Holben and Justice, 1981]. Although the narrower threshold of the ratioed class was an improvement, it did not include important shortwave IR spectral information. A ratio of TM bands 2 and 5 reduced the threshold range but not the variability with respect to the single visible band.

On the other hand, snow patches were clearly discernible on principal component images. As Figure 10.3 shows there is virtually no difference between the first principal component using TM bands 2,3,4,5 and 7 and the first component using bands 2 and 5 alone (see discussion below). The two band component was selected for thresholding since it was computationally less costly and because it had a lower coefficient of variation than either TM band 2, the TM2/TM5 ratio or the five band principal component image. A single threshold range applied to the two band principal component image yielded a satisfactory classified image (Figures 10.4 and 10.5).

Classification Results

The spectral and spatial advantages afforded by the TM sensor are evident from comparing TM and MSS snow classifications for the same scene (Figure 10.4). The MSS scene was also classified by thresholding a single data plane, the first principal component of bands 4,5,6 and 7, which was selected by the same process of comparing training site statistics. Percent snow cover in the MSS subimage was 30% higher than in the matched TM subimage. This discrepancy partly stems from the poorer spectral discrimination provided by the MSS data and the inexact, subjective nature of thresholding, but its major cause is the far coarser resolution that blurs transition zones and leads to systematic overclassification. At the same time, isolated, small groups of snow-covered pixels identified on the TM image were omitted from the MSS classification.

Principal Component Analysis

Principal component analysis is a linear orthogonalizing transformation that yields a vector of coefficients, the eigenvector, used in linear combination with the variables of the input vector to align the variables along an axis of maximum variation that is statistically uncorrelated and geometrically orthogonal to succeeding components [Cooley and Lohnes, 1971]. A principal component image is obtained from the original image, g, having p spectral bands by the transformation [Moik, 1980]:

$$g^c = \mathbf{T}\,(g - \mathbf{m}) \tag{10.4}$$

Here g^c is the principal component image, $\mathbf{T} = pxp$ is the matrix whose rows are the normalized eigenvectors of the spectral covariance matrix $\mathbf{C}$ of g, and $\mathbf{m}$ is the mean vector of the p spectral bands.

The eigenvalues λ_p and the eigenvectors t_p of $\mathbf{C}$ are obtained by solving the equation

$$\mathbf{C}\, t_p = \lambda_p\, t_p \tag{10.5}$$

The principal component transformation isolates non-random information from noise while also decorrelating the transformation axes to eliminate redundancy [Anuta et al., 1984]. The resulting scalar eigenvalues and set of eigenvectors can be interpreted directly for some insight into the sources of variation. The ratio of each eigenvalue to the sum of all eigenvalues gives the percent of total variance explained by the corresponding eigenvector. The eigenvectors are comprised of coefficients or loadings that correspond to the cosine of the angular distance through which each input band must be rotated to be aligned with the principal axis of variation. The larger coefficients represent smaller angular distances and thus greater influence on the component [Anuta et al., 1984]. The loadings can be viewed as weights corresponding to the relative contribution made by each band.

Component loadings for TM and MSS subimages are given in Table 10.2. Clearly, the visible bands dominate the first principal component derived from five TM bands; visible and near IR bands all carry about equal weight while the shortwave IR bands contribute far less. Only in the second component does the near IR band behave independently of the visible bands. The loadings of the first principal component using only two bands reflects this same pattern and provides the same level of explained variance as the five band first component. Apparently redundancy among the five TM bands with respect to the first axis of maximum variation was effectively eliminated by using only two bands.

Loadings for the first component derived from four MSS bands are not clearly divided into two classes. Visible bands show a pattern of increasing relative contribution into the IR which then tapers off again; MSS bands 4 and 7 alone were unable to represent this combination of spectral information. In reviewing the component images, it is apparent that TM snow classification was achieved using essentially a reduced-variance visible image augmented slightly by shortwave IR information whereas MSS classification relied on a nearly equal mix of visible and near IR bands.

10.5. Methods

Distance Measures

In the language of statistical pattern recognition, the texture statistics used in this study are features which detect sufficient statistical (non-random) variability between patterns to allow classification. The task in feature selection is to find an evaluation function that will assess how well a set of features discriminates between classes. Generally, there are three types of evaluation rules [Ben-Bassat, 1980]: information measures (uncertainty), distance measures (separability), and dependence measures (association). Each of these measures distribute objects into feature space which can be divided into classes by a discriminant function. Alternatively, each measure can stand as a figure of merit such that a large measurement difference implies low classification error. Evaluation by figure of merit rather than by classification has the advantage of being independent of any particular discriminant function and may additionally include error analysis [Faugeras and Pratt, 1980]. Distance metrics were deemed most appropriate to the aim of quantifying resolution-dependent textural differences rather than for discriminating between them.

Distance measures used in pattern recognition for statistical evaluation of separability operate on sample pools. Accordingly, the large TM and MSS images were divided into 64 square samples covering comparable areas. Distances were calculated between these samples and then reported in sum or average.

Three distance measures were chosen to evaluate the separability of TM and MSS texture features. Initially Euclidean distance was calculated between sets of statistics that were first rescaled between zero and one in order to preserve a consistent metric for variables originally measured on different scales. The Euclidean distance between columns of the TM and MSS feature matrices was calculated as follows:

$$d(j,k) = \sum_{i=1}^{N} \sqrt{[x(i,j) - x(i,k)]^2} \tag{10.6}$$

The Euclidean distance between image pairs was the sum total of distances between all texture features (matrix columns). Because it was necessary to re-scale the data, this metric accommodated comparisons between unnormalized variables such as sums and counts.

To be able to easily compare the degree of similarity among data sets, the average Gower Similarity Coefficient [Gower, 1971] was calculated between each feature k:

$$S(i,j,k) = \frac{1}{m} \sum_{i,j}^{m} 1 - \frac{|x(i,k) - x(j,k)|}{R(k)} \tag{10.7}$$

$R(k)$ is the range of a given texture feature k over both sets of data. The similarity between image pairs was the overall average similarity between texture features. Like Euclidean distance, the similarity coefficient is sensitive to magnitude. When applied to inherently normalized features such as the standard deviation or the average, the range is sufficiently comparable between data sets for the coefficient to work well. Unscaled data sets ranging widely in value will have low similarity though correlation between the two may be high.

The last distance metric considered, Bhattacharyya distance ,is a more sophisticated measure theoretically based on a scalar function of the probability densities of the two feature sets [Faugeras and Pratt, 1980]: For Gaussian densities Bhattacharyya distance is calculated [Davis, 1981]:

$$B(S_1,S_2) = \frac{1}{8}(\bar{u}_1 - \bar{u}_2)\left[\frac{\Sigma_1 - \Sigma_2}{2}\right]^{-1}(\bar{u}_1 - \bar{u}_2)^T$$

$$+ \ln 6 \left\{ \frac{\left| \frac{1}{2}(\Sigma_1 + \Sigma_2) \right|}{|\Sigma_1|^{1/2} \, |\Sigma_2|^{1/2}} \right\} \tag{10.8}$$

Here u_i is the mean vector for class i, Σ_i is the covariance matrix for class i, and $|\Sigma_i|$ is the determinant of Σ_i.

By taking variability into account, this metric distinguishes between feature sets that might have identical means but a different spread of values around the mean. In addition, Bhattacharyya distance is theoretically linked to the Chernoff error bound applied to Bayesian classification error [Faugeras and Pratt, 1980]. If texture features are normally distributed these error bounds can be applied to Bhattacharyya measurements. As is true of the other metrics, Bhattacharyya distance is most successfully used on normalized variables.

Regression Techniques

As a first step in regression analysis, all variables were screened for asymmetrical distributions. If histograms and quantile plots of the sorted data against quantiles of the standard normal distribution (Q-Q plots) were skewed, the variables were transformed using power functions [Tukey, 1977] that gave the best approximation to symmetric and, if possible, normal distributions. This was done to better satisfy least-squares assumptions of normality and homoscedastic error.

For each of the twelve models, the best subset of predictor variables was selected using a leaps and bounds regression method available from the S interactive data analysis package [Becker, 1984] in which Mallow's C_p statistic served as the criterion for goodness of fit. This method is a generalization of stepwise regression methods that examines all possible subsets of predictor variables rather than the effect of a single addition to or deletion from the predictor set. The C_p statistic, closely related to the adjusted coefficient of determination, [Draper, 1981] is:

$$C_p = \frac{RSS_p}{s^2 - (n - 2p)} \tag{10.9}$$

RSS_p is the residual sum of squares from a model containing p parameters and s^2 is the residual mean square from the largest equation possible containing all the variables.

The term s^2 is taken as the unbiased estimate of the error variance σ^2. Since the expected value of the C_p variable is approximately p, the best, least biased equations are those in which the C_p statistic is equal to the number of parameters. In each case, the equation with the smallest number of parameters and least biased fit was chosen for the regression model.

Standard least-squares multiple regression was then run on the transformed variables using a set of programs from the S package. The significance of the regression coefficients was checked with a t-statistic and the overall regression significance with an F-statistic. The residual standard error and adjusted coefficient of determination (R^2) were calculated for comparison of models. Regression residuals were plotted against the fitted values, and a locally weighted smoothed line was drawn through the scatterplots to detect departures from the zero mean line. In addition, the sorted residuals were plotted against quartiles of the standard normal distribution to check for normality. Finally, a robust, iterated, weighted least-squares regression was run. Observations that received low weight were examined and the effect of deleting these samples was determined by repeating the least squares regression on the trimmed data set. If the least squares and robust regressions agreed well in coefficients and residuals, it was presumed that the least-

squares assumptions had been sufficiently met and that the tests of significance stood.

Without a large, longitudinal data set at a given site it is difficult to to test the predictive power of a model. In the case of the TM/MSS image pair, regression models were used for comparing the effect of resolution on the scene model, not for cross-predictive purposes. Instead, for each model, a jackknife technique was used to verify internal stability and to test internal predictability. In this technique, each observation was deleted in turn, the regression repeated and the new coefficients used to predict the deleted value. The stability of each regression coefficient was measured by the coefficient of variation and any observations with highly deviant coefficients were examined for error. The predicted and observed values were plotted in sample sequence and as scatterplots. Prediction residuals were also plotted to check for any systematic patterns. The overall prediction performance was measured using a model efficiency statistic [Rango and Martinec, 1979] which is a non-dimensional "goodness of fit" function:

$$R^2 = \frac{\frac{1}{n}\sum_{i=1}^{n}(y_i - \bar{y})^2 - \frac{1}{n}\sum_{i=1}^{n}(y_i - y_i')^2}{\frac{1}{n}\sum_{i=1}^{n}(y_i - \bar{y})^2} \tag{10.10}$$

Here y_i is the observed snow-covered area, y is the mean snow-covered area, and y_i' is the predicted snow-covered area. Similar to the coefficient of determination, this statistic is a measure of the proportion of variance explained by the model.

The purpose of independently deriving regression models for December and January images at a given site was to test the generality of each set of extracted parameters by means of a cross-prediction test. This technique determines how well one set of parameters predicts the snow cover at the same site but under an altered snow cover pattern. The data for the two dates were then pooled to obtain a general equation for the scene. As before, predictions and prediction residuals were plotted and model efficiencies calculated.

10.6. Results

Texture Characteristics

Gray level co-occurrence matrices (GLCM) are joint probability tables for a specified relationship between pixels. A comparison of matrices constrained by different joint relationships should reveal information about three fundamental texture properties: periodicity, directionality, and information content. Thus, a good starting point for analyzing the effect of resolution on

texture was to compare various co-occurrence matrices and the statistics extracted from them at both TM and MSS resolutions.

Using image pair A, co-occurrence matrices were tabulated over the entire TM and MSS scenes for a range of displacements (1, 3, 5, 10 pixels), a range of angles (0 °, 45 °, 90 °, 135 °) and a range of quantizations (8, 16, 32, 64 grey levels). The chi-square statistic was used as the criterion to choose the best combination of specifications. Plots of chi-square values for all quantizations and distances (Figure 10.6) show that the maximum chi-square angle (in this case vertical) was identical at all grey levels and displacements. Chi-square values from the two resolutions were consistently parallel in behavior; most information was found at a displacement of one pixel and, by definition, at the highest number of grey levels (64).

When TM and MSS images were divided into samples (for the purpose of metric analysis) it was possible to compare the χ^2 selected angles for each image by sample. Table 10.3 gives the correlations between selected angles for each image pair; only image D had a correlation better than 0.5. For all images, horizontal and vertical directions were dominant perhaps because the diagonal distance is actually 1.4 times longer than the distance to adjoining horizontal or vertical pixels. In the TM image the selected angle oscillated between the two orientations more rapidly than those of the comparable MSS image. This divergence in directionality is the most distinct textural difference between TM and MSS images. Although this may be interpreted simply as increased noise, it has elsewhere been reported that directionality is critical for distinguishing very similar cover types [Hallada, 1982]. This implies that the tendency of investigators to reduce computation by averaging the various directional co-occurrence matrices is probably an unwise economy in classification studies. However, averaged matrices are useful for deriving rotation-invariant measures of texture; statistics computed from averaged matrices are the most useful features for predicting SCA since they hold for various orientations of the terrain image.

Figure 10.7 is a graph of chi-square values for one angle plotted against distance. The exponential drop in chi-square beyond a distance of one corresponds to the sharp drop-off in the autocorrelation function observed in any natural texture [Laws, 1980]. Also note that large differences in information content due to greater quantization are only significant for distances less than five, beyond that, low quantization yields the same information. The large chi-square difference between MSS and TM images is due to the four-fold greater sample size used in the TM image to cover a comparable sample size at MSS resolution, not a reflection of a far greater information content. Regular artificial patterns will have additional peaks in the chi-square/distance

plot at displacements corresponding to the periodicity of the pattern. No such underlying periodicity was detected in these images using displacements that covered up to 60% of the linear dimension of the sample.

By definition the χ^2 statistic increases in magnitude as the information content climbs with increasing quantization. The computational costs of carrying out the analysis at 64 grey levels were too high to be considered in this study since each doubling of the grey scale increased all calculations four-fold. Sixteen grey levels were chosen as a compromise between information content and efficiency based in part from the analysis of co-occurrence statistics that follows.

GLCM Statistics

Plots of each co-occurrence statistic against angle for image pair A revealed that in each case the maximum chi-square angle was that which produced a matrix dominated by small grey-level transitions. This is a diagonally dominant matrix indicative of a relatively coarse texture (see Figures 10.8a,b). In short, the preferred textural orientation corresponded to the highest autocorrelation.

The inertia statistic was minimal at the χ^2 selected angle because it is designed to give most weight to infrequent, large, high contrast, transitions. And because the grey level differences act to weight the statistic, most differentiation between angles was achieved at the highest quantization level. MSS and TM responses were parallel but MSS values were consistently higher at each grey level, the expected behavior for a coarser texture.

Another statistic that varied inversely to the chi-square evaluation was entropy. This is the case because the negative log of small probability transitions is much greater than the negative log of high probability transitions. That entropy should be minimized where structure is greatest is intuitively correct. Entropy also dropped with decreasing quantization due to the increased probability per transition. Entropy values were greater for MSS than for TM at all grey levels, again indicating the relative coarseness of the MSS texture.

Dominance of low "contrast" transitions was best detected by the homogeneity statistic. Because the gradient between joint pixels appears in the denominator of the homogeneity formula, the largest homogeneities for both TM and MSS were found at the lowest quantization level at the χ^2 selected angle. Yet this statistic is relatively insensitive to quantization giving good differentiation between angles at the highest number of grey levels. As expected, the TM image had higher homogeneity than the coarser MSS image.

Highly correlated with homogeneity, the energy statistic was also maximized at lowest quantization for the χ^2 angle. Energy is simply the square of the transition probabilities; as the probability per bin drops with increasing quantization, the square gets increasingly smaller. Thus, energy is very sensitive to an increase in quantization such that no detectable difference exists between angles at 64 grey levels. At this quantization the statistics would have to be scaled to remain compatible with other GLCM statistics. Energy was higher for the TM scene because the higher probability of low contrast transitions dominated in the finer resolution image.

Both TM and MSS images produced positive correlation (COR) statistics on the order of $\rho = 0.8$, an indication of a strong association between rows and columns of the GLCM. As the co-occurrence matrix becomes less diagonally dominant the COR value increases. Accordingly, the highest correlations coincided with the χ^2 angle and with the TM scene at all levels of quantization. Unlike the energy statistic, COR, a standardized statistic ranging between zero and one, is useful at all grey levels.

Two other correlation measures based on matrix entropy are strongly associated with the COR statistic. Information correlation 2 (ICOR2) behaves exactly like COR although the value of the correlations is on average 0.1 below COR values. ICOR2 is maximal when the difference between total matrix entropy and the row or column entropies is smallest i.e. when values are more evenly spread throughout the matrix. Conversely, the information correlation 1 (ICOR1) statistic assigns highest negative correlations to matrices in which this entropy differential is smallest making ICOR1 inversely related to COR and ICOR2. TM matrices generally have lower ICOR1 values than do MSS matrices since the difference between total and marginal entropies is smaller for the for the finer texture.

It can be concluded from examination of the co-occurrence statistics that many are intercorrelated. Those statistics that emphasized low contrast transitions, energy and homogeneity, were positively correlated with each other ($\rho = 0.82$) and negatively correlated ($\rho = -0.87$) with entropy and inertia which give weight to high contrast transitions. The correlation statistics, COR, ICOR1, ICOR2 were highly correlated with each other either directly or inversely. If this redundancy is removed, the seven co-occurrence statistics are reduced to three: measures of low contrast, high contrast and correlation.

While some co-occurrence statistics are equally effective at all levels of quantization some are more sensitive with fewer grey levels, others with more. A good middle ground of 16 grey levels coincides with the same choice made for the sake of computational efficiency.

All GLCM statistics were normalized by sample size making direct comparison of TM and MSS textural features valid. The statistics in all cases are sensitive to differences in resolution between the scenes. MSS features consistently show a relatively coarser texture in which high contrast transitions form a larger proportion of co-occurrences than in the TM image.

Filter Statistics

A survey of TM and MSS filter statistics showed that averages and sums (per unit area) are very close in value for the two resolutions but that the standard deviation of the TM images is consistently higher indicating that filtering brings forth more edge detail in the higher frequency TM data. In the next step of analysis, various metrics were used to quantify the resolution dependent differences detected by both the local statistics of the filtered images and by the co-occurrence statistics.

Metric Analysis

For each of the four sets of registered TM and MSS imagery, the distance between features was measured three ways. Results from using Euclidean distance, Gower Similarity, and Bhattacharyya distance are given in Table 10.4. Distances between SUM feature sets are reported only in the case of Euclidean distance as this was the only analysis for which all variables were normalized to a (0,1) range. The SUM variable alone is strictly dependent on sample size; left un-scaled, SUM values distorted feature space making valid Gower similarity or Bhattacharyya distance measures impossible. By contrast, the GLCM statistics, based on probabilities rather than frequencies and calculated from histogram equalized images are standard statistics; likewise AVG and SD values are inherently normalized. A clear picture of texture separability was obtained despite the omission of SUM variables from Bhattacharyya distance and Gower similarity analysis.

Based on mean Gower Similarity, TM and MSS textures are 91% similar when GLCM features are used, 96% similar with AVG features but only 71% similar with SD features. The same pattern is repeated by Bhattacharyya distance measurements: SD features produce twice the separability of the AVG filters, while the GLCM features fall in between. This implies, not surprisingly, that the ratio of within scene to between scene variance is greater for averages than for either standard deviations or moments of the co-occurrence matrix.

Euclidean distances agreed with the other two metrics by singling out the SD features as the most sensitive indicators of resolution dependent textural differences. In Euclidean space, AVG and SUM are nearly identical and somewhat superior to GLCM features for texture separability.

Though not strictly consistent, all three metrics indicate that image pairs A and B are closer than images C and D.

It can be assumed that resolution differences between TM and MSS image pairs are relatively constant since the images were taken under identical conditions. That the distances between pairs are not constant can be attributed to differences in registration, saturation, and surface properties between sets of images. However, if all metrics were in accord, the coefficient of variation among the features should be fairly constant. This is the case for Euclidean distance and Gower similarity measures but is not for Bhattacharyya distance values, a result most likely due to the incorporation of the variance into the calculation of distance.

The Bhattacharyya distance measure may also be inconsistent because it was applied to GLCM and filter variables that in some cases were clearly non-normal whereas it is defined only for Gaussian distributions. Likewise, the error bounds reported in Table 10.4 are not statistically significant but serve as rough limits on the accuracy of calculated distances.

Metric analysis supports the conclusions gathered from inspection of individual co-occurrence statistics: there is a consistent, detectable difference in texture between TM and MSS images. This difference is on the order of 5% to 10% when characterized by GLCM statistics or AVG statistics but as much as 30% when the variance of the filtered images is used. Clearly, the difference in textural information represented by these texture features is far less than what the human eye perceives and what would be expected by a two-fold improvement in resolution. Translation of textural information into joint probabilities or into selectively filtered enhancements and subsequently into summary statistics involves a loss in information that dampens out distinctions between textures that are much more pronounced at the original level. It is not surprising that an improvement or degradation of resolution should correspond to a concomitant increase or decrease in image variance detectable by SD filters, but it is unexpected that the co-occurrence statistics are so relatively insensitive to these changes.

Regression Analysis Results

An initial task before undertaking regression analysis was to survey the distributions of both dependent and predictor variables. Summary statistics for snow-covered area (SCA) are given in Table 10.5. In general the standard deviations are roughly equal to $\frac{1}{4}$ the range thus suggesting non-normal distributions. For a normal distribution three standard deviations on either side of the mean contains almost all cases making the standard deviation approximately $\frac{1}{6}$ the range

[Arkin and Colton, 1970]. This was confirmed by strongly skewed histograms of SCA for each image; low cover samples occurred far more frequently than high cover samples. This is typically the case for data that are counts or amounts because of a fixed zero boundary and a high or unlimited upper bound [Chambers, 1983]. Excessive skewness often implies a correlation of variability with mean level which can produce non-constant variance and heteroscedastic error in a least-squares regression [Bartlett, 1947]. Non-normality invalidates the usual significance tests and heteroscedasticity reduces the precision of the estimates. Fortunately, transformations that stabilize variance also tend to normalize the data; this is usually accomplished by power functions [Chambers, 1983]:

y_i^θ	$\theta < 0$	for right skew
$\log y_i$		$\theta = 0$
$-y_i^\theta$	$\theta > 0$	for left skew

The best transformation was chosen by plotting sorted transformed data against quartiles of the standard normal distribution. The square root transformation ($\theta = 0.5$) turned out to be best for the December and January data while a log transform was necessary for the MSS and TM image pairs.

The predictor variables were surveyed in a similar manner for asymmetrical distributions. The purpose was to gain insight into the behavior of variables and to determine whether transformation of skewed variables to symmetric improved regression models. Distributions of all the co-occurrence statistics show a preponderance of small transitions which is expected for a relatively coarse texture measured at a single pixel displacement. The inertia statistic, which compensates for this typical situation by giving more weight to less frequent, large transitions, is symmetric. Energy and homogeneity statistics are right skewed because the probability of transition term dominates inversely; entropy is left skewed since the term dominates directly. By contrast, the response of the filter variables is scene specific; for TM and MSS images the AVG, SD and SUM statistics are generally symmetric while for the December and January images they are skewed left.

Skewed predictor variables were transformed using power functions and then entered into the leaps and bounds regression for subset selection. Transformed variables do not simplify or improve the models. In many cases, a mix of symmetric and skewed variables have the best explanatory power. In final form, TM/MSS regressions are semi-log functions and the

December/January are "semi-square root" functions.

Regression Significance

A summary of the regression models is given in Tables 10.6a,b. The equations are grouped by image and type of summary statistic used for filtered samples. It is clear from these results that snow-covered area can be successfully regressed on a combination of texture statistics. While the models vary in size between three and seven parameters, the best results are obtained with four or five predictor variables. All regression coefficients are significant at the 0.005 level or better and the least-squares coefficients are on average within 5% of those estimated by robust regression. The proportion of explained variance measured by the adjusted coefficient of determination is in all cases at least 0.95.

Analysis of the residuals was hampered by the log transform of the dependent variable. In log units the residuals are homoscedastic and close to being normally distributed, once corrections were made for negative log values (antilog values between zero and one). The residuals in real values are log-normally distributed, showing larger variance for low snow cover values. The residuals from December and January models, in square root units, were evenly spread around the zero mean line and close to normal on a Q-Q plot.

Least squares linear regression assumes that regressor variables are independent, random variates and that errors are not autocorrelated. When regressor variables and errors are positively autocorrelated, the true variance of regression coefficient estimates is underestimated leading to overestimation of t and F significance tests and inflated R^2 values [Cliff and Ord, 1981]. A basic property of geographic data is its spatial autocorrelation. It can be assumed, therefore, that the texture features used as predictors are autocorrelated to some degree.

In order to check for residual first-order autocorrelation Durbin-Watson statistics were calculated for all models:

$$DW = \frac{\Sigma (u_t - u_{t-1})^2}{\Sigma u_t^{\ 2}} \tag{10.11}$$

Here u_t is the regression residual at location t .

A Durbin-Watson value close to 2 indicates no autocorrelation, a value of zero implies perfect positive autocorrelation and a value of 4 implies negative autocorrelation. Durbin-Watson statistics for all models, given in Table 10.7, are consistent: all but the December models show no postive first-order autocorrelation (significant at the 0.01 level). Statistics for December models

are inconclusive; the null hypothesis of no positive autocorrelation can neither be rejected or accepted. Overall, it can be concluded that the sampling interval de-emphasized adjacent influences and failed to coincide with any large periodicities of the image function. However, in the general case, depending on sampling frequency and site-specific texture pattern, it may be necessary to include autoregressive terms for some models.

Regression Models

Models derived for TM and MSS images that used a combination of co-occurrence statistics and AVG filter values were very similar in composition and coefficient values. The two leading variables were symmetrically distributed co-occurrence statistics followed by a smoothing filter and a Sobel gradient operator. When AVG statistics were replaced with SUM or SD statistics, the models diverged in number of variables, composition and coefficient values; SD models were more dissimilar than AVG models. In general, the AVG/GLCM model characterizing scene texture in the MSS image was unaltered for the TM image despite the two-fold improvement in resolution. Major differences became apparent with the use of SUM variables and were quite pronounced with SD variables.

As can be seen from December and January imagery (Figures 10.5), the snow cover receded substantially in one month from 33% to 19% snow cover. Nevertheless, one pair of models resulted which were quite similar for both images. When GLCM and AVG features were combined, only three parameters were required and of these two were shared in common by the separate models but produced very different coefficients. By contrast, the use of SUM filters meant a large increase in the number of parameters to seven without a corresponding improvement in $\bar{R}^2$. Of these seven parameters only three were in common and the coefficients were quite dissimilar. On the other hand, SD models for each date had five parameters, three of which were identical (ICOR1, fil_0, fil_6) and two of which were highly correlated between dates. All five coefficients were quite similar but no formal test for the equality of regression coefficients through time could be made because the model specifications were not identical. The degree of similarity between models was inferred from the results of forecasting the snow cover at one date using model coefficients derived from the other.

In an effort to get a general equation applicable to both December and January scenes, the data were pooled and re-submitted for regression analysis. The resulting models, though significant and predictive (see Figure 10.9) tended to be over-parameterized ranging from six predictors using AVG filters to eight using SUM filters. Again no conclusions could be drawn about

the similarities of the regression relationships between pooled and individual data sets because the model specifications varied so widely.

Regression Variable Selection

Co-occurrence statistics that are designed to reflect second-order relationships did not outperform the first-order filter statistics. No model was composed exclusively of co-occurrence statistics while the smoothing filter appeared in almost all models. Perhaps the simpler statistics were more suitable for use in a functional relationship because snow-covered area is a high contrast, low variance target easily captured by first-order statistics. The complicated heterogeneous cover of, say, an urban scene may require second-order statistics for purposes of discrimination and classification.

The most significant and predictive equations were those that had four or five parameters. Examination of variables selected by the leaps and bounds method suggests that there are six categories of texture features that contain most of the texture information in a scene: low-contrast GLCM moments, high-contrast GLCM moments, GLCM correlations, the low pass filter (fil_0), vertical edge detectors and horizontal edge detectors. It is possible that a generic equation composed of variables drawn from each category but with scene specific coefficients could be generally applied to snow-covered watersheds.

Prediction Results

The significance of the regressions and the proportion of variance explained by the equations were all uniformly high. These models are admittedly scene-specific and calibrated with a limited data set. The only means of testing model predictability was to perform jackknife regressions summarizing internal predictability with model efficiency scores (see Table 10.8). These results are reported in both transformed and actual units. Clearly, the type of transformation applied to the dependent variable had a strong effect on the outcome of prediction. In log units, the efficiency of TM and MSS regressions was on average about 15% [illegible] r than $\bar{R}^2$ values. When predictions were converted to actual values (number of snow-covered pixels) the efficiencies dropped to zero due to excessive overshooting for the top 8% of the values. If the domain of prediction is limited to low and mid-range values the efficiencies return to those measured in log units. The coefficients proved to be quite stable, varying on average 2.5% but in no case more than 6.5%. Log transformation linearized the model making possible a highly significant regression, but because small log residuals for high values converted exponentially into much larger actual residuals, the domain for accurate prediction of real values was limited to 25% SCA.

The over-prediction problem inherent in log transformed data was not encountered when the data were square-root transformed. Jackknife efficiencies in square root units were quite high: 5% lower than $\bar{R}^2$ values and when measured in real values only 10% lower than $\bar{R}^2$. Figures 10.10a,b and 10.11a,b show the results of jackknife regression for the December scene in both actual and real values using AVG filters.

Regressions for December and January that involved SD filters differed from each other by two variables. Two edge filters in the December equation were replaced by edge/spot filters in the January model. The coefficients were on the whole quite similar. So it is not unexpected that when each model was applied to the other scene that model efficiencies, in transformed terms, differed by only 5%. More importantly, both models turned out to be surprisingly efficient at prediction: 91% and 95% of the variance was explained by the models (see Table 10.8). Figures 10.12a,b and 10.13a,b are plots of cross-predicted versus actual values for the two dates.

By contrast, the AVG models for the two dates were poor predictors even though the individual regressions had high $\bar{R}^2$. The December AVG model predicted January SCA with 44% efficiency and the reverse was only 40% efficient. SUM models for both images were so large (p=7) that no attempt was made to test predictability. In general, predictive analysis re-emphasized what was found from jackknife regressions: standard deviations of filtered samples were by far the best predictors.

The remarkably good predictability between scenes that differed in snow coverage by 15% implies that scene dependent parameters are robust enough to encompass recessional pattern changes. It may be possible to derive general parameters for moderately sized basins for use in the melt season when patterns of snow recession are duplicated year to year.

10.7. Discussion and Conclusion

Texture Characteristics

When an image is considered to represent a random field, the co-occurrence matrix becomes an estimate of the joint probability density function for pixels separated by given row and column shifts. The autocorrelation at this spatial lag is determined by the matrix transition probabilities. In the images of snow cover, the joint pixel correlations at a single pixel lag were high (ρ=0.85) located along the slope of the central peak of the autocorrelation function. A comparison of co-occurrence statistics from different resolutions is really a matter of comparing the rate of change in the initial slope of the autocorrelation function; steep slopes correspond to fine textures, gentle

slopes to coarser textures.

Detecting texture periodicities at far outlying joint positions is likely only for regular, artificial patterns. For natural scenes it is most appropriate to carry out GLCM analysis over relatively small windows at the minimum displacement. Judging from the results of this study, quantization level is most critical when using small joint displacements because it acts to enhance or dampen the differences in slope of the autocorrelation function. Beyond five pixels large quantizations are only marginally more informative. It should also be noted that if textures are to be analyzed over immediately adjacent neighborhoods then directional differences between textures become more acute and rotationally averaged measures will overlook an important feature for distinguishing closely related textures.

The GLCM features are moments of the joint probability distribution that describe the spread of values away from the central diagonal, a feature equivalent to the autocorrelation peak reduced to two dimensions. As such, they are descriptors of contrast and correlation; low contrast transitions are close to the diagonal, high contrast transitions are more distant and the correlations reflect the degree of difference in transition values. When MSS and TM co-occurrence statistics from the same site were compared, the MSS image was coarser both in terms of contrast and correlation.

Metric Analysis

The above result only served to verify the self-evident. It was necessary to use metric analysis to find the magnitude and variability of these texture differences. The dissimilarity between the two resolutions measured between the four image pairs using the standard GLCM statistics or AVG/SUM statistics was only five to ten percent, but this increased to 30% when the standard deviation of the edge filtered samples was used instead. That the variance (second moment) of a local first order variable should be more informative than the mean (first moment) is not surprising. What is unexpected is the much greater separability afforded by a first order moment relative to the complex moments of the joint probability distribution.

Laws [1980] discovered that SD measures were best for discrimination but not necessarily for segmentation. They acted as measures of local contrast tending to locate edges rather than regions. The consistently higher SD's of the TM images no doubt indicate the greater edge detail created by improved resolution. As measures of local contrast SD features encompass the variability of an entire window whereas GLCM measures of contrast are compressed histograms of greytone transitions over a distance of a single pixel. The co-occurrence matrix provides information

on the adjacent (or the joint) while the filter SD provides information on the local. Gagalowicz [1981] and Julesz [1975] have found that texture discrimination is achieved locally, not globally so that properties averaged over a local region may be more informative than those ascertained from joint relationships. In other words, more information on texture structure may be lost by generating the GLCM and its moments than in filtering and calculating variance.

TM vs MSS Regressions

Metric analysis made it clear that the relationship between resolution and texture separability is not one to one. In fact, it is likely that studies employing standard GLCM statistics or SUM/AVG filters could well substitute MSS data for TM without considerable loss in information. In keeping with distance metric results, the AVG and to a lesser extent SUM regression models at the two resolutions agreed while SD models differed considerably. When regressions were worked out for two dates at TM resolution, both AVG and SD models were similar in composition and, for the latter, in coefficient values. Any conclusions that might be drawn about resolution dependent textural differences from comparing the two sets of regression models are confounded by a lack of control on the SCA variable. Snow cover varied 30% between the resolutions due to limitations of thresholding and spectral/spatial disparity between resolutions, while snow receded only 14% between sequential images of the same resolution.

Judging from jackknife regression results, the relationship between SCA and texture measures was of comparable strength at the two resolutions. TM model efficiencies were only 5% better than MSS efficiencies. But without actual ground data to both calibrate and test the models it can only be said that they were both internally consistent.

Regression and Prediction Results

In general regression of snow area onto parameters describing its distribution was successful. All twelve models were highly significant and explained a large proportion of the variance. For December models, these results should be viewed cautiously in light of positive spatial autocorrelation effects leading to underestimation of coefficient variance. Nevertheless, some of these models were highly predictive. At 90 - 95% efficiency the semi-square root models using SD variables were especially good predictors. Operationally, they could be used to obtain snow cover estimates when snow patterns are very discontinuous making manual or digital snow classification difficult.

The domain of accurate prediction is limited by the transformation chosen for the dependent variable. Transformations that stabilize variance and symmetricize distributions should be

selected with the scale of the predicted variable in mind. For these models a square root transform was preferable to taking the log. In real rather than transformed values, log models began to seriously overshoot at 25% snow cover while square root models were stable up to 70 or 80% SCA. Using linear modeling and a moderate sample size this inherent problem will always limit the domain of prediction to some degree because the uneven distribution of sample points over the range of prediction results in greater uncertainty for under-represented points.

The aim of this study was not to successfully predict SCA *per se* but to establish the methodologies for eventually predicting snow depth, a more direct indicator of snowmelt runoff. To that end, it was learned that parameters of the texture regression models are scene and pattern specific but are fortunately robust enough to accommodate considerable latitude in the actual snow pattern formations, making them useful through time as the snowline recedes.

It may be possible, after further studies of models derived at a variety of sites, to construct a standard model based on all six or some set of the six categories of texture features used here. Without question the smoothing filter (fil_0) would be a necessary parameter. Among the twelve models studied it was nearly ubiquitous. Correlations between fil_0 statistics and SCA ranged between 0.72 and 0.95 (see Table 10.9) making it the single most predictive variable. Obviously, local summary statistics of the smoothed image are highly correlated with coverage because snow is such a singularly bright, high-contrast target within the scene. In most models this low frequency information was augmented by high pass filter variables and some mix of GLCM statistics that contributed information on contrast and correlation in the immediate neighborhood of each pixel. In general, it was found that GLCM and texture energy features are well suited for detecting bright, high-contrast snow cover patterns because they operate in the first case by measuring contrast differences or in the latter by detecting edge structure.

The high $\bar{R}^2$ values of the regression models were not good indicators of predictive power. Using a cross-prediction test only models based on a majority of SD variables were useful under different conditions. Thus the results of metric and regression analysis were in accord: separability coincided with predictability. The standard deviation was superior for both purposes because it reflected the level of high frequency information consistently both within and between scenes. Depending on the site, AVG and SUM statistics could be highly intercorrelated or quite unrelated while SD values remained at a consistent level of intercorrelation at different sites. It should be noted that filtered images retained full quantization while GLCM images were necessarily reduced. The power of SD statistics may in part be due to the greater information inherent in

higher quantizations. It appears that breaking down texture structure into joint relationships for a limited number of grey tones involves a loss in information greater than that involved in taking local statistics of filtered images.

Conclusion

The difference in resolution between MSS and TM images which is so dramatic to the eye was critical for classification accuracy. Snow classifications from TM images were far more detailed and complete than MSS classifications yet principal component analysis revealed that spectral information did not play a large part in this disparity. The data plane used for thresholding snow cover in the TM images was essentially a reduced-variance visible band somewhat augmented by shortwave IR data for cloud discrimination purposes. TM near infrared data were redundant to visible data and could be eliminated from the data plane. The MSS data plane was also in effect a reduced-variance visible image supplemented by near IR data which, as in TM component analysis, supplied mostly redundant information with respect to the first axis of maximum variation. In short, for binary classifications, snow is easily detected in the visible range but may require shortwave IR data to aid in distinguishing cloud cover from snow.

Measures of joint grey-tone relationships and local statistics of high frequency enhanced images do not duplicate perceptual sensitivity to textural detail apparent with greater resolution. It is not surprising that these methods do not parallel those used in complex, non-linear, hierarchical visual processing. If the texture measures failed to achieve the sensitivity of human perceptual capabilities they successfully served as descriptors of mesoscale spatial distribution in functional relationships between snow-covered area and areal distribution. Despite inherent data problems of skewed distributions and autocorrelated samples, linear relationships making use of the standard deviation of convolved images were 91- 96% efficient in predicting snow-covered area for a given site under two snow cover patterns.

Exploratory and particular rather than generalized, the regression analyses presented here were undertaken as a feasibility study yet they did yield some general observations on the nature of natural textures. Texture models are a subset of image models which Ahuja and Schachter [1981] have grouped into the stochastic and pixel-based or the deterministic and region-based. Global two-dimensional stochastic models specified by a particular random field can be described variously by the autocorrelation function, variograms, means, gradients or spatial dependencies [Ahuja and Schachter, 1981]. Specified in this manner, a global model can be viewed as a combination of the ideal data modified by a point spread function plus additive noise. For example,

Faugeras and Pratt [1980] successfully decomposed global textures into measures of the autocorrelation function and moments of the histogram of the decorrelated white noise field. This description is not unique in all cases; global models breakdown when the mean and autocorrelation function are no longer stationary. It becomes necessary to include a set of means and a spatial function to modify the symmetric autocorrelation function. In other words, with inhomogeneities global models become local models.

If global properties do not hold or if an image model cannot be formulated, a texture must be described empirically at the pixel or local level. Determining joint and conditional probabilities is one such approach but as Ahuja and Schachter warn, a joint probability density function may be an overspecification lacking in abstraction. Since neither over-generalized global models, or highly detailed joint relationships are entirely successful descriptions of natural texture it becomes necessary to describe image statistics as local spatial averages.

On the basis of perceptual experiments, Gagalowicz [1981] found that where local second order statistics differ from global ones, the eye is able to detect a textural difference; visual discrimination is thus a local process. In addition, Julesz [1975] has speculated after years of perceptual testing that visual discrimination may require only local first-order statistics of simple, pooled feature extractors. The results of analyzing snow cover texture support the notion that texture is a local property. Local standard deviations were more effective for separating textures and more reliable for linear prediction. Measures of local variance appear to be quite informative yet general enough to avoid over-sensitivity to noise. Moreover, local statistics taken from a series of edge enhanced images do a better job at capturing edge structure than most stochastic models which have been criticized for failing to account for real-world spatial structure [Modestino et al., 1981]. In conclusion, the results of this study confirm those recently reported elsewhere [Pietikäinen *et al.*, 1983] that Laws texture features are powerful and efficient descriptors of natural textures.

10.8. Appendix

Co-occurrence Features

$p(i,j) =$ matrix entry of the normalized co-occurrence matrix.

$Ng =$ number of grey levels.

Energy

$$ENG = \sum_{i=1}^{N_g} \sum_{j=1}^{N_g} p(i,j)^2$$

Homogeneity

$$HOM = \sum_{i=1}^{N_g} \sum_{j=1}^{N_g} \frac{1}{1+(i-j)^2} \; p(i,j)$$

Entropy

$$ENT = -\sum_{i=1}^{N_g} \sum_{j=1}^{N_g} p(i,j) \log p(i,j)$$

Inertia

$$INR = \sum_{i=1}^{N_g} \sum_{j=1}^{N_g} (i-j)^2 \, p(i,j)$$

Correlation

$$COR = \frac{\sum_{i=1}^{N_g} \sum_{j=1}^{N_g} (i,j \; p(i,j)) - m_I \; m_J}{(\sigma_I \; \sigma_J)}$$

where

$$m_I = \sum_{i=1}^{N_g} \sum_{j=1}^{N_g} i \; p(i,j)$$

$$m_J = \sum_{i=1}^{N_g} \sum_{j=1}^{N_g} j \; p(i,j)$$

$$\sigma_I = \sum_{i=1}^{N_g} \sum_{j=1}^{N_g} i^2 \, p(i,j) - \left(\sum_{i=1}^{N_g} \sum_{j=1}^{N_g} i \; p(i,j)^2 \right)^{1/2}$$

$$\sigma_J = \sum_{i=1}^{N_g} \sum_{j=1}^{N_g} j^2 \, p(i,j) - \left(\sum_{i=1}^{N_g} \sum_{j=1}^{N_g} j \; p(i,j)^2 \right)^{1/2}$$

Information Correlation 1

$$ICOR\,1 = \frac{HXY - HXY\,1}{\max(HX, HY)}$$

where

$$HXY = ENT$$

$$HXY\,1 = -\sum_{i=1}^{N_g}\sum_{j=1}^{N_g} p(i,j)\log(p_x(i)\,p_y(j))$$

$$HX = \sum_{i=1}^{N_g} i\,\log(p_x(i))$$

$$HY = \sum_{j=1}^{N_g} j\,\log(p_y(j))$$

$$p_x(i) = \sum_{j=1}^{N_g} p(i,j)$$

$$p_y(j) = \sum_{i=1}^{N_g} p(i,j)$$

Information Correlation 2

$$ICOR\,2 = (1 - \exp[-2.0\,(HXY\,2 - HXY)])^{1/2}$$

where

$$HXY\,2 = -\sum_{i=1}^{N_g}\sum_{j=1}^{N_g} p_x(i)\,p_y(j)\log(p_x(i)\,p_y(j))$$

Convolution Masks

$$fil_0 = \begin{bmatrix} 1 & 2 & 1 \\ 2 & 4 & 2 \\ 1 & 2 & 1 \end{bmatrix} \qquad fil_1 = \begin{bmatrix} -1 & 0 & 1 \\ -2 & 0 & 2 \\ -1 & 0 & 1 \end{bmatrix} \qquad fil_2 = \begin{bmatrix} -1 & 2 & -1 \\ -2 & 4 & -2 \\ -1 & 2 & -1 \end{bmatrix}$$

Smoothing Filter Vertical Sobel

$$fil_3 = \begin{bmatrix} -1 & -2 & -1 \\ 0 & 0 & 0 \\ 1 & 2 & 1 \end{bmatrix} \quad fil_4 = \begin{bmatrix} 1 & 0 & -1 \\ 0 & 0 & 0 \\ -1 & 0 & 1 \end{bmatrix} \quad fil_5 = \begin{bmatrix} 1 & -2 & 1 \\ 0 & 0 & 0 \\ -1 & 2 & -1 \end{bmatrix}$$

Horizontal Sobel

$$fil_6 = \begin{bmatrix} -1 & -2 & -1 \\ 2 & 4 & 2 \\ -1 & -2 & -1 \end{bmatrix} \quad fil_7 = \begin{bmatrix} 1 & 0 & -1 \\ -2 & 0 & 2 \\ 1 & 0 & -1 \end{bmatrix} \quad fil_8 = \begin{bmatrix} 1 & -2 & 1 \\ -2 & 4 & -2 \\ 1 & -2 & 1 \end{bmatrix}$$

Laplacian Filter

10.9. Symbols

AVG	Average of the absolute value of pixels within a specified window in an image convolved with a Laws filter.
COR	Correlation co-occurrence statistic
ENG	Energy co-occurrence statistic
ENT	Entropy co-occurrence statistic
fil_0	Laws convolution filter 0 : smoothing filter
fil_1	Laws convolution filter 1 : vertical Sobel filter
fil_2	Laws convolution filter 2
fil_3	Laws convolution filter 3 : horizontal Sobel filter
fil_4	Laws convolution filter 4
fil_5	Laws convolution filter 5
fil_6	Laws convolution filter 6
fil_7	Laws convolution filter 7
fil_8	Laws convolution filter 8 : Laplacian filter
GLCM	Grey-level co-occurrence matrix

HOM	Homogeneity co-occurrence statistic
ICOR1	Information correlation 1 co-occurrence statistic
ICOR2	Information correlation 2 co-occurrence statistic
INR	Inertia co-occurrence statistic
MSS	Multispectral Scanner
SCA	Snow-covered area
SD	Standard deviation of pixels within a specified window of an image convolved with a Laws filter.
SUM	Sum of the absolute value of pixels within a specified window of an image convolved with a Laws filter.
TM	Thematic Mapper

10.10. Tables

Table 10 1 Snow Classification Training Site Statistics, DN values

Band	Mean	Std Dev	CV	Min	Max	Range
TM2	117	12	10%	42	140	98
TM2/TM3	58	2	4%	53	70	17
TM2/TM5	91	9	10%	34	112	78
PC1 (TM2,5)	128	11	9%	100	220	120
PC1 (TM2,3,4,5,7)	130	15	12%	101	226	125

Table 10 2. Loadings of Principal Components

Band	Principal Component			
	PC1	Pct. Var	PC2	Pct. Var
TM2	-0.52	98.2%	-0.46	1.3%
TM3	-0.66		-0.32	
TM4	-0.53		0.82	
TM5	-0.10		0.14	
TM7	-0.05		0.01	
MSS4	-0.47	98.3%	-0.55	1.3%
MSS5	-0.54		-0.39	
MSS6	-0.60		0.46	
MSS7	-0.35		0.57	
TM2	-0.88	99.1%	-0.15	0.9%
TM5	-0.15		0.88	
MSS4	-0.80	97.5%	-0.59	2.5%
MSS7	-0.59		0.80	

Table 10.3. TM vs MSS χ^2 Angle

	Correlations			
	A	B	C	D
ρ	0.50	0.48	0.74	0.47

Table 10.4. Distances Between TM and MSS Texture Features

	Eulcidean Distance			
Image	GLCM	AVG	SD	SUM
A	7.22	8.33	7.96	8.30
B	8.98	8.19	10.47	8.04
C	10.20	11.56	13.89	11.46
D	11.73	13.00	14.84	13.05
Mean	9.53	10.27	12.29	10.21
SD	1.91	2.39	3.72	2.45
CV	20%	23%	30%	24%

Gower Similarity

	Filter Statistic		
Image	GLCM	AVG	SD
A	0.90	0.97	0.72
B	0.90	0.96	0.72
C	0.92	0.95	0.68
D	0.91	0.95	0.71
Mean	0.91	0.96	0.71
SD	0.009	0.012	0.020
CV	1.1	1.2	2.7

Bhattacharyya Distance

	Filter Statistic					
Image	GLCM	approx error	AVG	approx error	SD	approx. error
A	0.90	0.20	1.28	0.15	2.87	0.04
B	0.87	0.23	1.04	0.18	2.86	0.04
C	1.32	0.15	1.39	0.14	2.94	0.04
D	2.26	0.03	1.48	0.15	2.51	0.05
Mean	1.59		1.30		2.79	
SD	1.13		0.19		0.19	
CV	71%		14%		7%	

Table 10.5. Snow-Covered Area

	MSS		TM		DEC		JAN	
	# of Pixels	Pct. Cover	# of Pixels	Pct. Cover	# of Pixels	Pct. Cover	# of Pixels	Pct Cover
Mean	23	9%	70	7%	340	33%	199	19%
Std. Dev	24	10%	82	8%	262	26%	249	24%
CV	107%	107%	117%	117%	77%	77%	125%	125%
Range	0-92	0-36%	0-344	0-34%	0-1014	0-99%	0-992	0-97%

Table 10.6a. Regression Models

Image	Filter	Coefficients		*t value*	$\bar{R}^2$	*F value*	DF	Resid SE
MSS	AVG	INR	0.113	5.58	.946	280	4,60	.285
		ICOR1	-5.030	-8.36				
		fil_0	0.011	10.87				
		fil_3	-0.019	-9.39				
MSS	SD	HOM	1.760	2.38	.955	316	4,60	.269
		ENT	0.668	3.54				
		fil_0	0.034	9.47				
		fil_2	-0.019	-3.88				
MSS	SUM	INR	5.79e-2	3.75	.963	310	5,59	.244
		ICOR2	3.400	6.80				
		fil_0	8.53e-5	13.68				
		fil_1	-4.33e-5	-3.79				
		fil_3	-4.68e-5	-3.90				
TM	AVG	INR	0.299	7.05	.962	410	4,60	.315
		ICOR1	-6.86	-8.91				
		fil_0	0.017	11.65				
		fil_5	-0.030	-9.98				
TM	SD	fil_0	0.064	15.73	.982	834	4,60	.223
		fil_2	-0.030	-2.47				
		fil_6	-0.027	-2.16				
		fil_8	0.051	6.75				
TM	SUM	INR	0.258	6.01	.965	442	4,60	.304
		ICOR1	-3.909	-5.42				
		fil_0	4.48e-5	13.17				
		fil_4	-2.34e-5	-8.08				

Table 10.6b. Regression Models Continued

Image	Filter	Coefficients		t value	$\bar{R}^2$	F value	DF	Resid SE
DEC	AVG	ENG	-7.25	-2.91	.981	1057	3,61	2.165
		COR	-0.484	-2.75				
DEC	SD	ICOR1	-26.88	-4.91	.991	1352	5,59	1.787
		fil_0	0.102	3.49				
DEC	SUM	COR	45.03	8.75	.986	582	7,57	2.295
		HOM	-32.44	-12.10				
JAN	AVG	ENG	44.26	7.03	.950	410	3,61	3.141
		HOM	-21.86	-7.91				
JAN	SD	ICOR1	-19.26	-5.45	.988	1036	5,59	1.560
		fil_0	0.117	4.32				
JAN	SUM	COR	16.59	5.80	.972	969	7,57	2.484
		HOM	-60.06	-9.85				
DEC/	SD	COR	-12.19	-3.89	.987	1446	7,121	1.836
JAN		ENT	2.47	2.47				

Table 10.7. Durbin-Watson Statistics

Image	AVG		SD		SUM	
	DW	ρ	DW	ρ	DW	ρ
TM	1.66	0.17	2.19	-0.09	1.76	0.12
MSS	1.61	0.20	1.66	0.17	1.86	0.07
DEC	1.39*	0.30	1.61*	0.20	1.60*	0.20
JAN	1.64	0.18	1.68	0.16	2.00	-0.002

* cannot reject or accept null hypothesis of no positive autocorrelation. All other values show no positive autocorrelation at the 1% level.

Table 10.8. Prediction Results

Model Efficiencies

		Jackknife			Cross-Prediction	
		Transformed	Actual	N	Transformed	Actual
MSS	AVG	.76	.82	61		
TM	AVG	.81	.68	59		
DEC	AVG	.90	.87	64	.40	.36
	SD	.95	.91	64	.91	.84
JAN	AVG	.89	.85	64	.44	.39
	SD	.97	.94	64	.96	.91

Table 10.9. SCA and Fil_0 Correlations

SCA	AVG	SD	SUM
TM	.72	.91	.83
MSS	.73	.87	.84
DEC	.95	.80	.90
JAN	.89	.94	.96

ORIGINAL PAGE IS
OF POOR QUALITY

10.11. Figures

Figure 10.1 Snow texture study sites: TM image C (upper left), TM Image A (upper right), MSS image C (lower left), MSS Image A (lower right).

Figure 10.2 Snow texture study sites: TM image D (upper left), TM image B (upper right), MSS image D (lower left), MSS image B (lower right).

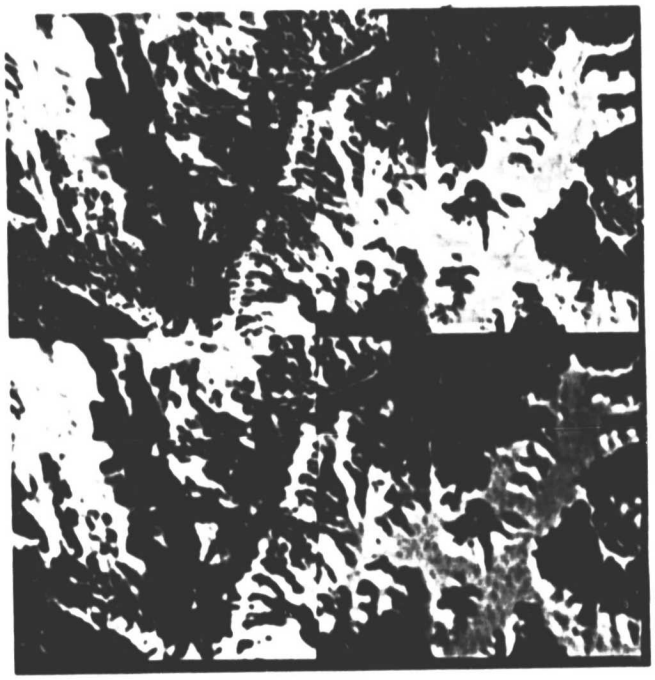

ORIGINAL PAGE IS
OF POOR QUALITY

Figure 10.3 First principal component of TM bands 2, 3, 4, 5 and 7 (upper left), first principal component of TM bands 2 and 5 (upper right), snow-covered area (lower left) and TM band 2 (lower right).

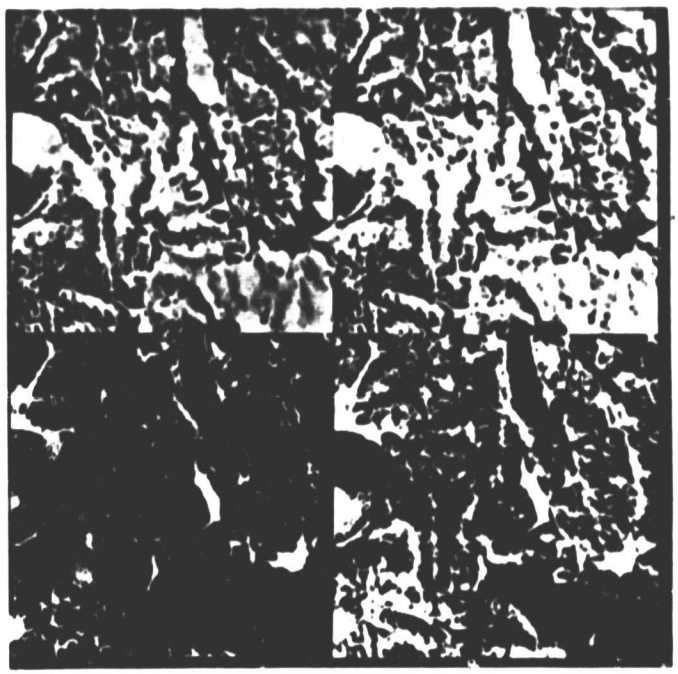

Figure 10.4 MSS band 4, image A (upper left), TM band 2, image A (upper right), MSS snow-covered area (lower left) and TM snow-covered area (lower right).

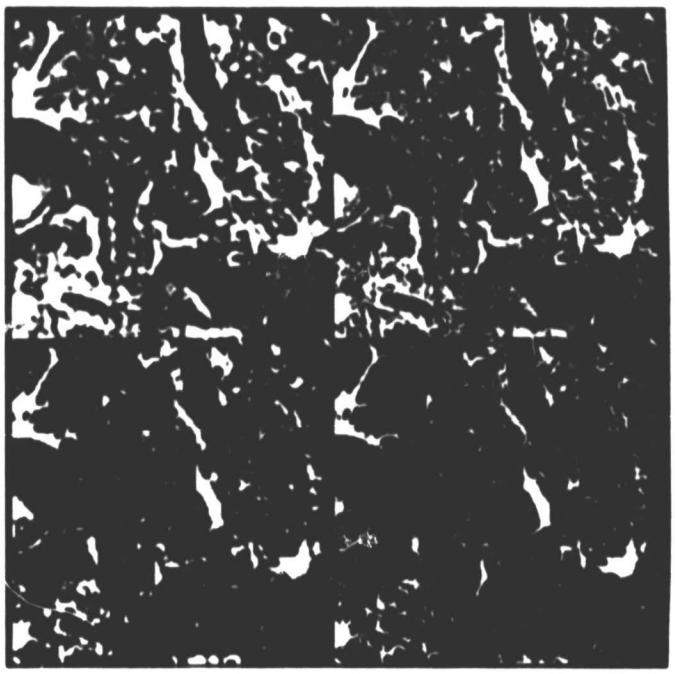

ORIGINAL PAGE IS
OF POOR QUALITY

Figure 10.5 January TM band 2 (upper left), December TM band 2 (upper right), January snow-covered area (lower left), December snow-covered area (lower left).

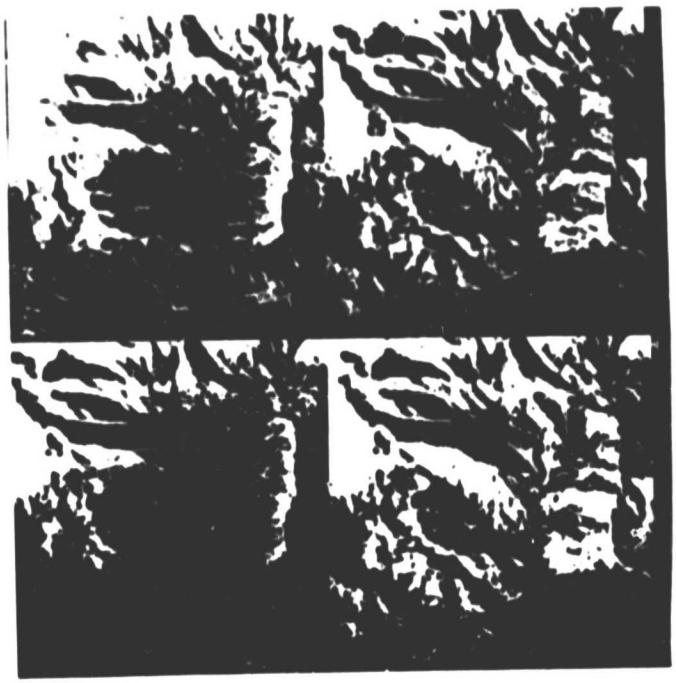

Figure 10.6 TM and MSS chi-square values versus co-occurrence displacement distances at four quantization levels.

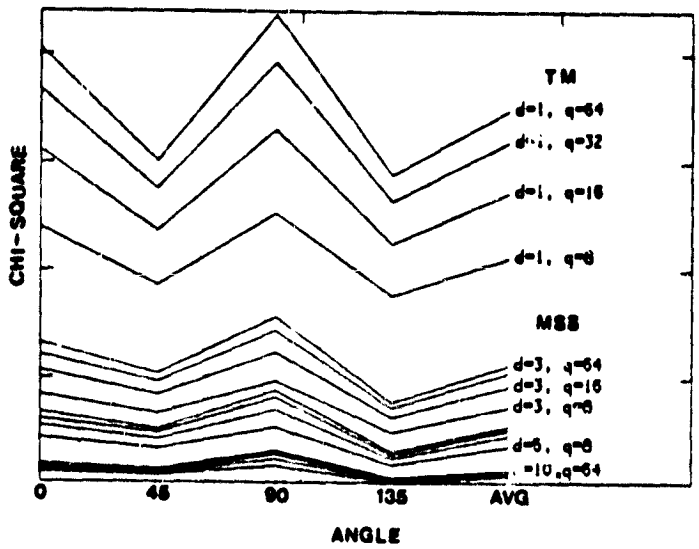

Figure 10.7 TM and MSS chi-square values versus co-occurrence displacement angles for all distances and quantizations.

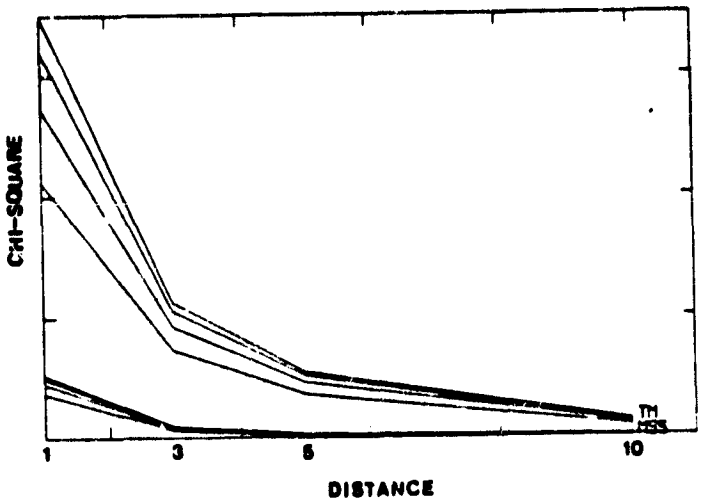

ORIGINAL PAGE IS
OF POOR QUALITY

Figures 10.8a,b TM and MSS co-occurrence matrices, 16 grey-levels.

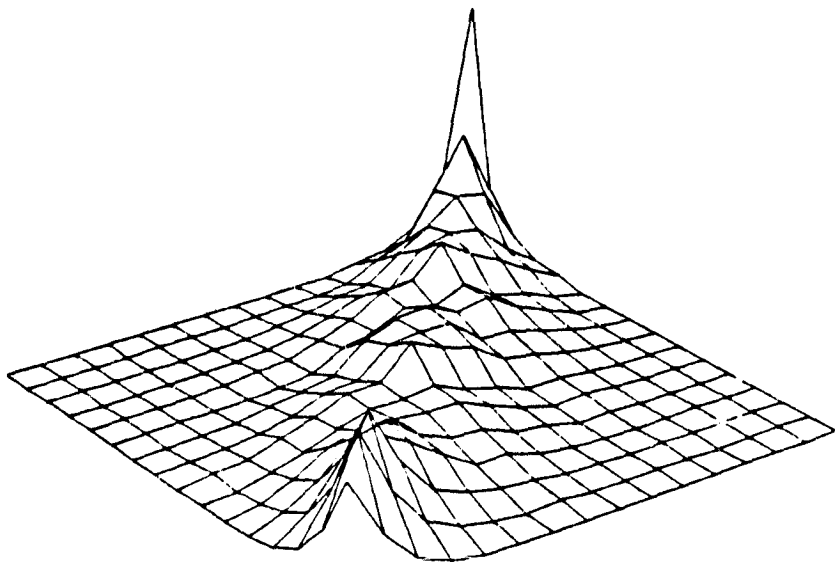

Grey Level Co-occurrence Matrix, Mss Image A
Quantization=16, Vertical Exaggeration=20

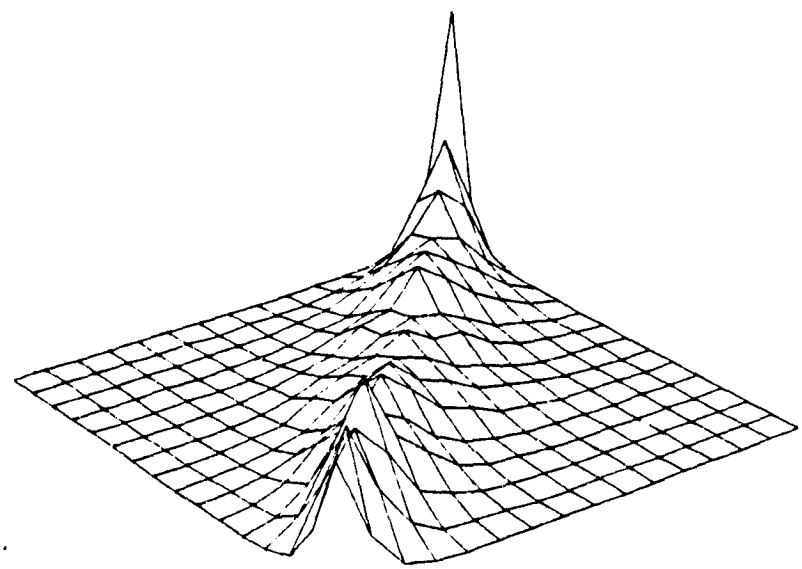

Grey Level Co-Occurrence Matrix, Quantization= 16
TM Image A, (Vertical Exaggeration= 20)

C-2

Figure 10.9 December predictions using pooled data in transformed units (square root).

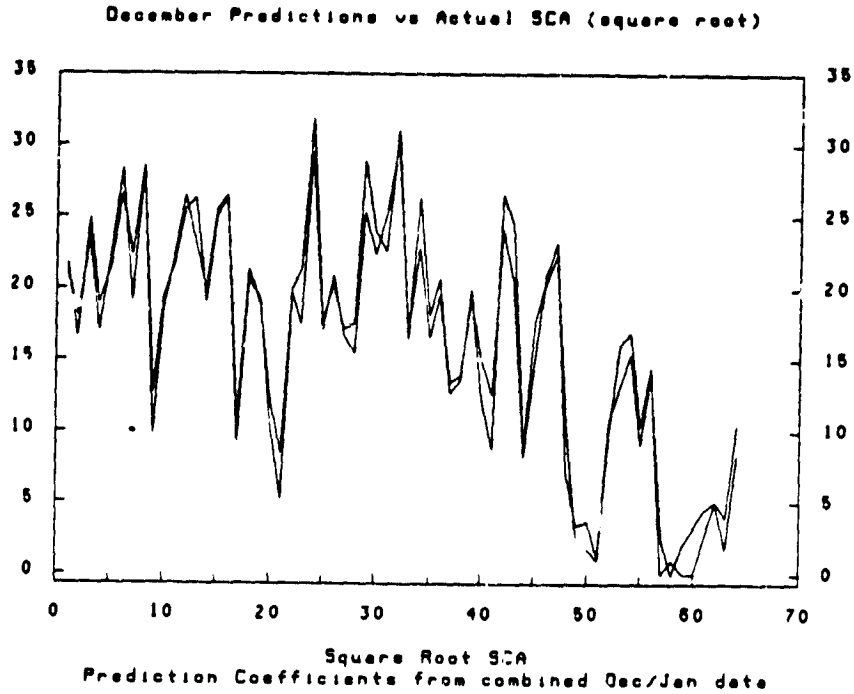

ORIGINAL PAGE IS
OF POOR QUALITY

Figures 10.10a,b December AVG model jackknife predictions by sample and plotted against actual SCA in transformed units (square root).

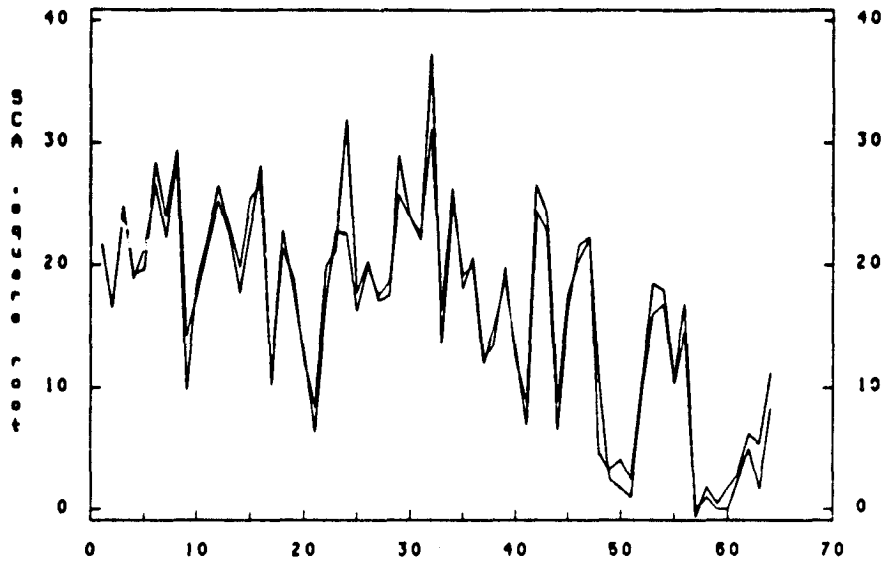

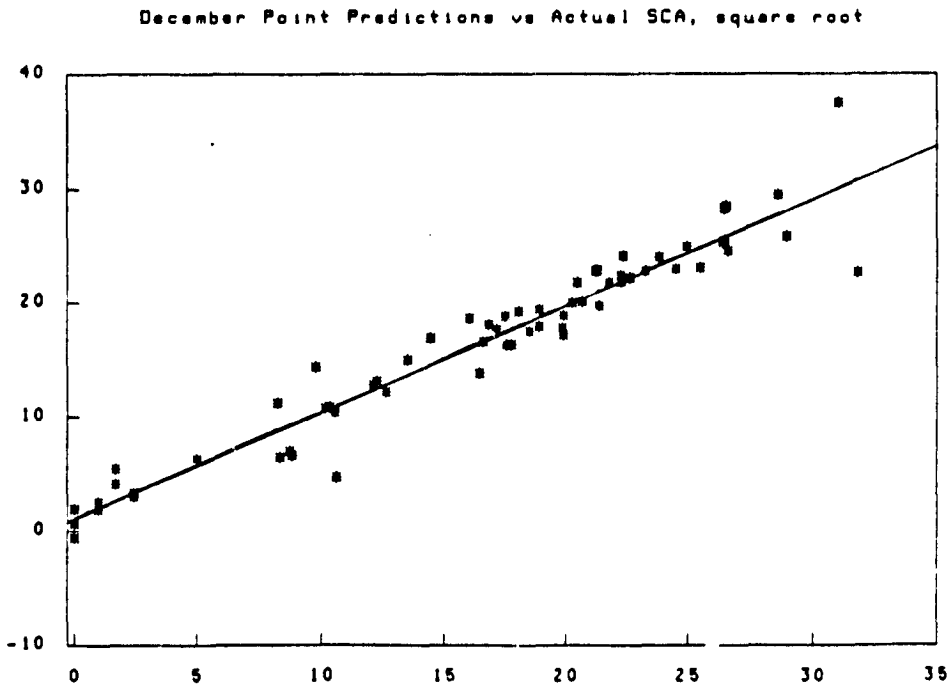

Figures 10.11a,b December AVG model jackknife predictions by sample and plotted against actual SCA in real units (snow-covered pixels).

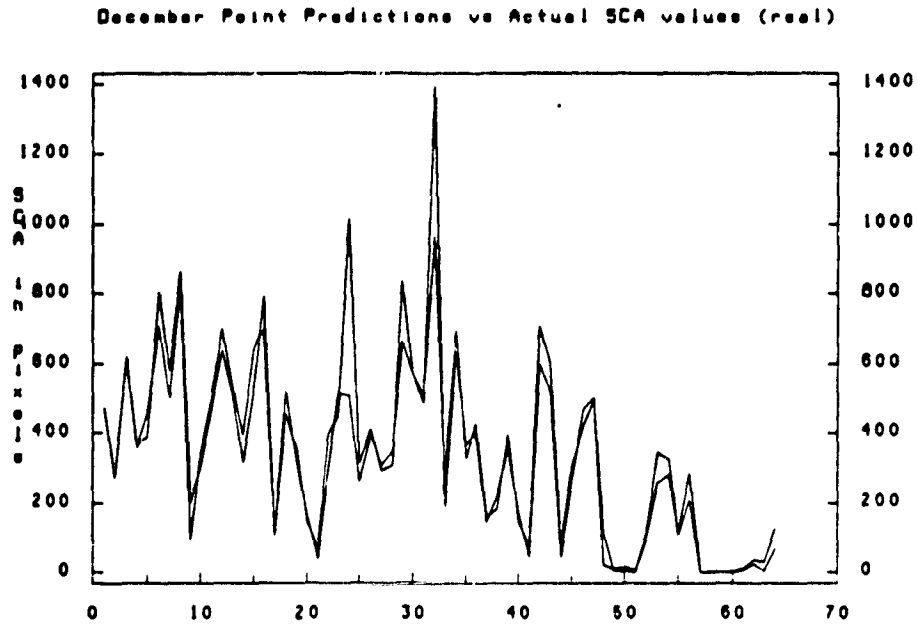

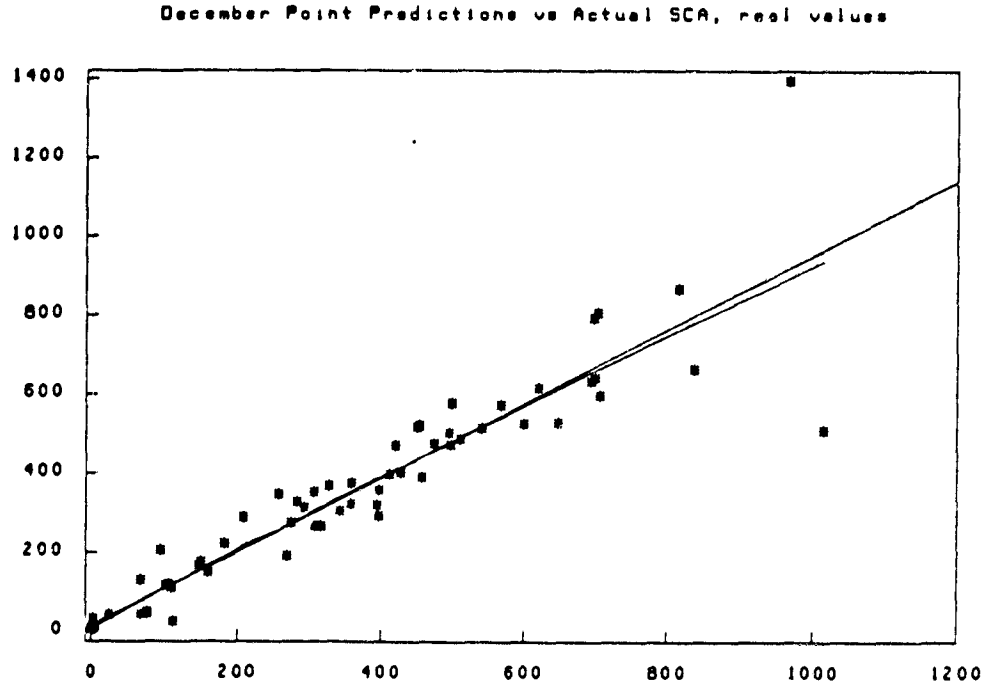

Figures 10.12a,b December cross-predictions using January coefficients by sample and plotted against actual values in real units (snow- covered pixels).

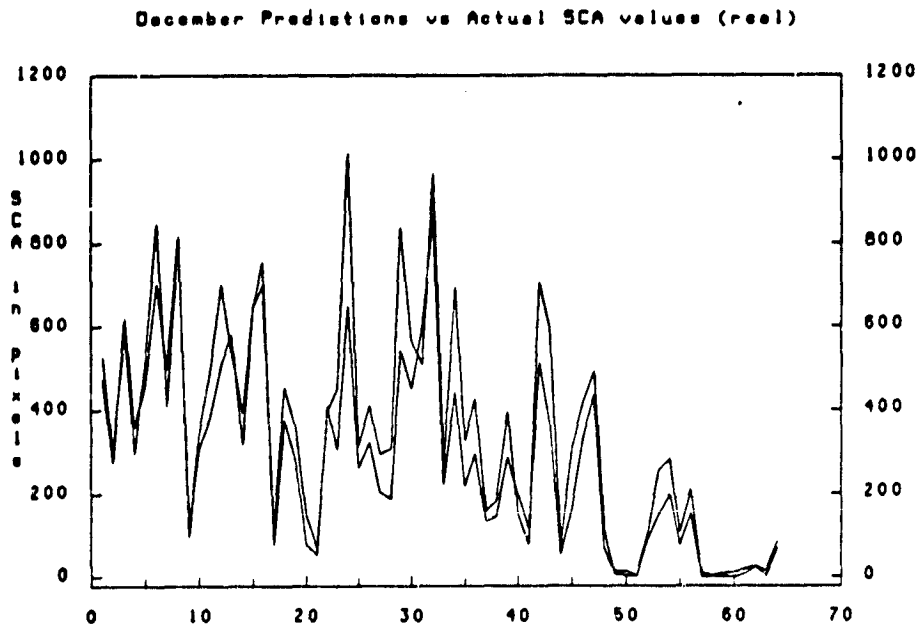

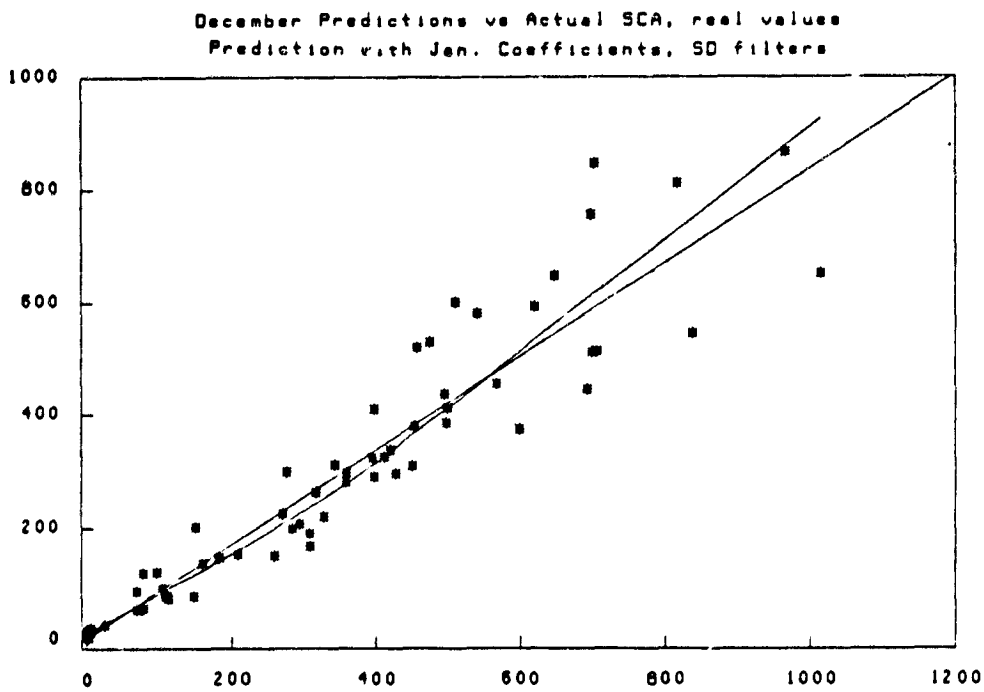

ORIGINAL PAGE IS
OF POOR QUALITY

Figures 10.13a,b January cross-predictions using December coefficients by sample and plotted against actual values in real units (snow-covered pixels).

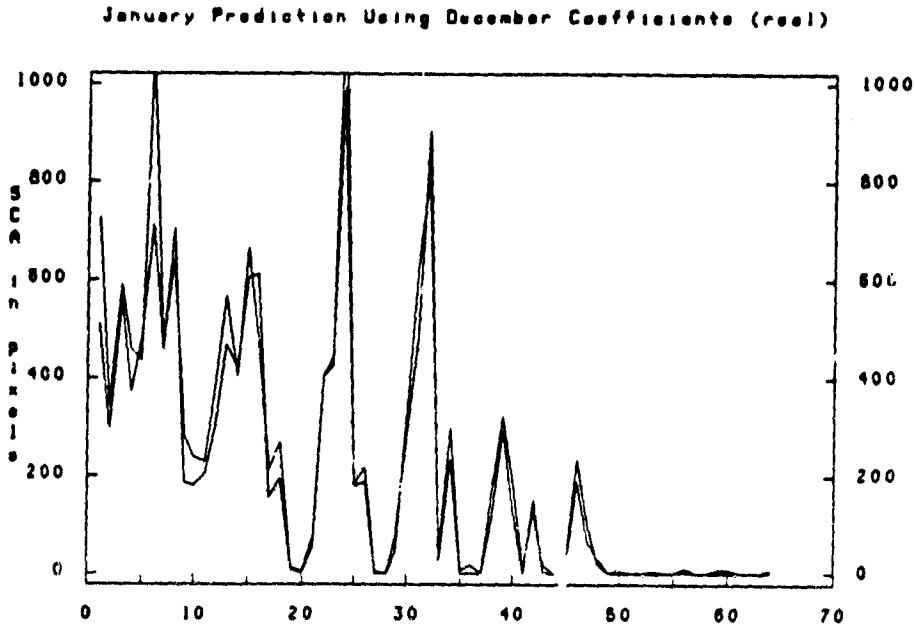

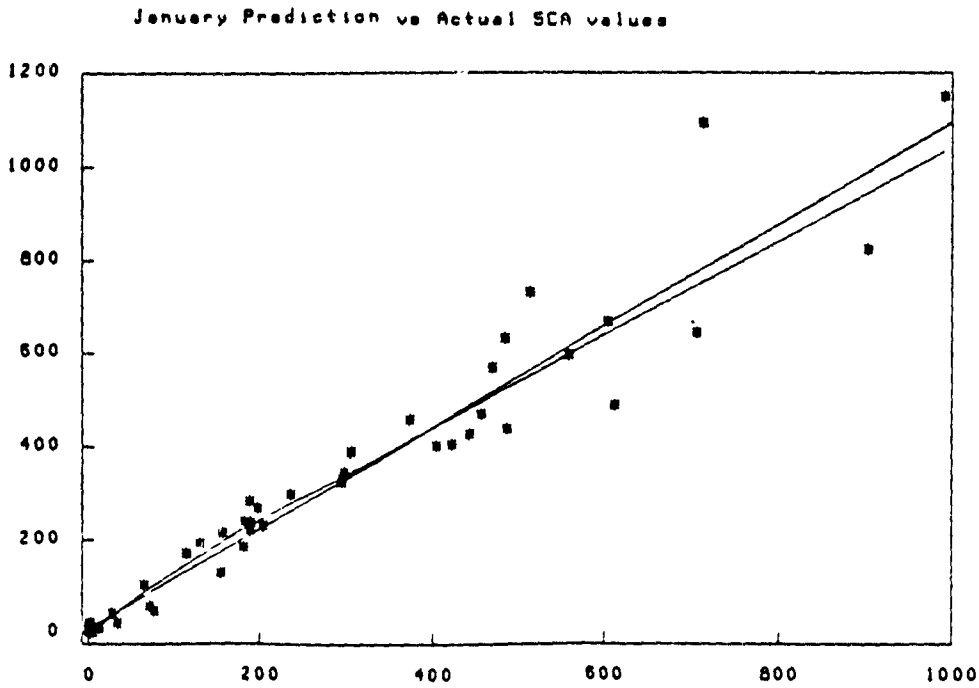

11. References

Adams, W. P. and N. T. Roulet, "Areal differentiation of land and lake snowcover in a small sub-arctic drainage basin," *Nordic Hydrology*, vol. 13, pp. 139-156, 1982.

Ahuja, N. and B. J. Schachter, "Image models," *Computing Surveys*, vol. 13 , pp. 373-397, 1981.

Andrews, H. C. and B. R. Hunt, *Digital Image Restoration*, pp. 1-238, Prentice-Hall, Englewood Cliffs, NJ, 1977.

Anuta, P. E., L. A. Bartolucci, M. E. Dean, D. F. Lozano, E. Malaret, C. D. McGillem, J. A. Valdés, and C. R. Valenzuela, "Landsat-4 MSS and Thematic Mapper data quality and information content analysis," *IEEE Transactions on Geoscience and Remote Sensing*, vol. GE-22, pp. 222-236, 1984.

Arkin, H. and R. R. Colton, *Statistical Methods*, Barnes and Noble, New York, 1970.

Ballard, D. H. and C. M. Brown, *Computer Vision*, Prentice-Hall, Englewood Cliffs, NJ, 1982.

Bartlett, M. S., "The use of transformations," *Biometrics*, vol. 3, pp. 39-52, 1947.

Becker, R. A. and J. M. Chambers, *S, An Interactive Enviornment for Data Analysis and Graphics*, Wadsworth, Belmont, CA, 1984.

Ben-Bassat, M., *Handbook of Statistics, Volume II*, North-Holland Publishing Co, Amsterdam, 1980.

Cashwell, E. D. and C. J. Everett, *A Practical Manual of the Monte Carlo Method for Random Walk Problems*, pp. 1-153, Pergamon Press, New York, NY, 1959.

Chambers, J. M., W. S. Cleveland, B. Kleiner, and P. A. Tukey, *Graphical Methods for Data Analysis*, Duxbury Press, Boston, 1983.

Chandrasekhar, S., *Radiative Transfer*, pp. 1-393, Dover, New York, NY, 1960.

Chen, C. H., "A study of texture classification using spectral feature," in *Sixth International Conference on Pattern Recognition*, pp. 1074-1077, IEEE Computer Society Press, Munich, 1982.

Chen, P. C. and T. Pavlidis, "Segmentation by texture using co-occurrence matrix and split-and-merge algorithm," *Computer Graphics and Image Processing*, vol. 10, pp. 172-182, 1979.

Cliff, A. D. and J. K. Ord, *Spatial Processes, Models and Applications*, Pion Limited, London, 1981.

Conners, R. W. and C. A. Harlow, "A theoretical comparison of texture algorithms," *IEEE Transactions on Pattern Analysis and Machine Intelligence*, vol. PAMI-2 , pp. 204-222, 1980.

Conners, R. W., M. M. Trivedi, and C. A. Harlow, "Segmentation of a high-resolution urban scene using texture operators," *Computer Vision, Graphics and Image Processing*, vol. 25, pp. 273-310, 1984.

Cooley, W. W. and P. R. Lohnes, *Multivariate Data Analysis*, John Wiley, New York, 1971.

Cooper, C. F., "Snowcover measurement," *Photogrammetric Engineering*, vol. 31, pp. 611-619, 1965.

Dave, J. V., "Effect of atmospheric conditions on remote sensing of a surface nonhomogeneity," *Photogrammetric Engineering and Remote Sensing*, vol. 46, pp. 1173-1180, 1980.

Dave, J. V. and J. Gazdag, "A modified Fourier transform method for multiple scattering calculations in a plane parallel Mie atmosphere," *Applied Optics*, vol. 9, pp. 1457-1466, 1970.

Davis, L. S., M. Clearman, and J. K. Aggarwal, "An empirical evaluation of generalized cooccurrence matrices," *IEEE Transactions on Pattern Analysis and Machine Intelligence*, vol. PAMI-3 , pp. 214-221, 1981.

Davis, P. J., *Circulant Matrices*, John Wiley, New York, NY, 1979.

Diner, D. J. and J. V. Martonchik, "Atmospheric transfer of radiation above an inhomogeneous non-Lambertian reflective ground, I, Theory," *Journal of Quantitative Spectroscopy and Radiative Transfer*, vol. 31, pp. 97-125, 1984.

Dozier, J., "Snow reflectance from Landsat-4 Thematic Mapper," *IEEE Transactions on Geoscience and Remote Sensing*, vol. GE-22, pp. 323-328, 1984.

Draper, N. R. and H. Smith, *Applied Regression Analysis*, John Wiley, New York, 1981.

Ehrich, R. W. and J. P. Foith, "A view of texture topology and texture description," *Computer Graphics and Image Processing*, vol. 8, pp. 174-202, 1978.

Faugeras, O. D., "Texture analysis and classification using a human visual model," in *Proceedings of the Fourth International Joint Conference on Pattern Recognition*, pp. 549-552, 1978.

Faugeras, O. D. and W. K. Pratt, "Decorrelation methods of texture feature extraction," *IEEE Transactions on Pattern Analysis and Machine Intelligence*, vol. PAMI-2 , pp. 323-332, 1980.

Gagalowicz, A., "A new method for texture fields synthesis: Some applications to the study of human vision," *IEEE Transactions on Pattern Analysis and Machine Intelligence*, vol.

PAMI-3 , pp. 520-533, 1981.

Galloway, M. M., "Texture analysis using grey level run lengths," *Computer Graphics and Image Processing*, vol. 4, pp. 172-179, 1975.

Gower, J. C., "A general coefficient of similarity and some of its properties," *Biometrics*, vol. 27, pp. 857-874, 1971.

Grant, I. P. and G. E. Hunt, "Discrete space theory of radiative transfer, I, Fundamentals," *Proceedings of the Royal Society of London*, vol. A313, pp. 183-197, 1969.

Haefner, H., "Digital mapping of mountains under European conditions," in *Operational Applications of Satellite Snowcover Observations*, ed. A. Rango, NASA Conference Publication 2116, pp. 73-91, NASA Goddard Space Flight Center, Greenbelt, MD, 1979.

Hallada, W., B. Bly, R. Boyd, and S. Cox, "A study of feature extraction using divergence analysis of texture features," in *National Conference on Energy Resource Management*, NASA Conference Publication 2261, pp. 1-18, 1982.

Hansen, J. E. and L. D. Travis, "Light scattering in planetary atmospheres," *Space Science Reviews*, vol. 16, pp. 527-610, 1974.

Haralick, R. M., "Statistical and structural approaches to texture," *Proceedings of the IEEE*, vol. 67 , pp. 786-804, 1979.

Haralick, R. M., K. Shanmugan, and I. Dinstein, "Textural features for image classification," *IEEE Transactions on Systems, Man and Cybernetics*, vol. SMC-3 , pp. 610-621, 1973.

Holben, B. and C. Justice, "An examination of spectral band ratioing to reduce topographic effect on remotely sensed data," *International Journal of Remote Sensing*, vol. 2 , pp. 115-133, 1981.

Holmes, Q. A. and D. R. Nüesch, and R. A. Shuchman, "Textural analysis and real-time classification of sea-ice types using digital SAR data," *IEEE Transactions on Geoscience and Remote Sensing*, vol. GE-22 , pp. 113-120, 1984.

House, L. and L. Avery, "The Monte Carlo technique applied to radiative transfer," *Journal of Quantitative Spectroscopy and Radiative Transfer*, vol. 9, pp. 1579-1591, 1969.

Hulst, H. C. van de, *Multiple Light Scattering*, pp. 1-739, Academic Press, New York, NY, 1980.

Hunt, B. R., "The application of constrained least squares estimation to image restoration by digital computer," *IEEE Transactions on Computers*, vol. C-22, pp. 805-814, 1973.

Jernigan, M. E. and F. D'Astous, "Entropy-based texture analysis in the spatial frequency domain," *IEEE Transactions on Pattern Analysis and Machine Intelligence*, vol. PAMI-6 , pp. 237-243, 1984.

Julesz, B., "Experiments in the visual perception of texture," *Scientific American*, vol. 232 , pp. 34-43 1975.

Julesz, B. and T. Caelli, "On the limits of fourier decompositions in visual texture perception," *Perception*, vol. 8, pp. 69-73, 1979.

Justice, C. O., S. W. Wharton, and B. N. Holben, "Application of digital terrain data to quantify and reduce the topographic effect on landsat data," *International Journal of Remote Sensing*, vol. 2 , pp. 213-230, 1981.

Kaufman, Y. J. and R. S. Fraser, "Atmospheric effect on classification of finite fields," *Remote Sensing of Environment*, vol. 15, pp. 95-118, 1984.

Kiang, R. K., "Monte Carlo simulations of atmospheric spread functions for space-born optical sensors," *Proceedings, Eighth International Symposium on Machine Processing of Remotely Sensed Data*, vol. 8, pp. 156-162, Purdue University, West Lafayette, IN, 1982.

Kneizys, F. X., E. P. Shettle, W. O. Gallery, J. H. Chetwynd jr., L. W. Abreu, J. E. A. Selby, S. A. Clough, and R. W. Fenn, "Atmospheric transmittance / radiance: computer code LOWTRAN6," Report AFGL-TR-83-0187, Air Force Geophysics Laboratory, Bedford, MA, 1983.

Laws, K. I., "Textured Image Segmentation," USC/IPI Report 940, Image Processing Institute, University of Southern California, Los Angeles, 1980.

Lichtenegger, J. and K. Seidel, "Snow surface measurements from digital Landsat MSS data," *Nordic Hydrology*, vol. 12, pp. 275-288, 1981.

Lu, S. Y. and K. S. Fu, "Stochastic tree grammar inference for texture synthesis and discrimination," *Computer Graphics and Image Processing*, vol. 9, pp. 234-245, 1979.

Marchuk, G. I., G. A. Mikhailov, M. A. Nazaraliev, R. A. Darbinjan, B. A. Kargin, and B. S. Elepov, *The Monte Carlo Methods in Atmospheric Optics*, pp. 1-208, Springer-Verlag, New York, NY, 1980.

Marr, D., *Vision: A Computational Investigation into the Human Representation of Visual Information*, W. H. Freeman, San Francisco, 1982.

Martinec, J., "Snowmelt-runoff model for stream flow forecasts," *Nordic Hydrology*, vol. 6, pp. 145-154, 1975.

Martinec, J., "Limitations in hydrological interpretations of snow coverage," *Nordic Hydrology*, vol. 11, pp. 209-220, 1980.

Matsuyama, T., K. Saburi, and M. Nagao, "A structural analyzer for regularly arranged textures," *Computer Graphics and Image Processing*, vol. 18, pp. 259-278, 1982.

McCormick, B. H. and S. N. Jayaramamurthy, "Time-series model for texture synthesis," *International Journal of Computer and Information Sciences*, vol. 3 , pp. 329-343, 1974.

McDonnell, M. J., "Box filtering techiques," *Computer Graphics and Image Processing*, vol 17, pp. 65-70, 1981.

Mekler, Y. and Y. J. Kaufman, "Contrast reduction by the atmosphere and retrieval of nonuniform surface reflectance," *Applied Optics*, vol. 21, pp. 310-316, 1982.

Mitchell, O. R. and S. G. Carlton, "Image segmentation using a local extrema texture measure," *Pattern Recognition*, vol. 10, pp. 205-210, 1978.

Mitchell, O. R., C. R. Meyers, and W. Boyne, "A max-min measure for image texture analysis," *IEEE Transactions on Computers*, vol. C-26 , pp. 408-414, 1977.

Modestino, J. W., R. W. Fries, and A. L. Vickers, "Texture discrimination based upon an assumed stochastic texture model," *IEEE Transactions on Pattern Analysis and Machine Intelligence*, vol. PAMI-3 , pp. 557-580, 1981.

Moik, J. G., *Digital Processing of Remotely Sensed Images*, NASA SP-431, Washington D. C, 1980.

Moravec, G. F. and J. A. Danielson, "A graphical method of stream runoff prediction from Landsat derived snowcover data for watersheds in the upper Rio Grande basin of Colorado," in *Operational Applications of Satellite Snowcover Observations*, ed. A. Rango, NASA Conference Publication 2116, pp. 171-183, NASA Goddard Space Flight Center, Greenbelt, MD, 1979.

NASA/NOAA,, *U. S. Standard Atmosphere, 1976*, NOAA-S/T 76-1562, pp. 1-227, Washington, DC, 1976.

Nevatia, R., *Machine Perception*, Prentice-Hall, Englewood Cliffs, NJ, 1983.

Ozişik, M. N. and S. M. Shouman, "Source function expansion method for radiative transfer in a two-layer slab," *Journal of Quantitative Spectroscopy and Radiative Transfer*, vol. 24, pp.

441-449, 1980.

Otte·an, J. and R. S. Fraser, "Adjacency effects of the atmosphere on imaging by surface reflection and atmospheric scattering: cross radiance to zenith," *Applied Optics*, vol. 18, pp. 2852-2860, 1979.

Palmer, P. L., "A technique for determining snow covered area of mountain watersheds from partially cloud-obscured Landsat imagery," NASA Technical Report CP-G1-04099, 1981.

Pearce, W. A., "A study of the effects of the atmosphere on Thematic Mapper observations," Report 004-77, Contract NAS5-23639, pp. 1-155, NASA Goddard Space Flight Center, Greenbelt, MD, 1977.

Pielou, E., *Mathematical Ecology*, Wiley, New York, 1977.

Pietikäinen, M., A. Rosenfeld, and L. S. Davis, "Experiments with texture classification using averages of local pattern matches," *IEEE Transactions on Systems, Man and Cybernetics*, vol. SMC-13 , pp. 421-426, 1983.

Pratt, W. K., *Digital Image Processing*, Wiley, New York, 1978.

Pratt, W. K., O. D. Faugeras, and A. Gagalowicz, "Visual discrimination of stochastic texture fields," *IEEE Transactions On Systems, Man and Cybernetics*, vol. SMC-8 , pp. 796-804, 1978.

Price, J. C., "Comparison of the information content of data from the Landsat-4 Thematic Mapper and Multispectral Scanner," *IEEE Transactions on Geoscience and Remote Sensing*, vol. GE-22 , pp. 272-280, 1984.

Rango, A., J. F. Hannaford, R. L. Hall, M. Rosenzweig, and A. J. Brown, "Snow covered area utilization in runoff forecasts," *ASCE Journal of the Hydraulics Division*, vol. 105, pp. 53-66, 1979.

Rango, A. and K. I. Itten, "Satellite potentials in snowcover monitoring and runoff prediction," *Nordic Hydrology*, vol. 7, pp. 209-230, 1976.

Rango, A. and J. Martinec, "Application of a snowmelt-runoff model using Landsat data," *Nordic Hydrology*, vol. 10, pp. 225-238, 1979.

Rango, A. and J. Martinec, "Accuracy of snowmelt runoff simulation," *Nordic Hydrology*, vol. 12, pp. 265-274, 1981.

Rango, A., V. V. Salomonson, and J. L. Foster, "Seasonal streamflow estimation in the Himalayan region employing meteorological satellite snow cover observations," *Water Resources*

Research, vol. 14, pp. 359-373, 1977.

Rawls, W. J. and T. J. Jackson, "Pattern recognition analysis of snowdrifts," *Nordic Hydrology*, vol. 10, pp. 251-260, 1979.

Scheid, F., *Numerical Analysis*, pp. 1-422, McGraw-Hill, New York, NY, 1968.

Seidel, K., F. Ade, and J. Lichtenegger, "Augmenting Landsat MSS data with topographic information for enhanced registration and classification," *IEEE Transactions on Geoscience and Remote Sensing*, vol. GE-21 , pp. 252-258, 1983.

Shafer, B. A. and C. F. Leaf, "Landsat derived snowcover as an input variable for snowmelt runoff forecasting in south central Colorado," in *Operational Applications of Satellite Snowcover Observations*, ed. A. Rango, NASA Conference Publication 2116, pp. 151-169, NASA Goddard Space Flight Center, Greenbelt, MD, 1979.

Souza, P. de, "Texture recognition via autoregression," *Pattern Recognition*, vol. 15 , pp. 471-475, 1982.

Stamnes, K. and P. Conklin, "A new multi-layer discrete ordinate approach to radiative transfer in vertically inhomogeneous atmospheres," *Journal of Quantitative Spectroscopy and Radiative Transfer*, vol. 31, pp. 273-282, 1984.

Thomas, I. L., T. D. Prowse, and I. F. Owens, "Mapping New Zealand and Antarctic snowpack from Landsat," in *Operational Applications of Satellite Snowcover Observations*, ed. A. Rango, NASA Conference Publication 2116, pp. 41-51, NASA Goddard Space Flight Center, Greenbelt, MD, 1979.

Thompson, A. G., "Utilization of Landsat monitoring capabilities for snowcover observations," in *Operational Applications of Satellite Snowcover Observations*, ed. A. Rango, NASA SP-391, pp. 113-127, NASA Goddard Space Flight Center, Greenbelt, MD, 1975.

Thomsen, A. G., "Spatial simulation of snow processes," *Nordic Hydrology*, vol. 11, pp. 273-284, 1980.

Tomita, F., Y. Shirai, and S. Tsuji, "Description of textures by structural analysis," *IEEE Transactions on Pattern Analysis and Machine Intellligence*, vol. PAMI-4 , pp. 183-191, 1982.

Tou, J. T., "Pictorial feature extraction and recognition [illegible] image modelling," *Computer Graphics and Image Processing*, vol. 12, pp. 376-406, 1980.

Tukey, J. W., *Exploratory Data Analysis*, Addison-Wesley, Reading, MA, 1977.

Ueno, S., Y. Haba, Y. Kawata, T. Kusaka, and Y. Terashita, "The atmospheric blurring effect on remotely sensed earth imagery," in *Remote Sensing of Environment: Inversion Methods and Applications*, ed. A. L. Fymat and V. E. Zuev, pp. 305-321, Elsevier, New York, NY, 1978.

Vickers, A. L. and J. W. Modestino, "A maximum likelihood approach to texture classification," *IEEE Transactions on Pattern Analysis and Machine Intelligence*, vol. PAMI-4 , pp. 61-68, 1982.

Wang, S., F. D. Velasco, A. Wu, and A. Rosenfeld, "Relative effectiveness of selected texture primitive statistics for texture discrimination," *IEEE Transactions on Systems, Man and Cybernetics*, vol. SMC-11 , pp. 360-370, 1981.

Weszka, J. S., C. R. Dyer, and A. Rosenfeld, "A comparative study on textural measures for terrain classification," *IEEE Transactions on Systems, Man and Cybernetics*, vol. SMC-6 , pp. 269-285, 1976.

Wiscombe, W. J., "Extension of the doubling method to inhomogeneous sources," *Journal of Quantitative Spectroscopy and Radiative Transfer*, vol. 16, pp. 477-489, 1976.

Wiscombe, W. J., "On initialization, error and flux conservation in the doubling method," *Journal of Quantitative Spectroscopy and Radiative Transfer*, vol. 16, pp. 635-658, 1976.

Wiscombe, W. J., "The delta-M method: rapid yet accurate radiative flux calculations for strongly asymmetric phase functions," *Journal of the Atmospheric Sciences*, vol. 34, pp. 1408-1422, 1977.

Wiscombe, W. J., "Improved Mie scattering algorithms," *Applied Optics*, vol. 19, pp. 1505-1509, 1980.

Wiscombe, W. J. and J. W. Evans, "Exponential-sum fitting of radiative transmission functions," *Journal of Computational Physics*, vol. 24, pp. 416-444, 1977.

Zucker, S. W. and D. Terzopoulos, "Finding structure in co-occurrence matrices for texture analysis," *Computer Graphics and Image Processing*, vol. 12, pp. 286-308, 1980.